UNIVERSITAT DE
BARCELONA

Inhibition of the PI3K/Akt pathway as a therapeutic strategy for pediatric-type diffuse high-grade gliomas

Leire Balaguer Lluna

ADVERTIMENT. La consulta d'aquesta tesi queda condicionada a l'acceptació de les següents condicions d'ús: La difusió d'aquesta tesi per mitjà del servei TDX (**www.tdx.cat**) i a través del Dipòsit Digital de la UB (**diposit.ub.edu**) ha estat autoritzada pels titulars dels drets de propietat intel·lectual únicament per a usos privats emmarcats en activitats d'investigació i docència. No s'autoritza la seva reproducció amb finalitats de lucre ni la seva difusió i posada a disposició des d'un lloc aliè al servei TDX ni al Dipòsit Digital de la UB. No s'autoritza la presentació del seu contingut en una finestra o marc aliè a TDX o al Dipòsit Digital de la UB (framing). Aquesta reserva de drets afecta tant al resum de presentació de la tesi com als seus continguts. En la utilització o cita de parts de la tesi és obligat indicar el nom de la persona autora.

ADVERTENCIA. La consulta de esta tesis queda condicionada a la aceptación de las siguientes condiciones de uso: La difusión de esta tesis por medio del servicio TDR (**www.tdx.cat**) y a través del Repositorio Digital de la UB (**diposit.ub.edu**) ha sido autorizada por los titulares de los derechos de propiedad intelectual únicamente para usos privados enmarcados en actividades de investigación y docencia. No se autoriza su reproducción con finalidades de lucro ni su difusión y puesta a disposición desde un sitio ajeno al servicio TDR o al Repositorio Digital de la UB. No se autoriza la presentación de su contenido en una ventana o marco ajeno a TDR o al Repositorio Digital de la UB (framing). Esta reserva de derechos afecta tanto al resumen de presentación de la tesis como a sus contenidos. En la utilización o cita de partes de la tesis es obligado indicar el nombre de la persona autora.

WARNING. On having consulted this thesis you're accepting the following use conditions: Spreading this thesis by the TDX (**www.tdx.cat**) service and by the UB Digital Repository (**diposit.ub.edu**) has been authorized by the titular of the intellectual property rights only for private uses placed in investigation and teaching activities. Reproduction with lucrative aims is not authorized nor its spreading and availability from a site foreign to the TDX service or to the UB Digital Repository. Introducing its content in a window or frame foreign to the TDX service or to the UB Digital Repository is not authorized (framing). Those rights affect to the presentation summary of the thesis as well as to its contents. In the using or citation of parts of the thesis it's obliged to indicate the name of the author.

UNIVERSITAT DE BARCELONA

SJD Sant Joan de Déu
Barcelona · Hospital
Pediatric Cancer Center

SJD
Sant Joan de Déu
Institut de Recerca

University of Barcelona - Faculty of Medicine
Doctorate program: Biomedicine
Research line: Molecular and cellular biology of cancer

Inhibition of the PI3K/Akt pathway as a therapeutic strategy for pediatric-type diffuse high-grade gliomas

Pediatric Cancer Treatment Group
Pediatric Cancer Program
Institut de Recerca Sant Joan de Déu & Department of Pediatric Oncology
SJD Pediatric Cancer Center Barcelona

PhD candidate: Leire Balaguer Lluna

Thesis director: Dr. Ángel M. Carcaboso

Thesis tutor: Dra. Teresa Maria Ribalta Farrés

Table of content

List of figures

List of tables

Dr. Ángel Montero Carcaboso, director of the thesis ***Inhibition of the PI3K/Akt pathway as a therapeutic strategy for pediatric-type diffuse high-grade gliomas*** completed by the PhD candidate **Leire Balaguer Lluna**, endorses the originality of the research work included in this thesis.

> “The most effective way to do it, is to do it”
>
> Amelia Earhart

A la meua família

Agradecimientos

Estoy inmensamente agradecida por haber tenido la suerte de compartir mi vida, tanto personal como profesional con las siguientes personas, quienes han hecho posible la realización de mi doctorado.

Al Dr. Ángel Montero Carcaboso. Me gustaría comenzar agradeciendo a mi supervisor y mentor Ángel por la oportunidad que me brindó en 2019 al permitirme seguir mi carrera científica en su grupo de investigación. Su experiencia y soporte han sido fundamentales para poder afrontar esta tesis doctoral con éxito. Muchas gracias por tus consejos durante estos años.

A mis compañeros. Muchas gracias a toda la familia del laboratorio de investigación del cáncer pediátrico del PCCB, sin vuestra ayuda estos años no hubiesen sido iguales. Especialmente, gracias a mi trio calavera por estar siempre a mi lado, Dra. Estelita Prada, Dra. Chari Aschero y (casi doctora) Claudi Resa. Las risas, los lloros, las cerves post-lab, las cenas… Sois mis pilares, y sin vosotras difícilmente hubiese superado estos 5 años! Dr. Víctor, no podías faltar. Gracias por hacer de nuestras tesis un cachondeo con tus mil fotos y videos inesperados, por las horas de estabulario con terapia incluida, por Cucurella, o por tus problemas intestinales de los cuales, quizá, sabemos más de lo que deberíamos!! Dra. Merxe, la otra parte del DIPG team, gracias por ser la otra mitad, hemos conseguido superar estos años sin pedir los papeles del divorcio! Dras. Maria C y Helena, gracias por estar cuando esto empezó, no pudo haber sido mejor! Pabli, Meri, Carlita, Chao, Yas, Dra. Sara P, Jara, Ana y Nuria, gracias por vuestra ayuda, a cualquier nivel, ha sido indispensable para mi crecimiento profesional y, sobretodo, personal. Gracias a las chicas del subsuelo de hemato, por la paciencia que tuvieron cuando era incapaz de entender los mil problemas que supone un análisis NGS y por responder a nuestras preguntas básicas de genética. Muchas gracias también a todos los miembros senior del laboratorio, Dres. Carlos, Marta, Sara S, Silvia, Sole, por vuestra ayuda durante la tesis. Y Xènia, gracias por los millones de geles de WB! Y por último, pero no menos importante, os agradeceré siempre vuestro apoyo técnico y moral, nuestros técnicos de confianza: Mònica, Isa, Ana D y Óscar. Muchas gracias!!

A las de siempre. Volver a mis raíces y que siempre estéis me ha permitido desconectar, pensar, y volver con más fuerzas. Sobre todo, gracias Mai, por tanto. Por tu apoyo, tus consejos de vida y por mostrarme siempre lo orgullosa que estas de mí, siempre con las palabras indicadas. Gracias!

A la meua família. Sense vosaltres no haguera arribat fins ací. Vosaltres em vau ensenyar des de ben xicoteta que havia de ser perseverant i costant en les decisions que prenia i en els reptes que em plantejava aconseguir, sempre tenint el vostre suport si m'equivocava o si les coses no eixien bé. Gràcies per ajudar-me a continuar endavant, a no rendir-me. Vore com d'orgullosos us sentiu de mi és el que m'ha fet arribar fins ací, sempre amb paraules d'ànim i molt, molt d'amor. Per fi abuela et podré contestar a la teua pregunta recurrent "ja has presentat el treball este que et porta de cap?". Sí, ja ho tenim. Vos vull molt.

A Quim i Jacki. Que haguera fet si no haguéssiu estat els dies que tornava a casa volent enviar-ho tot a fer la mà? Qui m'hauria fet entrar en raó? En qui hauria celebrat quan les coses em sortien bé? Tantes xarrades passejant o a la vermu... Tot aquest camí vos l'he d'agrair a vosaltres, que m'heu recolzat en cada pas que he donat, bo o dolent, encara que estiguéssiu o no d'acord amb mi, sempre al meu costat per fer front junts a tot. Perquè una mirada val més que mil paraules diuen.. puc confirmar que així és, una mirada vostra de "tu pots" no la canvio per res. Us estimo.

Finalmente, quiero expresar mi gratitud a todas las familias donantes por su apoyo indispensable e incondicional, así como por su fortaleza y ánimo constantes para seguir con nuestros trabajos de investigación. Gracias a vuestra ayuda, podemos llevar a cabo nuestros proyectos y, juntos, avanzar para estar cada día más cerca de encontrar una cura para el DIPG

Chapter 1. Introduction

1. Diffuse intrinsic pontine gliomas

Pediatric-type diffuse high-grade gliomas (pHGG) are orphan malignancies that represent approximately 10% of the pediatric brain cancers[1], classified as grade III-IV tumors by the fifth edition of the World Health Organization of tumors affecting the CNS[2]. The estimated world standardized incidence rate of pHGG for patients aged 0–17 years is 6 per million person-years[3]. The median age at presentation of these tumors is 6-7 years, independently of the gender, with a median overall survival (OS) lower than a year from diagnosis[4]. Diffuse midline gliomas (DMG) H3 K27-altered[2,5] are the most frequent and deadly subclass of pHGG. Around 80% of DMG are located in the pons, receiving the name of diffuse intrinsic pontine gliomas (DIPG). Tumors evolving in this delicate area of the brain interfere with many nerves involved in essential body functions regarding the coordination of motor control signals[6,7]. Tumor cells develop diffusely and disseminate continuously, affecting different parts of the brain, spreading from the rostral to the frontal parts, usually without disrupting the integrity of the blood-brain barrier (BBB)[7,8]. Because of the anatomic location and the infiltrative nature of these tumors, surgical resection is not feasible, and chemotherapy treatments have not demonstrated sufficient anticancer activity. Radiation therapy in the only available treatment to control tumor growth, at least for a short period[9]. The analysis of biopsy samples obtained from patients with DIPG contributed to elucidate the molecular background of these tumors, characterized by a unique recurrent mutation in genes encoding histone H3 (H3K27M)[10-12]. The new knowledge on the genomic landscape of these tumors opened an era of discoveries that will likely end up in the development of new and effective therapies for patients.

In my PhD work, I leveraged on the preclinical pHGG models, most of them DIPG, already established at HSJD from patients, and I established new models from new patients. I used these preclinical tools to assess the rationale and efficacy of several pharmacological treatments for DIPG.

2. Genomic landscape of pHGG

Clinical researchers at the Necker hospital (Paris) were the first to demonstrate that obtaining biopsies from pediatric CNS tumors in the midline, most of them in the brainstem, is a safe procedure[13]. Since then, tissue samples have been used to improve the molecular knowledge on this disease, with clear implications for the diagnosis of patients, the selection of targeted treatments and the design of new clinical trials[14,15].

2.1. Histone-3 driver mutations

Initial analyses on the genomic and epigenomic profile of pHGG revealed a unique recurrent somatic gain-of-function mutation of the histone H3 genes (*HIST1H3B*, *HIST1H3C* and *H3F3A*), present in approximately 80% of DIPGs. These mutations were immediately considered as a driver and biological hallmark of these tumors[11,16,17]. Histones participate in the process of DNA condensation and undergo post-translational modifications, such as methylation, acetylation, phosphorylation, ubiquitination and SUMOylation (alteration by the covalent attachment of a small ubiquitin-like modifier protein to lysine residues[18]). These modifications may prompt changes in DNA function and transcription by regulation of DNA access to the cellular transcriptional machinery, remodelling different biological processes involving gene expression[19]. The missense alteration in the NH2-terminal tail of H3 results in a substitution of lysine (K) for methionine (M) at position 27. In the normal stem cell development, differentiation genes are tightly regulated by the tri-methylation in post-translational modification sites of the H3 tail, mainly resulting in tri-methylated K27 (H3K27me3). As a consequence of the K27M mutation, di- and tri- methylation of histone H3 at K27 (a process catalyzed by the methyltransferase EZH2, part of the PRC2 complex) is radically reduced, resulting in the aberrant activation of genes leading to malignancy (**Figure 1**)[20,21].

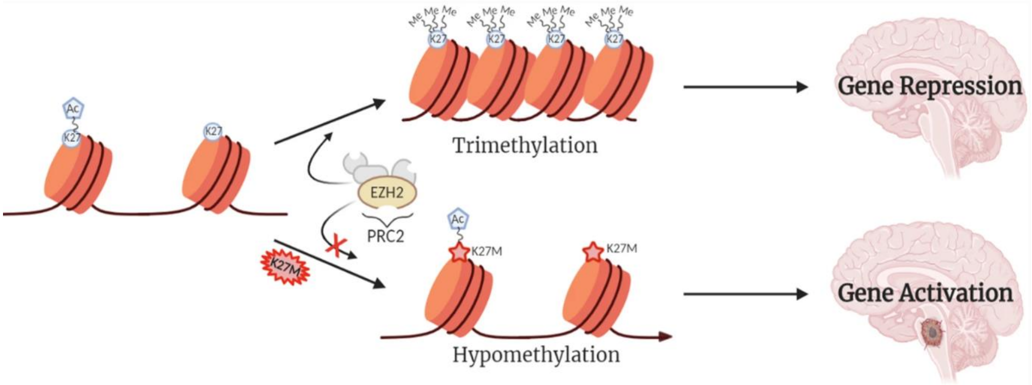

Figure 1. Scheme of H3K27M epigenetic modification. In H3K27M, the lysine substitution inhibits EZH2 binding, preventing PCR2-dependent methylation and leading to aberrant gene activation. Reproduced from reference[16].

Other genetic alterations of H3 also result in the depletion of H3K27me3. The most frequents are H3 p.Gly34Arg/Val (H3.3G34R/V) mutations, which are harbored in approximately 30% of diffuse gliomas arising in the cerebral hemispheres. In these gliomas, the mutated residue is adjacent to the lysine at position 36, reducing the tri- methylation of H3K36 site and repressing the methyltransferase SETD2/5 activity[8,22,23].

An important publication by Alan Mackay *et al.* built an integrated molecular meta-analysis of 1,000 pHGG, many of them DIPG[10]. The analysis grouped diffuse gliomas into different subgroups, according to the presence or absence of H3 mutation, the anatomical location of tumor, the age at diagnosis and the OS of patients. Tumors harboring the mutation H3.1K27M occur exclusively in the pons of the youngest DIPG patients, with a median age of 5 years old, while H3.3K27M tumors arise in a range of midline structures (including the thalamus, brainstem, cerebellum and spine) in patients of a median age of 8 years. Tumors driven by the K27M alteration are universally fatal, with a median OS of 11 and 15 month for H3.3 and H3.1 mutants, respectively). In contrast, H3.3G34R/V mutations (only reported for *H3F3A* gene) are only found in diffusely infiltrative tumors arising in the cerebral hemispheres, predominantly in the parietal or temporal lobes of adolescents or young adults, at a median age of 15 years old, and male predominance. Patients with H3.3G34R/V mutations have longer survival than those with K27M alterations, but their median OS is still limited to 18 months after the diagnosis. Those patients with pHGG with wild type gene H3 have better prognosis, especially when they are infant (younger than one year old) patients. These lesions are highly heterogeneous, with a variety of genomic and epigenomic features, and they appear as hemispheric tumors affecting infants/new-borns, children, adolescent and young adults (**Figure 2**)[10,24,25].

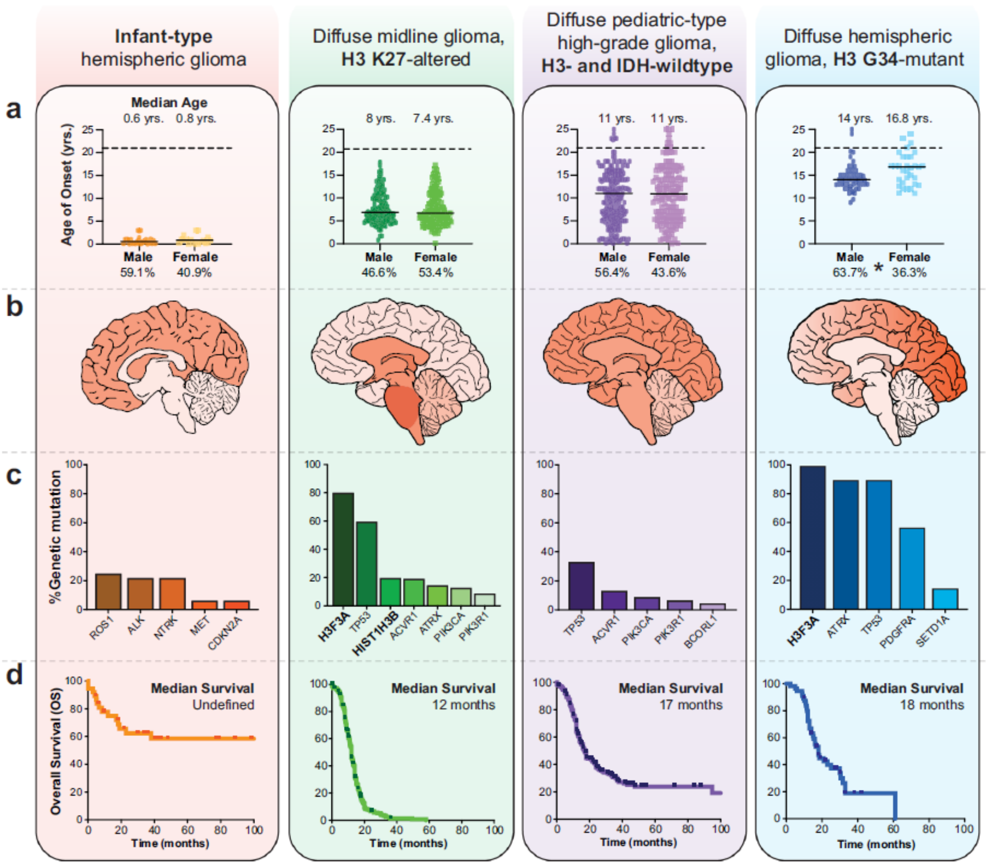

Figure 2. New classification of the pHGG subgroups, according to the clinicopathological and molecular characteristics. Driver mutations in H3.3 (K27M and G34R/V), H3.1K27M and H3 WT of tumors show different subgroups of disease, along with differences in location, age at diagnosis and clinical outcome of patients. Reproduced from reference[24].

2.2. Copy number abnormalities in pHGG

The genome-wide analysis of pHGG/DIPG tumors identified other recurrent genomic abnormalities and copy number imbalances (CNA) underlying these tumors (**Figure 3**).

The group led by Suzie Baker at Saint Jude evaluated the frequencies of large-scale chromosomic alterations in 43 biopsies and autopsies of DIPG[26]. They found focal gains of genes encoding receptors tyrosine kinase (RTKs) or cell-cycle regulatory genes in 24 of 43 tumor samples, including *PDGFRA* (in 13 of

43 DIPG), *MET*, *IGF1R*, *ERBB4* and *EGFR* genes. Other focal CNA gains were described, also affecting RTK-Ras-phosphoinositide 3-kinase pathway, such as *KRAS*, *AKT1*, *AKT3* and *PIK3CA* genes, and focal deletions of *NF1*. Focal gains were found in regulatory components of the RB pathway including genes encoding *cyclin D1, D2* and *D3* and *CDK4/6*[26].

Posterior work by Mackay *et al*. identified recurrent gains of chromosome 1q, the location of the gene encoding for H3.3, which explained the usually high variant allele fraction of H3.3K27M in these tumors[27]. They also described common large-scale alterations including loss of 17p (156 cases), which contains *TP53* at 17p13.1, and gains of 9q, both alterations correlating with shorter OS of the patients. They described as "high-level" the amplifications found at 4q12 (containing *PDGFRA/KIT/KDR* genes), 2p24.3 (*MYCN/ID2*), 7p11.2 (*EGFR*), 7q21.2 (*CDK6*) and 7q31.2 (*MET*), as well as focal deletions at 9p23.3 (*CDKN2A/B*) and 10q (*PTEN*), a negative regulator of PI3K signalling and tumor suppressor in many human cancers[28]. They observed a shorter OS in patients diagnosed with tumors harboring these amplifications and a better prognosis in patients with tumors with *CDKN2A*/*B* deletions[10].

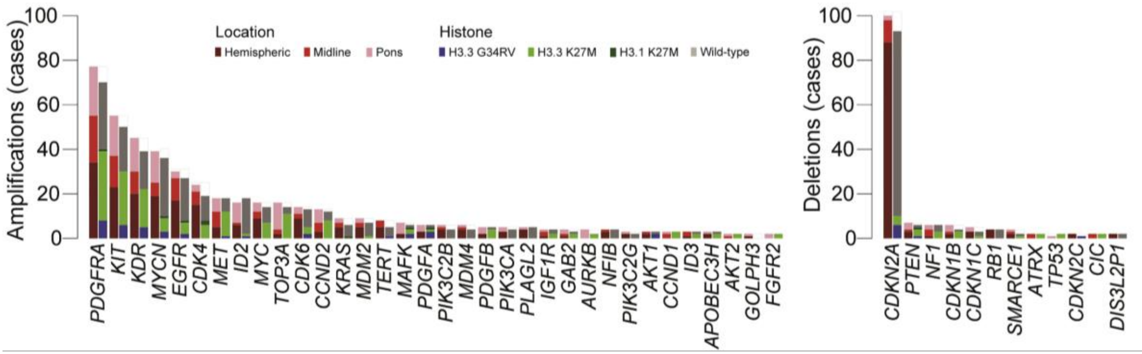

Figure 3. DNA copy-number aberrations in pHGG/DIPG. Most recurrent copy-number alterations of 834 pHGG/DIPG tumors are shown, in order of frequency, and colours represent the anatomical location and histone mutation. Reproduced from reference[10].

2.3. Recurrent somatic mutations in pHGGs

In addition to the histone-3 variant mutations, other recurrent mutations have been identified in pHGG. The data obtained from a large series of tumors have revealed the distinction between histone-dependent subgroups. Additionally, each subgroup exhibit co-segregated somatic mutations and pathway dysregulations that contribute to tumor development[20,29]. These distinctions may allow for the selection of targeted therapies specific to each DIPG subgroup (**Figure 4**)[10].

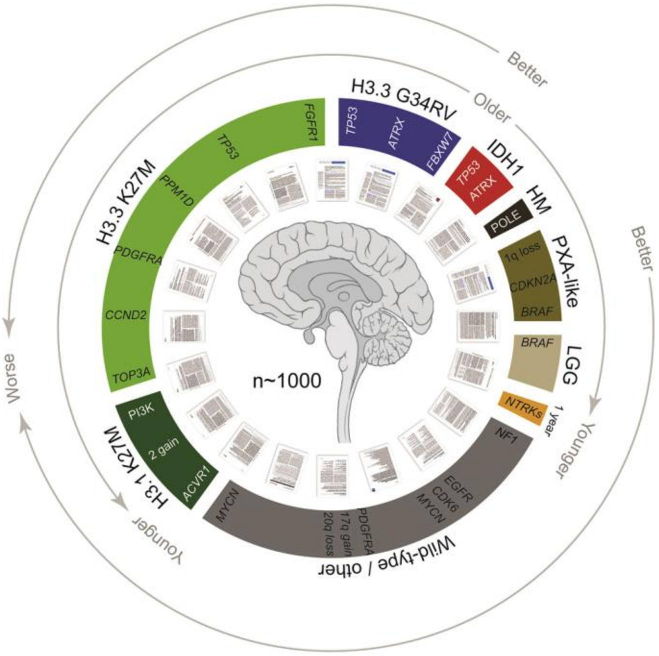

Figure 4. Genetic landscape across 1000 cases of pediatric gliomas. Schematic illustration of the multiple subgroups of low and high-grade gliomas that differ based on lesson location, age at diagnostic and prognosis. In addition to the subgroup-driving alterations, tumor commonly harbour associated alterations are represented. Reproduced from reference[10].

Mutations in the *ATRX* gene play a critical role in H3.3G34R/V-mutant neoplasms, with genetic alterations observed in over 80% of affected individuals, and reported to reach 100% in some clinical case series[30]. *ATRX* and H3.3G34R/V mutations exhibit co-segregation, with a high incidence of concurrent *TP53* mutations, observed in 88% of cases in a series of 135 patients diagnosed with diffuse hemispheric glioma, H3.3G34-mutant[31]. Recent DNA methylation studies have shown that the H3.3G34R/V subgroup is the only histone mutant category within pHGG to display significantly elevated methylation at the promoter region of O-6-methylguanine-DNA methyltransferase (*MGMT*), a key DNA repair enzyme[10,32,33]. This methylation pattern may be linked to increased sensitivity to temozolomide treatment, potentially leading to improved clinical outcomes[34]. In a study of 162 pHGG samples, *MGMT* promoter methylation was observed in 40 cases, with 75% of H3.3G34-mutant tumors showing methylation, compared to only 3% of H3K27-mutant cases[35]. Additionally, around half of H3.3G34R/V tumors (in a cohort of 95) bear activating *PDGFRA* mutations that display strong selection pressure at recurrence[22]. This pathway signalling opens a potentially targetable route for new treatments (**Figure 4**)[22].

TP53 mutations are also present in 22-40% of DIPG, co-segregating with H3.3K27M and typically with *PPM1D* mutations, a more aggressive phenotype of tumors with marked epigenetic deregulation[36]. Co-occurrence of H3.3K27M and *TP53* mutations imply worse clinical outcomes compared to patients with only one of them[10]. Mutations predominantly of gain-of-function in RTKs, such as *PDGFRA* and *FGFR1*, also occur frequently in this subset of tumors. *PDGFRA* alterations prevail in tumors arising in the pons, and *FGFR1* variants are restricted to the thalamus (**Figure 4**)[10].

Pathania *et al*. developed a mouse model that recapitulated partially the histological and molecular traits of H3.3-mutant pHGG when the mutations were introduced within a particular developmental stage in mice[37]. They observed that H3.3K27M in combination with *TP53* loss introduced *in utero* were sufficient to induce tumorigenesis, although tumors appeared postnatally, after 6-8 months. They found that the simultaneous presence of H3.3K27M and *TP53* loss, along with wild-type *PDGFRA* overexpression, accelerated tumor development and enhanced invasiveness. In contrast, *ATRX* knockdown led to tumors that were more localized (**Figure 5**)[37].

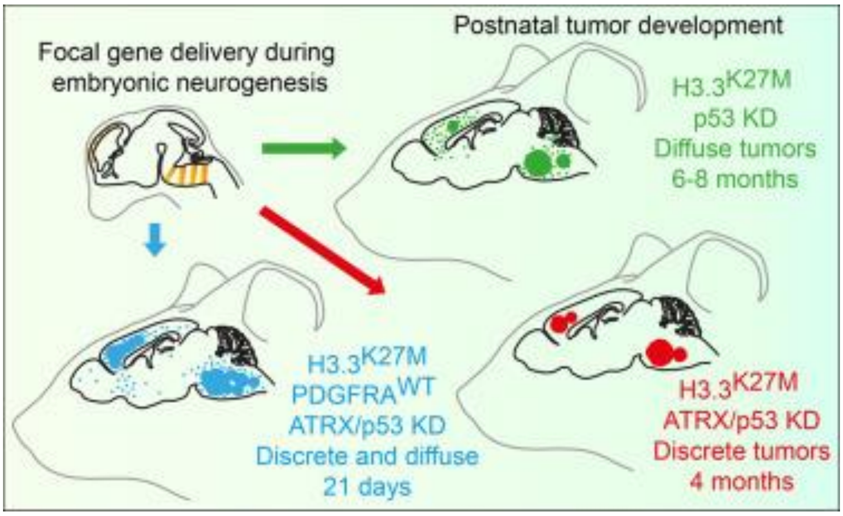

Figure 5. Diagram showing how H3.3K27M cooperates with TP53 loss and PDGFRA gain in mouse embryonic neural progenitor cells to induce invasive pHGG. Reproduced from reference[37].

H3.1K27M-mutated DIPG tumors are confined to the pons and are characterized at the copy-number level by gains and losses of entire chromosomal arms, including frequent gains of 1q and chromosome 2, as well as the loss of 16q[10]. Some point mutations are also identified in this subgroup of tumors, especially somatic mutations R206H and G328V within the activin A receptor type 1 (*ACVR1*), found in up to 25-30% of DIPG[38,39]. Mackay *et al*. also identified an enrichment of downstream PI3K pathway mutations, such as *PIK3CA* and *PIK3R1*, co-segregating with H3.1K27M mutations, compared with the upstream RTK alterations present in H3.3K27M DIPGs (**Figure 4**). Fortin *et al*. demonstrated that the *ACVR1*^{G328V} mutation works in conjunction with the *Hist1h3b*^{K27M} driver mutation to block the differentiation of oligodendrocyte precursor cells in genetically engineered models (GEMMs) of DIPG[40]. For the development of high-grade diffuse gliomas, an additional mutation in *PIK3CA*^{H1047R} was required, confirming the necessity of co-occurring alterations for tumorigenesis (**Figure 6**)[40].

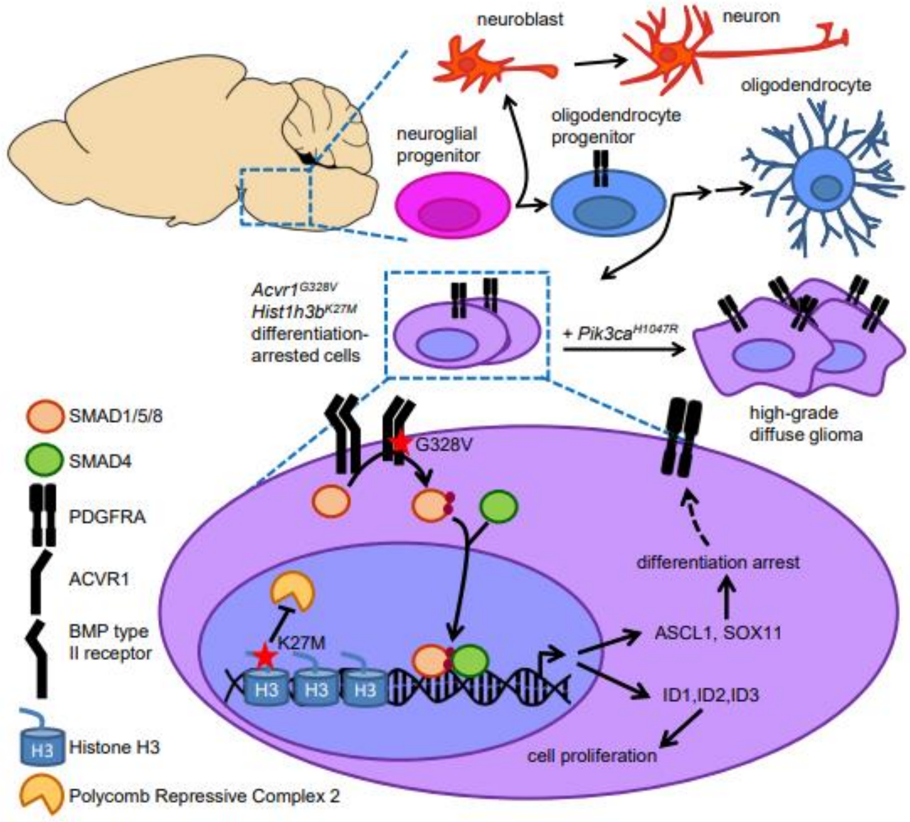

Figure 6. Mutant *ACVR1* inhibits glial cell differentiation and promote tumor development. The scheme shows the *ACVR1*^{G328V} mutation, both individually and in combination with *Hist1h3b*^{K27M}, resulting in effects on cell proliferation and differentiation. The addition of *ACVR1*^{G328V}, *Hist1h3b*^{K27M}, and *PIK3CA*^{H1047R} mutations in the oligodendrocyte precursor cells were required for tumor initiation and progression. Reproduced from reference[40].

3. Blood-brain barrier

The brain is one of the most vascularized organs and presents a special type of blood vessels characterized by the presence of a BBB, which is formed by specialized endothelial cells with surrounding basal lamina, pericytes, astrocytes and microglia. Together, they act as a physical and biochemical barrier to protect the CNS from the penetration of toxins and large hydrophilic substances, also providing essential nutrients to the brain. Recent data suggests that the pons has a tighter BBB ("super-BBB") compared to the cortex, further restricting the entrance of substances to the brain[41,42] (**Figure 7**).

In DIPG, diagnostic imaging techniques suggest that the BBB is intact in the patients at the time of the initial diagnosis[43], thus posing a significant obstacle for drug penetration from the blood to the brain parenchyma. Drug efflux proteins such as the human ATP-binding cassette (ABC) transporter family, including the P-glycoprotein (P-gp, *ABCB1*), the breast cancer resistance protein (BCPR, *ABCG2*) and the multidrug resistance proteins (MRPs, *ABCC*s), limit the delivery of chemotherapy to the CNS[44] (**Figure 7**).

Whether disrupting the BBB could be a feasible strategy to increase drug efficacy against pHGG remains not totally clear. Approaches to do so include transient disruption with warm 20% intracarotid mannitol, focused ultrasounds or administration of inhibitors of drug efflux transporters. All of them presented promising preclinical results, but their use in patients needs improvement[45-47].

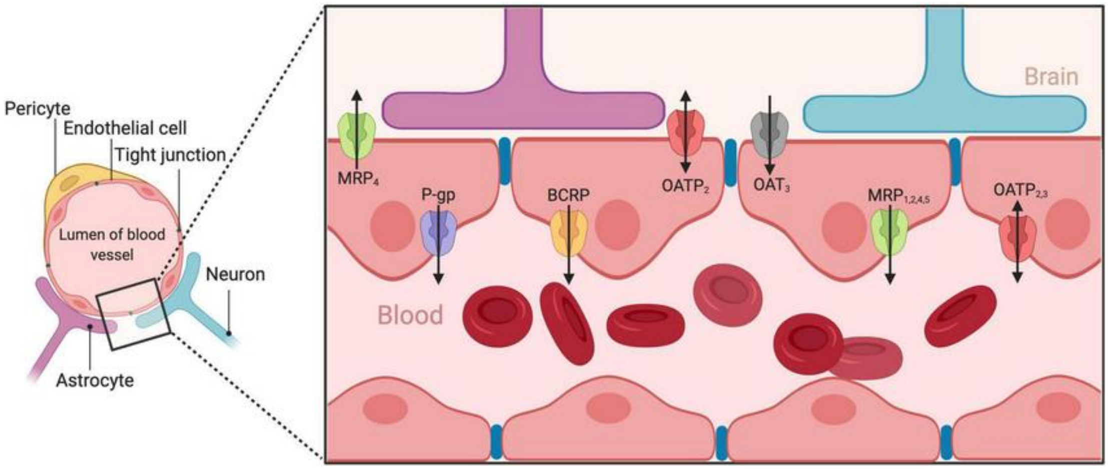

Figure 7. Representative scheme of the components in the BBB. The BBB consists of endothelial cells at the cerebral capillary level. These endothelial cells interact with perivascular structures, including the basal lamina, astrocytic end-feet processes, perivascular neurons, and pericytes. Tight junctions between the endothelial cells seal the intercellular space, maintaining the BBB integrity. The ABC efflux transporters, such as P-gp and BCRP and MRPs are expressed on the luminal side of endothelial cells. They prevent blood compounds from accessing the brain. Reproduced from reference[48].

4. Diagnosis and treatment of patients with DIPG

4.1. Clinical presentation

Patients diagnosed with DIPG present neurological symptomatology consistent with the anatomic location of the tumor. Typically, symptoms appear only a month before demanding medical assistance. Cranial nerves VI and VII are most commonly affected and specific to DIPG because they originate close to where the tumor usually infiltrates. Over 50% of patients display compression or dysfunction of critical white matter tracks in the brainstem, resulting in cranial nerves palsies (facial weakness and diplopia), long tract signs (motor deficits, hyperreflexia, Babinski reflex, clonus, increased tone) and cerebellar dysfunction (ataxia, dysmetria, dysarthria). These three frequent clinical characteristics are referred as the “classic triad” and alert clinics of a probable diagnosis of DIPG[36,49,50]. In less than 10% of patients, signs and symptoms of increased intracranial pressure may be present at the time of diagnosis, due to the obstructive hydrocephalus resulting from the expansion of the pons. This condition is more common at further stages of the disease progression[20,36]. While the epicentre and origin of DIPG occurs in the pons, during disease progression cells spread to the cerebellum or even to more distant parts of the brain.

4.2. Diagnostic imaging

The diagnosis of DIPG is based on conventional magnetic resonance imaging (MRI) findings. MRI is the preferred imaging method and it is complemented with computed tomography (CT) in specific cases[36]. MRI typically includes T2 and fluid attenuated inversion recovery (FLAIR) weighted images and T1-weighted with and without contrast, to enhance lesion visibility by suppressing CSF signal compared with conventional T2 imaging[51]. DIPG tumors are usually centered in the pons, often occupying at least 50% of its axial diameter and causing its expansion, potentially encasing the basilar artery. In a normal brain MRI, white matter appears bright (light grey/white) on a T1-weighted scan, whereas it appears dark grey on a T2-weighted scan. In DIPG tumors, they appear hypointense or isointense on T1-weighted images and hyperintense on T2-weighted images, with ill-defined margins, homogeneous enhancement, and minimal contrast with gadolinium uptake suggesting necrosis or inflammation [20,52,53] (**Figure 8**).

Recent studies highlight differential MRI features between H3K27M and WT subgroups, including enhancement quality, margin thickness, non-contrast-enhancing tumor margins, edema proportion, and cortical invasion, aiding in glioma subgroup discrimination with implications for diagnosis, treatment planning, and future trials[54,55].

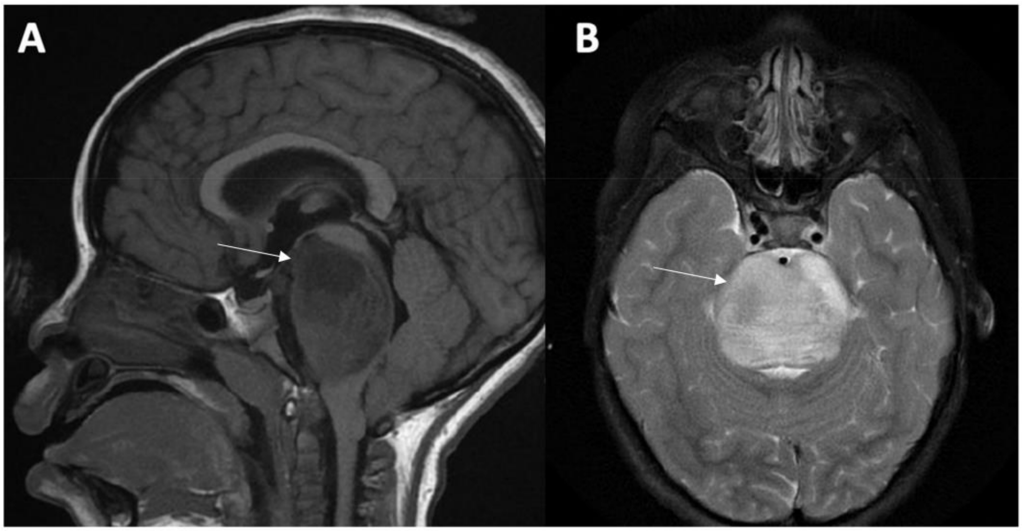

Figure 8. DIPG tumor imaging at the pons. MRI of the brain of a child with H3K27M-altered glioma. The imaging demonstrated a (A) sagittal T1 hypointense and (B) axial T2 hyperintense DIPG tumor occupying nearly half of the axial diameter. Arrows indicate the tumor. Reproduced from reference[20].

4.3. The standard of care

Focal radiation therapy (RT) is the only treatment that improves life expectancy for DIPGs, although its effect is only palliative. Over the past 20 years, RT at a dose of a 54-60 Gy administered in fractions of 1.5-2 Gy over 6 weeks, usually daily, has been the standard treatment recommendation for H3K27M diffuse midline gliomas, controlling tumor growth for a short time of period, and prolonging survival for up to 3 months in 70-80% of patients[39].

To enhance RT and minimize toxicity, hyperfractionated and hypofractionated regimens have been proposed for newly DIPG diagnostics. Hyperfractionated therapy with doses up to 72 Gy is less effective and increases radiation toxicity[56]. In contrast, hypofractionated therapy with doses of 39-45 Gy over 2.6-3 weeks is feasible, well-tolerated, and improves quality of life, but does not improve event-free survival or overall survival in DIPG patients[57-59]. Symptomatic tumor progression after RT is common due to the aggressive nature of the disease, leading to the consideration of re-irradiation for additional palliative benefits[60].

Unfortunately, 3-8 months post-RT, most patients show radiological and clinical signs of tumor progression, often leading to neo-adjuvant chemotherapy trials with agents like temozolomide, cisplatin, carboplatin, or irinotecan. However, no chemotherapy agents have yet shown significant improvement in PFS or OS compared to radiation therapy alone in patients with DIPG.

5. Biopsying DIPG

In 2007, neurosurgeons at the Hospital Necker–Enfants Malades (Paris) performed stereotactic biopsies on 24 children, establishing it as a safe procedure for obtaining tumor samples from the pontine region[61]. By 2012, multiple reports had been published highlighting the safety and importance of brainstem biopsies. Then, the stereotactic biopsy was stablished as a standard practice in an effort to enhance diagnosis of patients with DIPG[13,61,62]. These practices represented an improvement of basic science research in the field, including the design of clinical trials according to the histological and molecular information of these tumors.

5.1. Solid biopsy

The amount of tumor tissue obtained from a stereotactic biopsy is limited to 2 to 10 samples[63] of around 1 mm thickness and 10 mm length[64] obtained with a side-cutting biopsy needle[61]. Biopsy fragments are then used to confirm diagnosis by histological review, usually matching a grade 4 glioblastoma or grade 3 astrocytoma, with increased mitotic activity, microvascular proliferation and/or necrosis[65]. The typical immunohistochemistry panels include GFAP, ATRX, p53, neurofilament, ki67, H3K27M, H3K27me3, *IDH* R132H and *BRAF* V600E (rare in DIPG, but with available targeted therapies[66]). For a deeper characterization, histologic findings are complemented with molecular testing. Next-generation sequencing and DNA microarrays are usually used to molecularly confirm the presence or absence of H3 mutation and identify the isoform affected, relevant for patient prognosis.

Performing repeated surgical biopsies in the pons is not recommended, which is a barrier for the assessment of responses to therapy. Developing sensitive liquid biopsy techniques could make such goal feasible.

5.2. Liquid biopsy

Liquid biopsy is a sensitive and minimally invasive tool to analyse the molecular profiling of tumors, enabling precision oncology approaches[67]. The isolation of tumor-derived products in the body fluids of patients with cancer provides information of the whole intratumoral heterogeneity state, prognosis, minimal residual disease and actionable mutations at the moment of sample collection. Sample may be collected from different biofluids, mostly from blood (serum and plasma), and also saliva, urine, and CSF. Several tumor derivatives can be isolated from the sources, such as circulating tumor cells (CTCs), extracellular vesicles (EVs), cell-free DNA (cfDNA) and micro-RNA (miRNA)[68]. The cfDNA found in all biofluids includes the circulating tumor DNA (ctDNA) fraction, which refers to extracellular DNA fragments specifically derived from cancer cells, often having only 50-150 base pairs[69]. Droplet digital PCR (ddPCR) has emerged as one of the most sensitive and cost-effective methodologies for the detection and absolute quantification of the genomic aberrations present in the ctDNA at low allelic frequencies, compared to less sensitive techniques such as Sanger sequencing, quantitative PCR and next generation sequencing platforms[70,71]. The ctDNA isolated from plasma is already being used in the clinics for disease monitoring of extracranial adult cancers, including melanoma, ovarian, lung, breast and colorectal cancer[72]. For patients with glioblastoma multiforme, ctDNA quantification obtained from the CSF may also be used as a biomarker. For brain cancers, blood may not be a suitable source since ctDNA from brain cancers are unfrequently detected in plasma[67]. In contrast, ctDNA derived from CNS malignancies is more abundantly present in the CSF[67]. Once this technique is completely set up, it might represent a true breakthrough for brainstem tumors, for which only limited tissue is available and multiple sampling is not feasible (**Figure 9**).

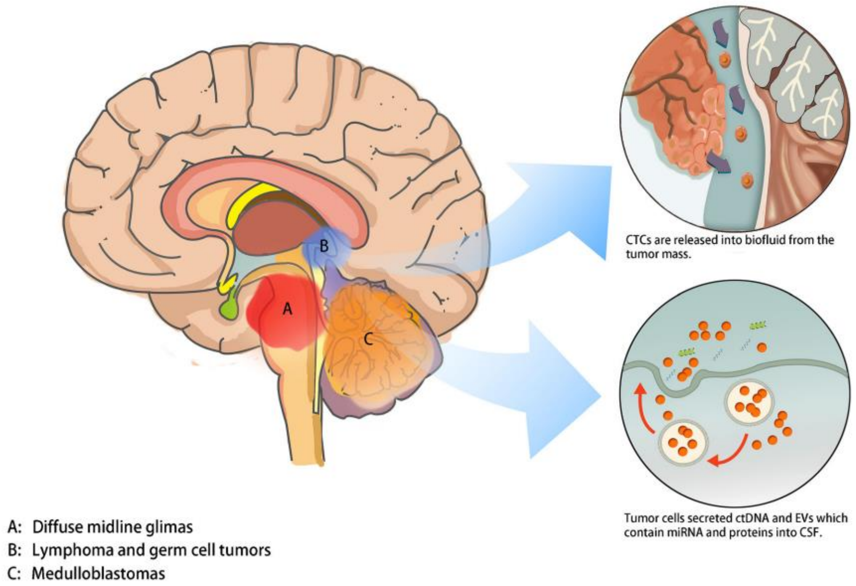

Figure 9. Scheme of the mechanisms for CTCs, ctDNA, and EVs secretion in diffuse midline gliomas, lymphomas and medulloblastomas. Reproduced from reference[73].

The groups led by Liwei Zhang and Chris Jones in The National Clinical Research Center for Neurological Disease of China and The Institute of Cancer Research in UK have developed and validated a clinically relevant and minimally invasive liquid biopsy platform suitable for the detection and quantification of molecular profiling mutations associated with DIPG, especially in *H3F3A*, *HIST1H3B/C*, *ACVR1*, *IDH1*, *PPM1D*, *TP53, ATRX, PIK3CA* and *BRAF*[74,75]. Pan *et al*. applied deep sequencing to the ctDNA isolated from CSF, and analyzed matching tumor and blood DNA from 57 patients with brainstem gliomas, including DIPG[75]. They observed that ctDNA accurately detected tumor-specific alterations found in the primary tumor tissue. In 17% of cases, CSF ctDNA had mutations that were undetectable in the tissue specimen. These results may be due to the sampling bias inherent in traditional biopsy or tumor heterogeneity, highlighting an additional potential benefit of CSF ctDNA over primary tumor DNA[75]. Stallard *et al*. reported that the concentration of H3.3K27M is two-fold higher in the CSF from the lateral ventricles, compared to the concentration in CSF samples from a lumbar puncture, probably due to the location of tumor adjacent to a CSF reservoir[76].

The main goal of the liquid biopsy in DIPG is obtaining biological material at different time points as a clinical approach for measuring longitudinal surveillance of disease and treatment response. To assess this issue, Panditharatna *et al*.

analysed the expression of H3.3K27M in CSF and plasma samples of DIPG patients[77]. They collected serial samples longitudinally through an on-going clinical trial and observed an increase in ctDNA released to CSF in patients who exhibited tumor spread. However, these findings were not replicated in ctDNA from plasma, suggesting a high integrity at the BBB which would preclude access of the ctDNA to the blood, as advanced by Pan *et al*. in 2020[75]. Surprisingly, subsequent analyses detected ctDNA in the plasma after RT, indicating either the potential role of radiation for a temporary disruption of the BBB, or a transiently higher concentration of ctDNA due to RT damaging the tumor producing alterations in tumor architecture, or both[77]. These studies thus may provide suitable methods for assessing tumor response to treatment[77]. Recently, a study reported the serial collection of CSF and blood in patients with DIPG treated with ONC201 in a phase-I trial (NCT03416530) demonstrated the potential use of ctDNA tracking as a supplemental tool for radiographic monitoring. They observed patterns of change in H3K27M levels over time, showing "spikes" preceding progression in many cases in plasma and in CSF. Also, in individual cases, they observed an early reduction in H3K27M levels, predicting long-term clinical response to ONC201, and it did not increase in cases of later-defined pseudo-progression[78] (**Figure 10**).

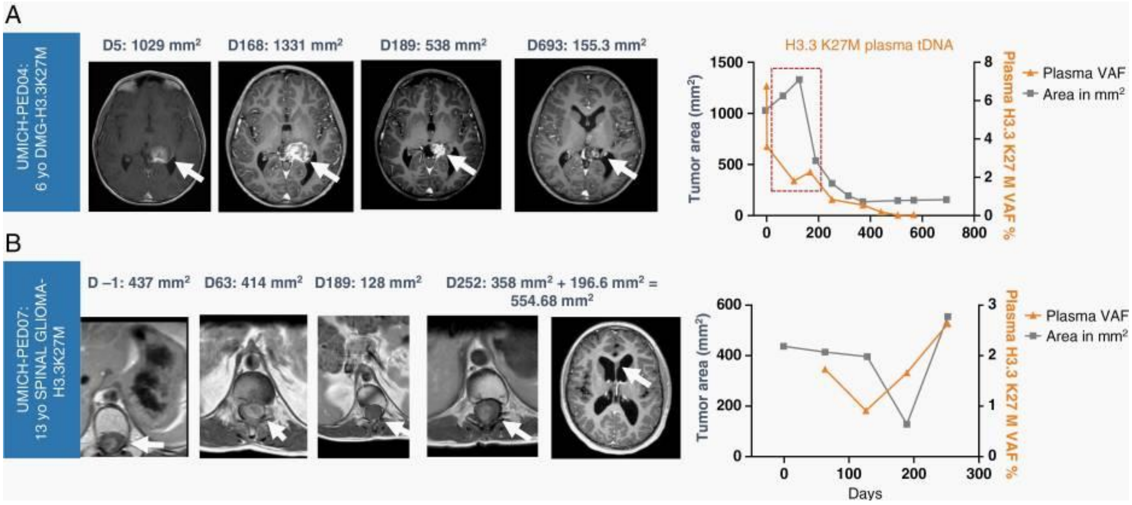

Figure 10. Two cases from the clinical trial monitored by MRI and H3K27M quantification in ctDNA of plasma serial samples. A) Pseudo-progression of tumor measure by MRI is not reflected in H3K27M reduction. B) Samples from a 23-age male. When tumor increase in volume, also of H3K27M in plasma was increased. Reproduced from reference[78].

In my PhD thesis, I attempted to set up a method for serial collection and analysis of CSF samples from mice with intracranial DIPG via the cisterna magna, utilizing the highly sensitive ddPCR technique to detect human histone-3 in the ctDNA of the mice.

6. Preclinical models of DIPG

DIPG and pHGG in general are distinct diseases from adult glioblastoma[11], and thus faithful experimental models are necessary to understand their unique pathophysiology and to test therapeutic strategies. Focused efforts to obtain tumor tissue for research at the time of autopsy and, more recently, biopsy, have helped establish *in vitro* and *in vivo* disease models derived directly from patient material, to test and validate novel treatments.

6.1. *In vitro* models

DIPG research faced serious limitations due to the lack of preclinical tools until Michelle Monje *et al*. at the Stanford University Medical Center established the first pediatric DIPG *in vitro* cell culture and *in vivo* xenograft mouse models using the tumor tissue derived from the autopsy of a patient, in which the pontine histopathology was similar to that of DIPG[79]. Following this research, a few other groups developed primary human DIPG cell lines from tumor samples collected during diagnostic biopsies[80,81], and an orthotopic mouse model using these cells were successfully developed[81].

Although biopsy tissue represents a smaller sample than autopsy tissue, these models may better predict therapeutic response rates in patients, as the cells have not been previously treated[82].

In this PhD project, I used several primary cell cultures derived from DIPG patients and I developed new *in vitro* cultures, with the intention to expand the preclinical pHGG/DIPG platform of the HSJD laboratory.

6.2. *In vivo* models

DMG does not occur spontaneously in mice and the development of xenografts plays a crucial role to study the disease and test preclinical therapies *in vivo*. Prior to 2011, to model DIPG we used glioma cell lines implanted into the pons of immunodeficient mice, with the assumption that the general properties of such gliomas were likely shared in the orthotopic location of the pediatric counterparts[83,84]. There are also reports of murine gliomas induced using carcinogens and transplanted into the mouse brainstem, to induce allografts to serve as DIPG models[85]. Significant advances in the field of mouse xenografts were achieved when Monje *et al*. successfully implanted cultured cells obtained from a DIPG autopsy into immunodeficient mice into the fourth ventricle of mice[79]. The model was the first to be engrafted in mice, although by that time the driver mutations of the sample were not totally known[79]. Soon thereafter, the implementation of stereotactic biopsies for DIPG diagnosis allowed for further development of preclinical models[86]. Our laboratory developed DIPG models from such biopsies. Our most important preclinical model is a DIPG established from the autopsy of a pediatric patient with DIPG who survived less than one month after diagnosis. The original patient tumor was sequenced in[87] (coded HSJD_DIPG007), and holds the mutations H3.3-K27M and *ACVR1*-R206H. This xenograft is HSJD-DIPG-007 (DIPG-007). These cells engraft consistently in the brainstem and cerebellum of NOD.SCID and athymic nude mice. Several preclinical studies have used this xenograft [41,45,87-103], which has been distributed to more than 60 international laboratories.

The second important xenograft at our institution is HSJD-GBM-001 (GBM-001). We established GBM-001 at SJD hospital Barcelona from the biopsy of a cortical tumor of a pediatric 10-year-old patient obtained at the diagnosis of disease. This tumor conserves wild type H3 and has the mutation p.G245S in the gene *TP53*. GBM-001 cells engraft consistently in the brain of NOD.SCID and athymic nude mice. Several publications have used this xenograft [89,104,105], which we have distributed to around 30 international laboratories. This tumor also engrafts in s.c. location (data from SJD laboratory).

A systematic study on the establishment of DIPG models was published by Plessier *et al*[43]. They compared two methods to stablish preclinical models of DIPG, which they called direct (patient-derived) or indirect (cell-derived) xenografting. In the direct model, biopsies were dissociated and directly injected in the thalamus or pons of mice to allow the amplification of the tumor cell pool *in vivo*. In the cell-derived model, biopsies were dissociated, cultured *in vitro*, transduced with luciferase, and then, after several passages required for biobanking, they were injected in the pons of mice and tumor growth was followed up by luminescence (**Figure 11**). They observed that the success rate for both engrafting methods was similar, around 60% for the direct method, and around 55% for the indirect one[43]. A second experience in the development of patient-derived xenografts of DIPG suggested that engraftment was more successful when DIPG samples were directly implanted in mice (68%), rather than after culturing (41%)[106].

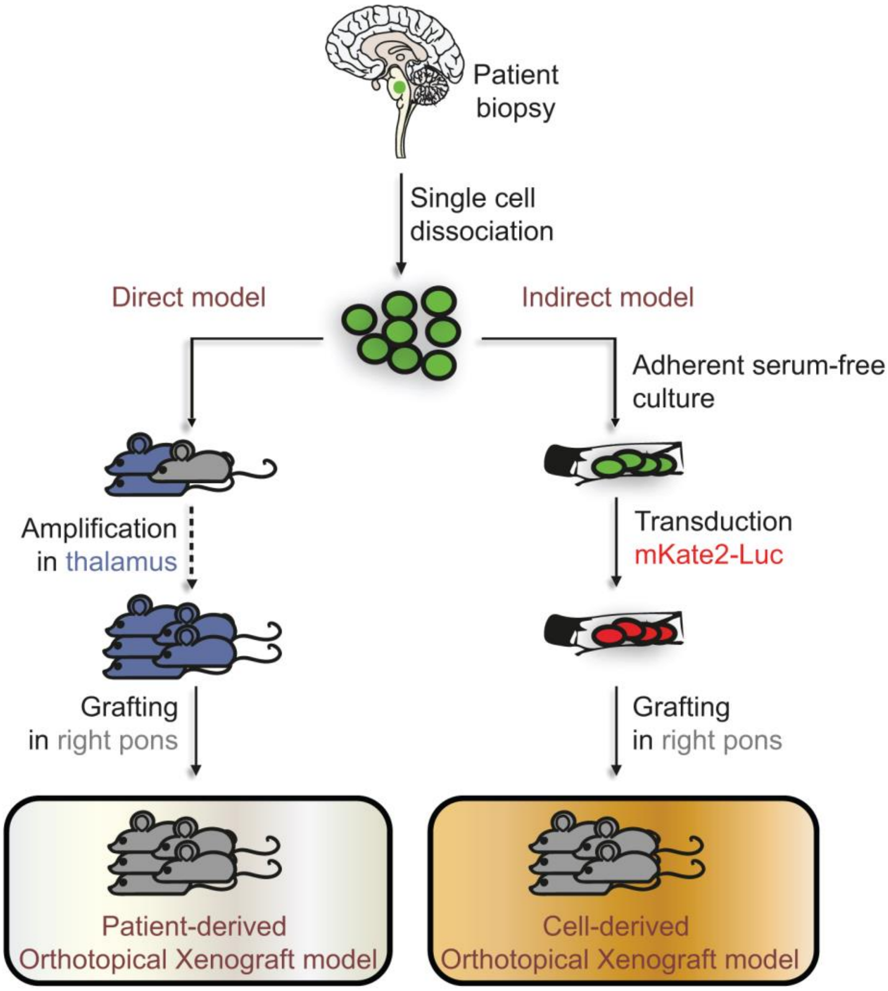

Figure 11. Direct and indirect models developed to study DIPG *in vivo*. For cancer cell expansion, tumors biopsied may be injected directly in the brainstem of mice (PDOX) or cultured and then, inoculated in the pons of mice (CDOX). Reproduced form reference[43].

Xenograft models are not sufficient to address the key question of the cell of origin of DMG. In this regard, GEMMs come with the advantage of arising in the natural microenvironment in immune-proficient animals. The first attempts transfected highly recurrent genetic alterations of DIPG in the brainstem cells of mice, using the RCAS-Tva system. Transfected aberrations were PDGF signalling overexpression, p53 loss and the H3.3K27M mutation. Under specific combinations, mice developed diffuse gliomas in the brainstem, with similar PDGF signalling overexpression, p53 loss and the H3.3 K27M mutation, with high molecular and biological fidelity compared to pediatric DIPG tumors[107-110]. In a different approach, which we could describe as a combination of GEMM and xenograft, human embryonic stem cells were differentiated to a neuronal progenitor lineage and co-transduced with constitutively active *PDGFRA*, *TP53* and H3.3K27M *in vitro* for murine implantation[111]. Mice developed tumors in the brainstem.

Despite being excellent research models, GEMMs come with the disadvantage of lacking part of the heterogeneity observed in patient tumor samples. As an advantage compared to xenografts, they conserve the immune environment. The tumor microenvironment found in DIPG tumors includes low infiltration by immune cells such as Treg, CD4 T cells, NK cells, B cells, monocytes, and eosinophils[112]. Actually, this microenvironment differs significantly from that of the adult glioblastomas, because DIPG shows less infiltration of immune cells[113]. Humanized mouse models may reproduce a more authentic human tumor immune environment, enhancing the potential for accurate drug response prediction in clinical trials and facilitating the discovery of effective therapeutic strategies. As an example, a humanized mouse model, NSG-SGM3-BLT, incorporating NOD-SCID IL2rgnull SCF/GM-CSF/IL3 strain engrafted with human thymus, liver, and hematopoietic stem cells, was utilized to create an orthotopic DIPG model by injecting SF8628, an H3.3K27M mutant cell, into the pons[114] (**Figure 12**).

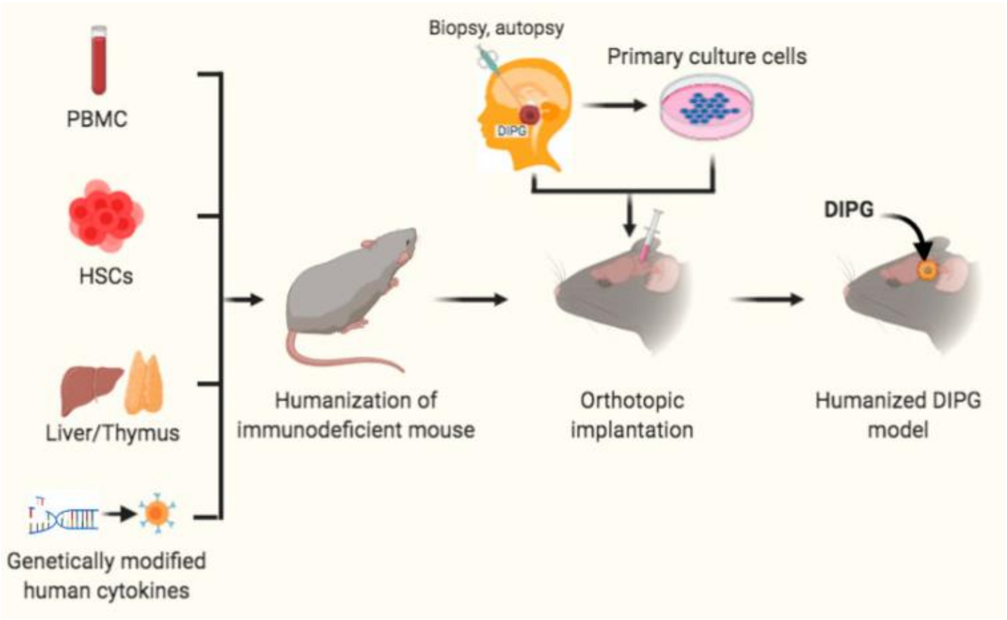

Figure 12. Scheme to humanization of an immunodeficient mice prior to orthotopic intracranial inoculation of DIPG cells, establishing humanized models for DIPG. Reproduced from reference[115].

While significant advances have been made in genetic modelling of DIPG in mice, further models are required to better mirror the human disease concerning new molecules, signalling pathways, and epigenetic factors involved in DIPG tumorigenesis. This advancement is crucial for progressing toward precision medicine, improving treatment effectiveness, and potentially enhancing outcomes for children afflicted by these tumors.

In this PhD work, I refined the methodology for the systematic use of orthotopic intracranial pHGG xenografts, and I attempted to establish additional models. All these xenografts closely recapitulate the original tumor growth patterns observed in patients.

7. Emerging molecularly targeted therapies

As mentioned above, the pHGG subclasses of DMG and diffuse hemispheric gliomas have histone mutations driving their malignant behavior, but these aberrations are still not actionable with treatments. Patients with pHGG have been treated in clinical trials with RTK inhibitors such as erlotinib, vandetanib or dasatinib, but these medicines did not show sufficient activity, alone or in combination with RT. Because the BBB permeability is a primary challenge for therapies, this section will evaluate targeted agents as promising alternatives that may effectively penetrate the BBB for the treatment of these tumors.

7.1. ONC201

ONC201 (7-benzyl-4-(2-methylbenzyl)-1,2,6,7,8,9- hexahydroimidazo [1,2-a]pyrido [3,4-e]pyrimidin- 5(1H)-one), is a small molecule of a novel class of anti-cancer compounds called imipridone. *In vitro*, ONC201 selectively blocks cancer cell growth and induces apoptosis in glioblastoma, breast, lung, colorectal and endometrial cancers, among others[116]. ONC201 was identified as an apoptotic inducer by tumor necrosis factor (TNF)-related apoptosis inducing ligand (TRAIL). ONC201 reportedly acts on the Akt/Erk system, dopamine receptors D2/3 (DRD2/3), and the serine protease “caseynolitic protease P (ClpP)”[116-119] (**Figure 13**).

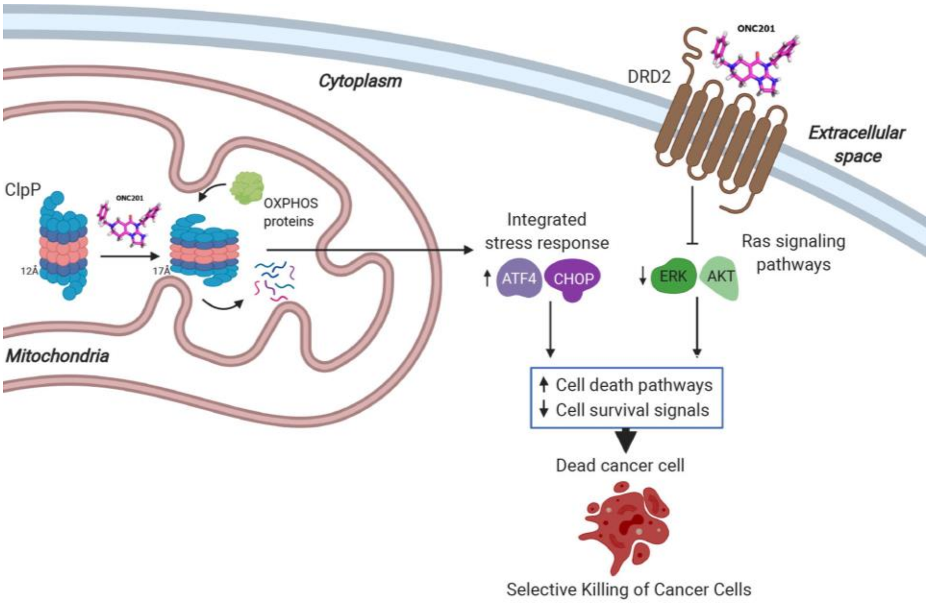

Figure 13. Summary of the initial mechanism of action proposed for ONC201. It shows the interactions with the selective targets molecules of ONC201, in the cytoplasm and mitochondria of a cancer cell. Scheme obtained from Chimerix website.

ONC201 is being evaluated in phase II-III clinical trials for different tumor types, including adult glioblastoma (NCT04629209, NCT04854044)[120]. In the first preclinical studies, researchers demonstrated the therapeutic potential of the imipridone compounds to induce TRAIL-mediated apoptosis in pHGG, resulting in a significant reduction of tumor growth and increased survival in orthotopic xenografts[121-123]. Subsequently, initial clinical experience with ONC201 in patients diagnosed with H3K27M-mutant DIPG was positive, showing significant clinical improvement in one patient[124]. After this case, two phase II clinical trials in recurrent H3K27M-mutant diffuse midline glioma with single agent ONC201 were initiated (NCT03295396; NCT02525692). Recently, Jackson *et al*. tested the combination of ONC201 with the potent brain-penetrant paxalisib (PI3K/Akt inhibitor) for the treatment of H3K27M DIPG in a preclinical study[125]. This study provided preliminary clinical evidence for the commencement of the phase II clinical trial, in participants with DMG (NCT05009992).

The most important study on the mechanism of action of ONC201 in DMG is the one performed at the University of Michigan[126]. Previous studies noted that, unlike IDH1-mutant gliomas, which convert α-ketoglutarate (α-KG) to 2-hydroxyglutarate (2HG) to inhibit histone lysine demethylases and sustain histone lysine methylation, H3K27M-mutant cells utilize α-KG to maintain low H3K27me3 levels[127]. Interestingly, the study led by Carl Koschmann revealed that treatment of H3K27M cells with ONC201 elevated α-KG, due to metabolic disruptions. Using metabolic tracing, they confirmed an increase in the glutamine metabolism in ONC201-treated cells compared to control, producing α-KG and leading to its conversion to 2HG[126]. The final result of this process is an increase in the trimethylation at K27, which would interfere with the normal malignant expansion of DIPG cells[126]. They confirmed the potential of 2HG metabolite as a biomarker for ONC201 response by detecting it in the CSF of patients treated with this drug in the ONC201-014 clinical trial. They reported a positive correlation between an increase of 2HG in CSF and a decrease in radiographic tumor volume detected by MRI[126].

In part of this PhD work, I aimed to replicate the reported preclinical activity of ONC201 in the HSJD DIPG xenografts.

7.2. Targeting the PI3K/Akt/mTOR pathway in pHGG/DIPG

In the integrated molecular meta-analysis of 1000 pHGG/DIPG, Mackay *et al.* detected tumors harboring genetic alterations in at least one of the considered “key biological processes” in 297 of 326 (91.1%) tumor cases[10]. These key processes included well-recognized pathways such as DNA repair (largely driven by *TP53* mutations and activating truncating alterations in *PPM1D*), and heterozygous mutations in a diverse set of genes including those involved in homologous recombination. The study investigated in depth alterations in the components of the RTK-PI3K-MAPK axis through either amplifications of RTKs, activating mutations in *PI3K*, or loss of *PTEN* (either through deletion or promoter methylation). These alterations were present in more than 60% of the pHGG[28]. Activating mutations or amplifications in the PI3K/Akt pathway are shared by approximately 40% of DIPG. Co-segregating with H3.3G34R/V, the predominant mutation at the RTK level was *PDGFRA*. Besides, H3K27M cases were enriched for PI3K/mTOR alterations, predominantly in *PIK3CA* (catalytic protein subunit) and *PIK3R1* (regulatory protein subunit) genes. H3 WT cases had the highest frequency of MAPK alterations, mainly in *BRAF* V600E[10] (**Figure 14**).

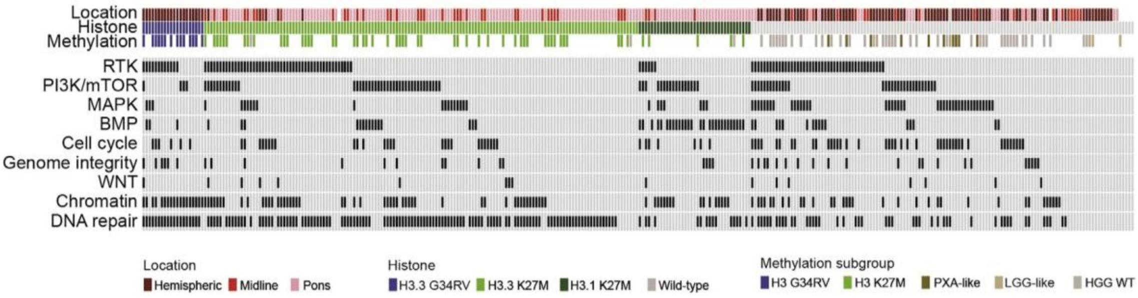

Figure 14. Graphic representation of the somatic alterations in nine commonly targeted pathways in 326 pHGG. Samples are in columns with pathways identified in the rows. Reproduced from reference[10].

7.2.1. The PI3K/Akt/mTOR pathway

The PI3K/Akt pathway plays a crucial role in various cellular processes and is aberrantly activated in cancers, contributing to the occurrence and progression of tumors. It controls hallmarks of cancer, including cell survival, metastasis, angiogenesis and inflammatory factor recruitment[128-131].

The axis of PI3K signalling in cancer begins with the engagement of soluble factors by tyrosine kinase receptors (RTKs) such as PDGFR, MET, EGFR, and IGF-1R, promoting the receptor activation. PI3K is then recruited to plasma membrane-anchored receptors by binding its regulatory subunit (p85), resulting in a conformational change in the catalytic domain of PI3K (p110). Total activated PI3K phosphorylates the third carbon of the phosphatidylinositol-(4,5)-

bisphosphate (PIP_2) and converts it to phosphatidylinositol-(3,4,5)-triphosphate (PIP_3), which activates the 3-phosphoinositide-dependent protein kinase 1 (PDK1). PIP_3 recruits the nodal kinase Akt (also known as protein kinase B, PKB) by direct interaction with its pleckstrin homology (PH) domain[128-131]. At the membrane, activated PDK1 phosphorylates Akt on Thr308 (necessary and sufficient for Akt activation). However, maximal activation requires additional phosphorylation at Ser473 by mTORC2[132,133]. Once Akt is fully activated, it triggers a complex cascade of signals that regulate cell growth, proliferation, survival, and migration. The lipid phosphatase, PTEN, provides instructions as tumor suppressor by catalyzing the degradation of PIP_3 in PIP_2. This dephosphorylation results in inhibition of the Akt signaling pathway and its consequent inactivation[134] (**Figure 15**).

Taken these data together, members of PI3K/Akt pathway are altered in a large number of pHGG/DIPG tumors, leading the over-activation of Akt[135]. Key components of the pathway, PIK3CA and Akt, are actionable with drugs. In this PhD thesis, I have delineated the mutations and copy number variations associated with the PI3K/Akt pathway observed in our pHGG models, along with the upregulation of RNA and the phosphorylation status of the key proteins within this pathway.

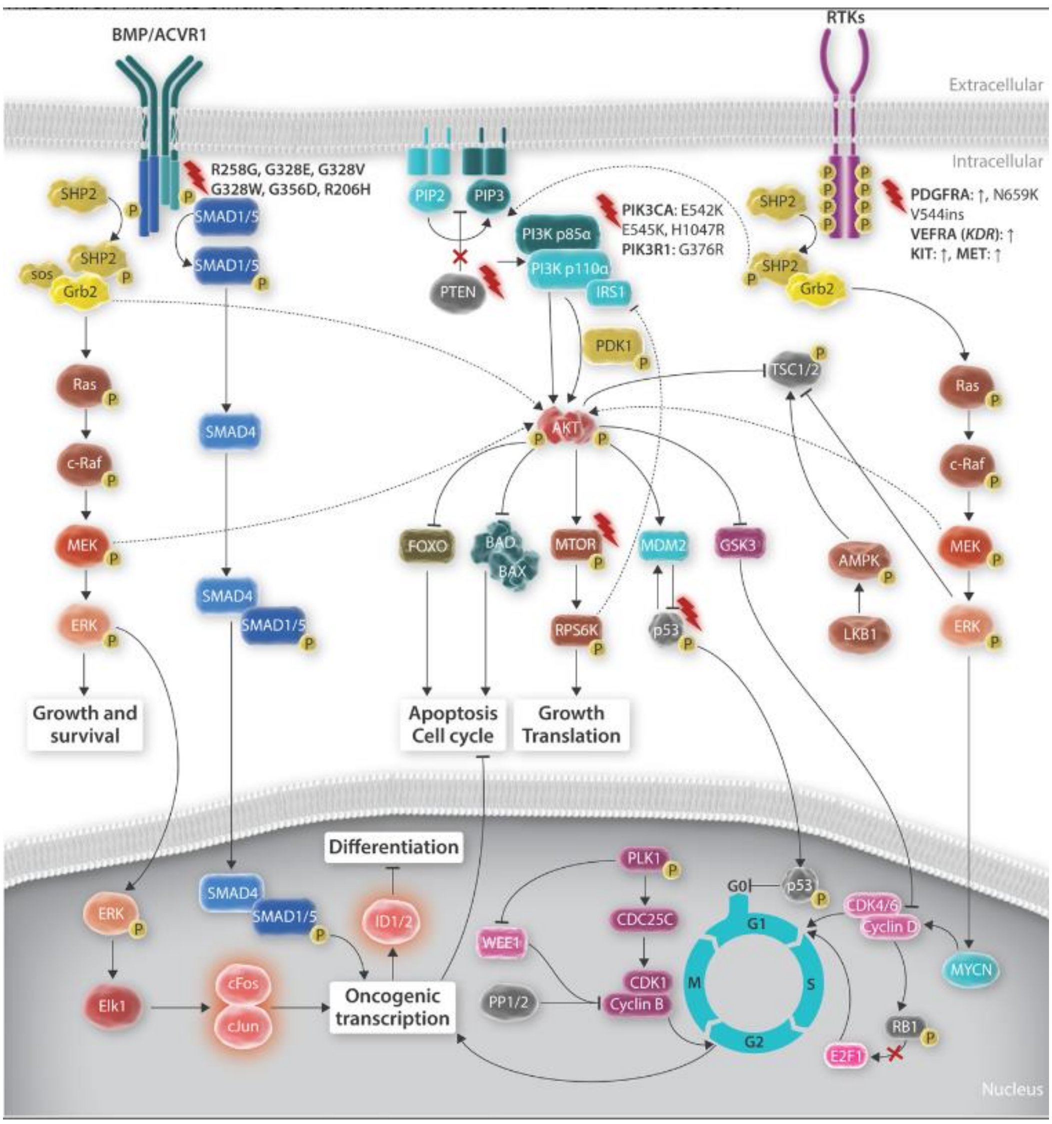

Figure 15. Scheme of the RTK-RAS-PI3K pathway. Soluble growth factors interact with RTKs, triggering PI3K activation, which converts PIP_2 to PIP_3 through phosphorylation. Akt associates with PIP_3 to modulate cell survival, while PTEN dephosphorylates PIP_3, thereby inhibiting Akt signalling. Furthermore, growth factor and RTK interactions also influence cell proliferation and survival by activating Ras in the MAPK pathway. Reproduced from reference[135].

7.2.2. Akt inhibitors: ipatasertib

Ipatasertib (GDC-0068) is an orally bioavailable and highly selective ATP-competitive pan-Akt inhibitor, currently tested in clinical trials for the treatment of several cancers (NCT04650581, NCT06400251, NCT04931342). Its design and chemical optimization was achieved using X-ray structural studies with inhibitors forming complexes with Akt1 and protein kinase A (PKA)[136]. Mechanistically, ipatasertib binds to the ATP pocket of Akt, stabilizing the phosphorylated Akt (phospho Akt or pAkt) in a conformation in which the phosphorylated residues are inaccessible to phosphatases. As a consequence there is dose-dependent accumulation of pAkt, which due to ipatasertib at the ATP pocket becomes inactive, despite presenting higher phosphorylation. As a result, the expression of its downstream targets, such as pS6, pRAS40, pEBP1 and pmTOR is downregulated (**Figure 16**). Preclinical data reported for a broad range of cancer types, including prostate, breast, ovarian, colorectal, and non-small-cell lung cancers have shown that ipatasertib induced tumor growth delay or regression in Akt-activated tumor cells and xenograft models[137]. Tumors with PTEN protein loss, or with genetic mutations in *PTEN* and *PIK3CA* show enhanced sensitivity to ipatasertib, compared to wild type tumors[137-139].

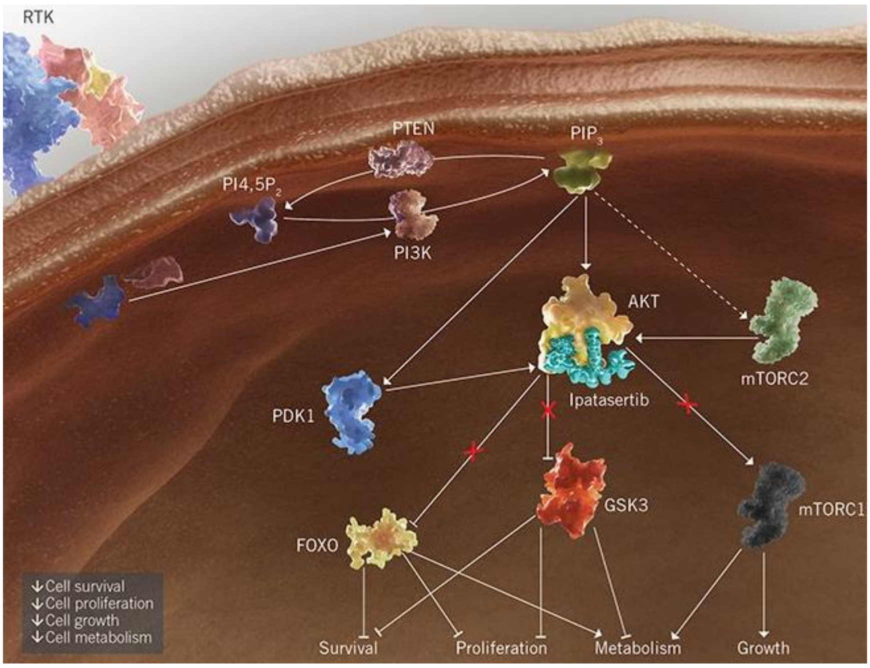

Figure 16. Scheme representing the mechanism of action of ipatasertib, a process that inhibits the Akt activity and downregulates the subsequent signalling pathways in tumor cells, blocking survival, proliferation and migration. Reproduced from Genentech website.

The first-in-human phase I study demonstrated the tolerability of ipatasertib as a monotherapy, with maximum tolerated dosage (MTD) of 600 mg once daily for 21 days continuously followed by 7 days off for adult patients, with diarrhea, nausea, fatigue, and rash as adverse events of treatment[138]. Ipatasertib efficacy is currently being evaluated in clinical trials, alone or in combination with conventional chemotherapy or other target therapies in different adult cancers, including glioblastoma (NCT05554380 and NCT03673787, among others). A phase II trial using ipatasertib combined with paclitaxel as first-line therapy for triple-negative breast cancer demonstrated an increase in the event free survival in patients treated with the combination, compared to patients treated with placebo plus paclitaxel[140]. At present, a Spanish phase Ib multicentre study is recruiting patients with unresectable locally advanced or metastatic HER2-positive breast cancer with tumors harboring *PIK3CA* mutations, to evaluate the safety and clinical activity of the combination of ipatasertib, trastuzumab and pertuzumab (antibodies against HER2) (NCT04253561).

Published data on the activity of ipatasertib in pediatric oncologic patients are limited to the case of a 12-year-old girl with an epithelioid neoplasm harboring a novel fusion between the *LAMTOR1* and *Akt1* genes[141]. Treatment resulted in significant tumor regression after 4 weeks. Unfortunately, imaging repeated following 10 weeks of therapy shown tumor progression event[141]. Currently, a phase II clinical trial for participants aged 12 to 17, and also adults, with metastatic or advanced Akt1/2/3-mutant positive solid tumors is active. The study was designed to evaluate the safety and efficacy of targeted therapies or immunotherapy as single agents or in combinations, depending on patient oncogenotype (NCT04589845).

Despite several studies carrying out the efficacy of ipatasertib, very little is known about its pharmacokinetic profile and distribution into the brain, for either adults or pediatric patients. In this PhD thesis, I investigated the biodistribution of the drug in murine plasma and brain tissues, as well as its therapeutic efficacy in orthotopic DIPG models.

7.2.3. PI3K inhibitors: inavolisib

Because *PIK3CA* is one of the most frequently mutated oncogenes, small molecule inhibitors targeting the PI3K signalling pathway have been developed. The class I isoform PI3Kα is the protein encoded by *PIK3CA* and it is most commonly associated with solid tumors, via gene amplification or activating mutations. Up to 70% of breast cancers present molecular aberrations of the PI3K/Akt/mTOR pathway, with recurrent mutations in *PI3KCA* in more than one third of early breast cancers[142,143]. Hence, several PI3K inhibitors have been designed and tested in preclinical studies, most of them showing anticancer effect[144]. Several phase Ib-II clinical trials are assessing the efficacy of these drugs in patients[145]. Due to their activity against brain metastases of breast cancer, some of them have been investigated for adult GBM. Alpelisib (BYL719) has shown anti-neoplastic effects against glioblastoma cells *in vitro*[146]. Similar findings have been reported for pictilisib (GDC-0941), including its ability to penetrate the BBB in preclinical models[147]. Other PI3K inhibitors have achieved phase II clinical trials, such as buparlisib (BKM-120) or paxalisib (GDC-0084) alone or in combination with other targeted drugs (NCT01349660, NCT03522298, among others). Due to their favorable CNS distribution profiles, some of them have been assayed in patients with pHGG/DIPG. In a first-in-human phase I, paxalisib showed sufficient CNS penetration and stabilized disease in 40% of patients with DIPG recruited for the trial[148].

Inavolisib (GDC-0077) is an orally bioavailable and potent inhibitor of the catalytic alpha isoform of *PIK3CA* (PI3Kα) and has been FDA-approved for the treatment of metastatic *PIK3CA*-mutant breast cancer. Inavolisib exerts its activity by binding to the ATP binding site of PI3K, inhibiting the phosphorylation of PIP_2 to PIP_3. Biochemically, inavolisib is around 300-fold more selective for PI3Kα than for other class I PI3K isoforms (β, δ, and γ) and around 200-fold more selective than for other PIK-related kinases[149-152]. Inavolisib also induces the proteosome-mediated degradation of the oncogenic mutant PI3K-p110α protein (**Figure 17**).

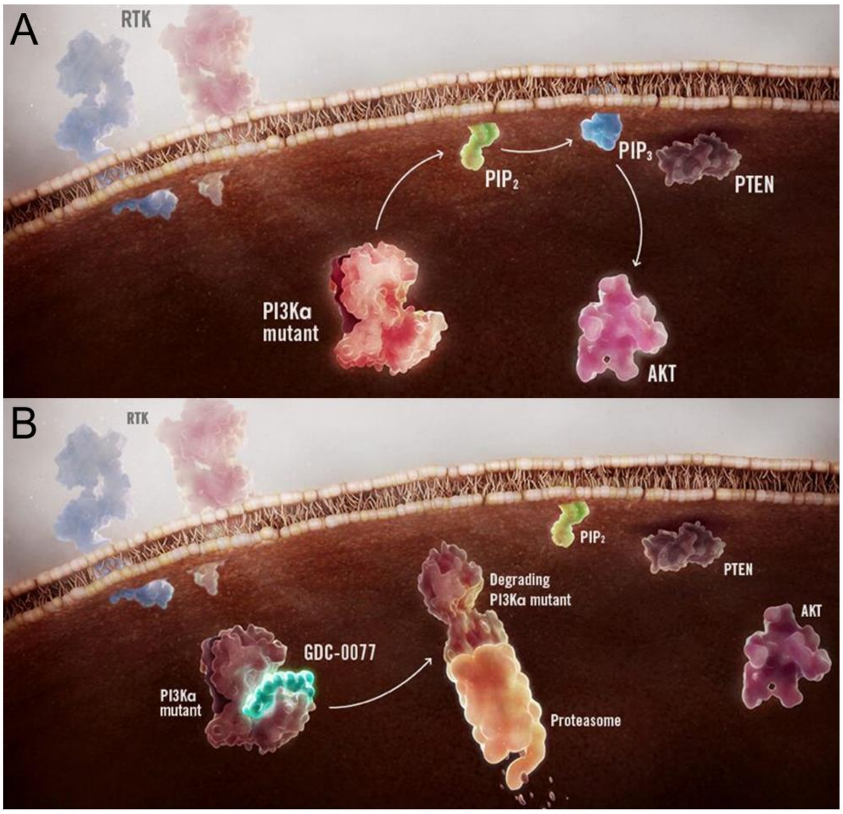

Figure 17. Scheme representing the mechanism of action of inavolisib. A) The PI3K pathway dysregulated caused by mutations in the genes coding for pathway enzymes, including PI3K. B) Inavolisib selectively inhibits mutant PI3Kα, resulting in reduction of pathway activity. Inavolisib binds to the ATP-binding site of PI3Kα, thereby blocking phosphorylation of PIP2 to PIP3 and preventing downstream signalling. Reproduced from the Genentech website.

Inavolisib-treated breast cancer *PIK3CA*-mutant xenografts showed a reduction of the PI3K pathway downstream proteins pAkt, pS6 and pPRAS40, decreased cell proliferation and increased apoptosis[151]. Several clinical trials evaluate inavolisib in patients with *PIK3CA* mutated breast tumors, alone or in combination with other therapies (NCT05646862, NCT05306041, and NCT05894239, among others). A phase III trial of inavolisib or placebo with palbociclib and fulvestrant in patients with *PIK3CA*-mutated, Hormone Receptor+ / HER2– locally advanced/metastatic breast cancer is finished with promising results (NCT04191499). In pediatric patients, a phase II clinical trial is open for different *PIK3CA* mutant-positive tumors (NCT04589845).

In this PhD dissertation, I examined the pharmacokinetics of inavolisib in the plasma and cerebral tissues of mice, along with its anticancer properties in *in vitro* and *in vivo* preclinical models of DIPG harboring (or not) *PIK3CA* mutations.

7.3. Cross-talk with the RAS/MEK/Erk pathway

PI3K/Akt is probably the most interconnected cellular signaling pathway, with points of cross-regulation with all major signal transduction pathways, both in normal and transforming conditions[153]. Initially, RAS-Erk and PI3K-mTOR were conceptualized as separate signaling pathways responding to distinct stimuli. However, early experiments suggested that they might interact and mutually influence each other to coordinate downstream functions[154]. The extent of this interplay and its importance in cancer treatment strategies are increasingly apparent.

A high number of cross-talk, feedback, and feed-forward loops link the PI3K/Akt/mTOR and MAPK/Erk signaling pathways to support mechanisms of cell survival, proliferation, metabolism and motility. The RAS protein, a linker molecule between the MAPK and PI3K pathways, is known to activate RAF by initiating the MAPK cascade, while simultaneously recruiting the p110 catalytic subunit of PI3K to the plasma membrane, leading to the activation of Akt signalling[155] (**Figure 18**). This activation could potentially promote resistance mechanisms against therapies focused on a single pathway. Diverse compensatory responses have been observed as tumors adapt to chemotherapy. For instance, when MAPK signalling is targeted and suppressed, Akt appears to be activated more robustly[156,157].

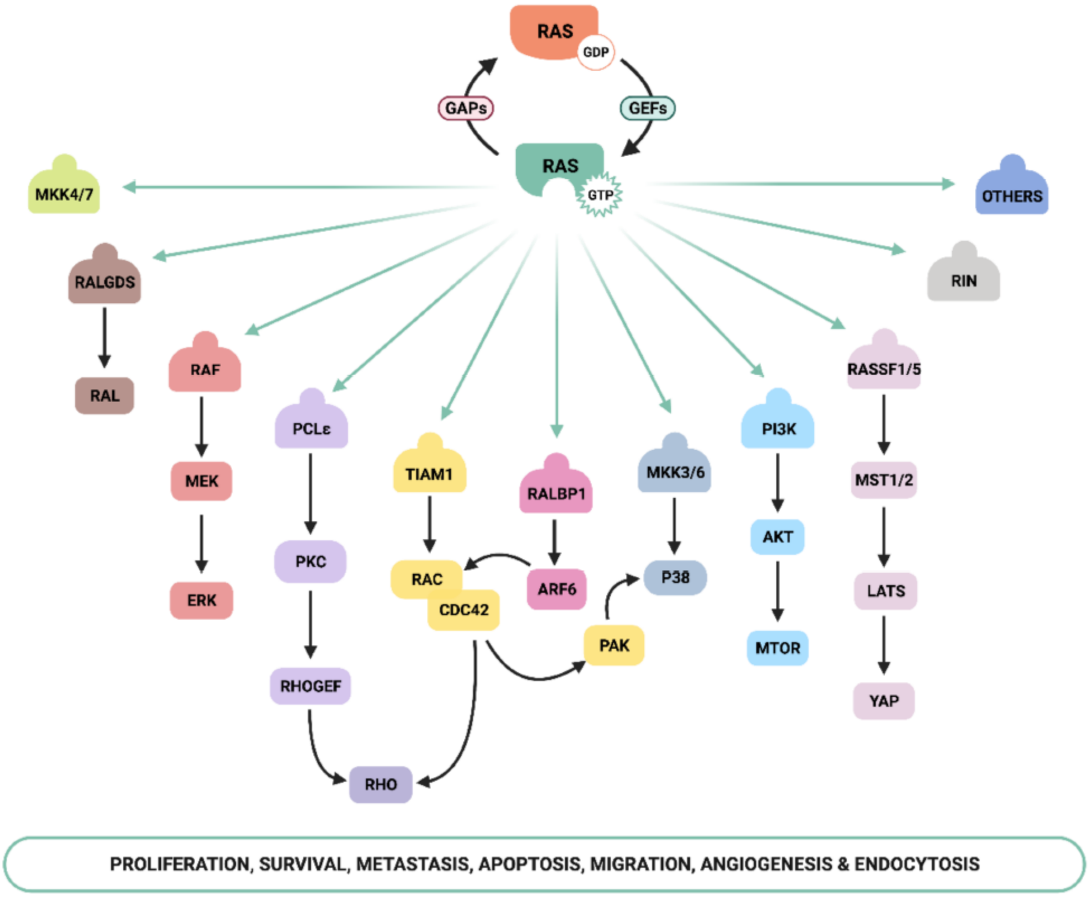

Figure 18. A schematic representation of the different signalling pathways activated by RAS protein, including MAPK/Erk and PI3K/Akt pathways. Reproduced from reference[158].

The simultaneous inhibition of both pathways by combining MEK with PI3K/Akt/mTOR inhibitors has shown promising results in xenografts and GEMM[159]. The selection of specific inhibitors targeting RTKs, Raf or MEK, PI3K or mTOR, or dual PI3K-mTOR inhibitors, should be tailored to each cancer subtype depending on the identified activation of RAS-MAPK and PI3K-mTOR signalling pathways. Therefore, identifying the unique signalling profile in each patient will be crucial for advancing personalized treatment strategies in the future[154].

Trametinib, an FDA and EMA-approved MEK1 and MEK2 inhibitor, in combination with dabrafenib for *BRAF*$^{V600E/K}$ mutation-positive cancer, has shown promise in low-grade gliomas in pediatric patients[160]. Combining PI3K and MEK/ERK pathway inhibitors has shown efficacy in DIPG models[161-163]. Perifosine and trametinib together induced significant apoptosis and cell cycle arrest in DIPG cultures[162]. Ongoing trials like PNOC021 are exploring combinations of trametinib with everolimus in pediatric and young adult patients with recurrent gliomas, highlighting the potential of dual pathway targeting in treating these tumors (NCT04485559).

In my PhD thesis, I investigated the status of the RAS/MEK/Erk signalling pathway in our primary models of pHGG. Building on this rationale and previous *in vitro* findings from our group, I also evaluated the anticancer activity, toxicity, and survival impact of trametinib in DIPG xenografts.

Chapter 2. Hypothesis and aims

This thesis aims to contribute to the field of therapy development in pHGG. These deadly cancers infiltrate structures such as the brainstem, cerebellum, thalamus and spinal cord, rendering surgery unfeasible. All pharmacological approaches for patients with pHGG have failed in clinical trials, partly because the BBB remains intact, impeding CNS drug distribution, and partly because we have not evaluated the right medicines. The RTK-PI3K-MAPK axis is altered in more than 60% of the pHGG. Activating mutations and amplifications of the PI3K/Akt pathway are shared by 40% of DIPG. These tumorigenic alterations are likely actionable with novel small molecule medicines, provided that such medicines cross the BBB.

In this thesis work, I hypothesized that the inhibition of the PI3K/Akt pathway is a therapeutic strategy for human pHGG xenografts in mice bearing mutations in the gene *PIK3CA*. To address my hypothesis, the main objectives of my thesis were:

i. To establish preclinical pHGG models covering most of the subclasses of the disease, and to compare the methods of paraffin tissue analysis, liquid biopsy of CSF and mouse weight monitoring to assess tumor burden in mice with orthotopic pHGG xenografts. I will develop ddPCR methods to quantify allele frequencies of human genes *H3F3A* K27M, *H3F3A* G34R and *ACVR1* R206H in mouse samples. I will use the developed methods to evaluate the preclinical activity of potential therapeutic candidates, including *ACVR1* inhibitors, ONC201, trametinib and taselisib in DIPG xenografts.
ii. To characterize the PI3K/Akt/mTOR pathway in preclinical pHGG models and in patients diagnosed with DIPG. In preclinical models, I will use next generation sequencing (NGS) technology to detect the alterations in the PI3K/Akt pathway. I will measure RNA and protein expression related to the activation of the pathway. In samples from patients diagnosed with pHGG, I will analyse markers of the pathway using immunoassays.
iii. To test the efficacy and CNS drug distribution of the PI3K/Akt pathway inhibitors ipatasertib and inavolisib in pHGG xenografts. I will evaluate the pharmacodynamic profile of both candidate drugs in DIPG models *in vitro*. I will measure their preclinical efficacy, selectivity for the tumor and distribution in the blood, CSF and brain in mice bearing DIPG intracranial xenografts with conserved BBB.

Chapter 3. Materials and methods

1. Next generation sequencing (NGS)

We analyzed the recurrent genomic alterations of pHGG through whole exosome sequencing using the next generation sequencing (NGS) technology, developed at Macrogen, Inc. We prepared the samples (primary pHGG cultures), by extracting DNA using the Gentra Peregen kit (Qiagen, Hilden, Germany). The sequencing was performed at Macrogen (Seoul, South Korea) and we analyzed the results. The Twist NGS Target Enrichment workflow was solution-based system utilizing ultra-long 120 mer biotinylated cDNA baits – to capture regions of interest, enriching them out of NGS genomic fragment library. Target Enrichment and Sequencing A genomic DNA (gDNA) library was prepared from 50 ng of input gDNA using the Twist Library Preparation EF Kit 2.0 (96 samples, PN 104207) with full-length combinatorial dual index TruSeq-compatible Y-adapters (Illumina) according to the Twist Bioscience Library Protocol. Macrogen used 50 ng of each gDNA diluted with EB Buffer and sheared to a target peak size of 200 bp with the fragmentation enzyme. Fragmentation was followed by end-repair and the addition of ‘A’ tail. Twist UDI index adapters were then ligated to the fragments.

After assessing the efficiency of ligation, the adapter-ligated product was PCR amplified. For exome capture, each hybridization reaction required 1500 ng of indexed libraries, made by pooling equal amounts from 8 individual libraries, and mixed with Hybridization mix, Twist Human Core Exome probe, RefSeq probe, Blocker solution, and Universal Blocker, Hybridization Enhancer according to the Twist library preparation protocol. The final purified PCR product was quantified by qPCR according to the qPCR Quantification Protocol Guide (KAPA Library Quantification kits for Illumina Sequencing platforms).

Then, Macrogen sequenced samples using the NovaSeqX platform (Illumina, San Diego, USA). Based on the BAM file, variant genotyping for each sample was performed with Haplotype Caller of GATK. They also filtered variants with VariantFiltration of GATK Tool for hard-filtering variant calls based on certain criteria. Filtered variants were annotated with SnpEff and filtered with dbSNP and SNPs from the 1000 genome project.

The calculation method for the copy number value was based on the log2. Thus, we defined the range as follows: log2 < -1.1: 0 (DEL); log2 < -0.25: 1 (LOSS); 0.2 ≤ log2 < 0.7: 3 (GAIN); log2 ≥ 0.7: 4 (AMP). To analyze the single nucleotide variants (SNVs), we filtered the raw variants excluding synonymous variants, and those variants detected elsewhere apart from exonic regions. We used the Integrative Genomics Viewer (IGV) Variants to visualize them to discard potential artifacts. The remaining variants were manually filtered using databases including Franklin (https://franklin.genoox.com/clinical-db), Varsome (https://varsome.com/), and ClinVar (http://www.ncbi.nlm.nih.gov/clinvar). We classified the variants according to the AMP/ASCO/CAP Standards and Guidelines for Somatic Variant Interpretation and Reporting[164].

2. Establishment of DIPG primary cell cultures

To establish new primary cultures from pHGG samples, we acquired fresh tissue samples from surgical biopsies and post-mortem examinations of patients at Hospital Sant Joan de Deu (HSJD, Barcelona, Spain). These patients were diagnosed based on clinical symptoms, MRI scans and presence of H3 K27M alteration by immunohistochemistry and molecular approaches. Collection of patient material was conducted with informed consent and approved by the institutional review board. Newly established cell cultures were designated HSJD-DIPG or HSJD-DMG (due to the new nomenclature of the disease) followed by sequential numbers, each corresponding to a different patient.

Tumor samples underwent dissociation in a buffer containing DNase I and collagenase type IV at 37°C for 15 minutes. The resulting tumor cells were isolated by centrifugation and cultured in stem cell media, consisting of Dulbecco's Modified Eagle Medium: Nutrient Mixture F12, Neurobasal-A Medium, HEPES buffer solution 1 M, MEM sodium pyruvate solution 100 nM, MEM non-essential amino acids solution 10 mM, Glutamax-I supplement and antibiotic-antimycotic, all from Life Technologies. The media was supplemented with B-27 supplement from Life Technologies, 20 ng/mL recombinant human-EGF, 20 ng/mL recombinant human-FGF, 20 ng/mL recombinant human-PDGF-AA and 20 ng/mL recombinant human PDGF-BB from Peprotech (Waltham, MA, USA), and 2 µg/mL heparin from Sigma Aldrich (Saint Louis, MI, USA). The cultures were incubated at 37ºC, 5% CO2 and 95% humidity.

As quality control, we genotyped our cell models for 10 human-specific short tandem repeat (STR) markers fingerprinting tumor cells and patients blood DNA.

For clarity purposes, we abbreviated cell identifications in the thesis by omitting the institutional code HSJD.

3. Immunofluorescence

For the immunofluorescence (IF) studies, we used frozen tumorspheres, formalin-fixed, paraffin-embedded (FFPE) biopsies/necropsies and Geltrex-embedded blood-brain barrier endothelial cells hCMEC/D3.

To detect the expression of stem cell markers and histone 3 proteins alterations in cancer cells, we used frozen down tumorspheres in culture using medium to ensure optimal cutting temperature (OCT, Sakura Finetek, Torrance, CA, USA). We sectioned the frozen blocks including the tumorspheres using a cryostat (HM525NX, Epredia, Kalamazoo, MI, USA) and fixed them in silane-coating pre-treated slides (Starfrost, Lowestoft, UK) with 4% paraformaldehyde (PFA) for 1 h at 4 ºC. We blocked the samples with 1% bovine serum albumin (BSA) and permeabilized the cells with 0.1% Triton X-100 solution (all Sigma) for improving the penetration of the antibody during 45 min at 4 ºC. Then, we incubated the slides overnight, at 4 ºC, in the presence of primary antibodies (**Table 1**).

For phospho-Akt immunolabelling in post-mortem human samples with DIPG, we used FFPE specimens. Sections (6 µm-thick) were prepared and subjected to sodium citrate (pH 6) heat-mediated antigen retrieval. Plasma membrane labelling with wheat germ agglutinin (WGA, W11261, Invitrogen) was performed to ensure specific Akt marking within the cells. Subsequently, samples were blocked using Novolink Polymer Protein Block (RE7200-CE, Leica Biosystems, Newcastle, UK) reagent for 45 minutes at room temperature (RT) in a humid chamber. Following blocking, slides were incubated overnight at 4 ºC with primary antibody (**Table 1**).

For angiogenesis studies, we performed IF of the endothelial marker CD31 in hCMEC/D3 cells embedded in Geltrex, treated as described in the section "*In vitro capillary-like tubule formation assay"*. We used 8-well glass chamber slides and treated them with conditioned media for 18 h. Then, we fixed the gels with 80% methanol and 20% DMSO for 30 min at RT. We rehydrated with 50% methanol and 50% PBS for 1 h at RT. Finally, we added 20% methanol and 80% PBS followed by a permeabilization process with 0.1% Tween 20-PBS at RT for 1 h. We next processed the samples with blocking solution (10% FBS, 5% BSA in PBS) for 2-4 h. We washed with 0.1% Tween 20-TBS (TBS-T) for 1 h and added the primary antibody rabbit anti-human-CD31 diluted in blocking solution at 4 ºC overnight (**Table 1**).

Table 1. Primary antibodies used in the IF assays. Table provides detailed information relative to the dilution, source and the reference of each antibody.

Antibody	Working dilution	Source	Reference	Company
Glial fibrilary acidic protein (GFAP)	1:200	Rabbit	RP014	Diagnostic Biosystems
Nestin	1:500	Rabbit	ABD69	Millipore
H3.3 K27me3	1:1000	Mouse	07-449	Millipore
H3.3 K27M	1:1000	Rabbit	31-1175-00	Revmab
H3.3 G34R	1:200	Rabbit	31-1120-00	Revmab
Phospho-Akt (Ser473)	1:50	Rabbit	#9271S	Cell Signaling
CD31	1:200	Rabbit	Ab32457	Abcam

In all the studies, the following day we washed the preparations with PBS and added the secondary antibody goat anti-rabbit-Alexa-488 (A11008, 1:1000, Invitrogen, Waltham, MA, USA) or anti-rabbit-Alexa-594 (A21207, 1:1000, Invitrogen), for 1 h at RT. We counterstained cell nuclei with DAPI and mounted the samples with Vectashield mounting medium (Vectorlabs, Newark, CA, USA). We obtained images using the Leica THUNDER Imager Live cell and 3D Assay software.

4. Immunohistochemistry (IHC)

We sectioned (6 µm-thick) FFPE blocks of human and mouse brains for immunostaining analysis and stained with hematoxylin and eosin (H&E). Sodium citrate (pH 6) heat-mediated antigen retrieval was performed before the incubation with antibodies (**Table 2**). Primary antibodies were diluted into Leica antibody diluent and incubated for 1 h at RT. We used the anti-human nuclear antigen to stain human nuclei in mouse xenografts. Novocastra Novolink polymer detection systems kit (Leica Biosystems RE-7150) was used for the staining. We performed automatic staining using Leica Bond-MAX autostainer (Leica Biosystems). We quantified the images using Image J software (NIH, Bethesda, MD, USA).

Table 2. Primary antibodies used for IHC assays. Table provides detailed information relative to the dilution and the reference of each antibody.

Antibody	Working dilution	Reference	Company
Human nuclear antigen	1:200	MAB4383	Sigma
H3.3 K27me3	1:500	31-1062-00	Revmab
H3.3 K27M	1:500	31-1175-00	Revmab
H3.3 G34R	1:50	31-1120-00	Revmab
Phospho-S6 (Ser240/244)	1:2000	#5364S	Cell Signaling

5. Immunoblotting analysis

To perform the western blot assay of histones, we used a histone extraction kit (OP-0006-100, Epigentek, Farmingdale, NY, USA) to lyse samples and extract the histones. We separated histone lysates (1 µg) in 15% polyacrylamide gels, transferred them to nitrocellulose membranes and blocked them with tris-buffered saline containing 5% BSA. Then, we incubated them overnight at 4 ºC with primary antibodies (**Table 3**). Human Histone 3 (H3) served as the housekeeping gene to loading control.

Table 3. Primary antibodies used for histone protein analysis by western blot assay. Table provides detailed information relative to dilution, source and reference of each antibody.

Antibody	Working dilution	Source	Reference	Company
H3.3 K27me3	1:1000	Mouse	07-449	Millipore
H3	1:2000	Rabbit	#4499	Cell Signaling
H3.3 K27M	1:1500	Rabbit	31-1175-00	Revmab
H3.3 G34R	1:1000	Rabbit	31-1120-00	Revmab

For the studies related to the analysis of cytoplasmic proteins, we lysed samples using lysis buffer containing Tris-HCl pH 7.4, NaCl 5M, 1% triton 100X, EDTA 0.5M, ortovanadate, NaF, sodium pyrophosphate (all Sigma), and free-protease inhibitor (Roche Diagnosis, Burgess Hill, UK). We quantified proteins with Bradford Protein Assay (Sigma). A range of 40-70 ng of proteins was loaded on 10-15% polyacrylamide gel for electrophoresis. The gel-separated proteins were transferred to nitrocellulose membranes. They were incubated overnight at 4 ºC with primary antibody (

Table 4). Human GAPDH served as the housekeeping gene to normalization and quantification.

Table 4. Primary antibodies used for cytoplasmic protein analysis by western blot assay. Table provides detailed information relative to the dilution, source and the reference of each antibody.

Antibody	Working dilution	Source	Reference	Company
Akt	1:1000	Rabbit	#9272	Cell Signaling
Phospho-Akt (Ser473)	1:1000	Rabbit	#9271	Cell Signaling
PRAS40	1:1000	Rabbit	#2691	Cell Signaling
Phospho-PRAS40 (Thr246)	1:1000	Rabbit	#13175	Cell Signaling
S6 Kinase	1:1000	Rabbit	#2217S	Cell Signaling
Phospho-S6 (Ser240/244)	1:750	Rabbit	#5364	Cell Signaling
Cleaved Caspase-3	1:500	Rabbit	#9664	Cell Signaling
Cleaved Caspase-7	1:500	Rabbit	#8438	Cell Signaling
Cleaved PARP	1:1000	Rabbit	#9541	Cell Signaling
GAPDH	1:50000	Mouse	#97166	Cell Signaling

Next day, for both histone and cytoplasmic proteins, we incubated the membranes with the secondary antibody (926-32211 and 926-68070, LI-COR) for 1 h at RT. Fluorescence signal was detected in Odissey CLx Imagin Systems (LI-COR, Biosciences). Images obtained were quantified using Image J software.

6. Pre-amplification PCR

To maximize the detection of mutated DNA sequences in mouse samples (**Table 5**) we performed a pre-amplification reaction. We used a commercial master mix (Q5 hot start high-fidelity, New England Biolabs, Ipswich, MA, USA), with 50 nM of forward and reverse primers. Primer sequences for *H3F3A* gene were those published for use in human liquid biopsies[165]. We set the thermocycler (A24811, Applied Biosystems, Foster City, CA, USA) at 98 ºC for 3 min, followed by 12 thermal cycles (98 ºC for 10 s, 67 ºC for 3 min, 72 ºC for 30 s) and an extension at 72 ºC for 2 min. We stored the PCR products diluted 1:5 with Tris EDTA buffer pH 8.0 (Sigma) to inactivate the Q5 polymerase[166]. As positive control, we used 1 ng of gDNA from DIPG-007 cells. We used sterile water as blank.

Table 5. Samples used in pre-amplification studies. Table provides detailed information relative to the ctDNA source and amount employed for the studies.

Material	ctDNA source	ctDNA loaded (ng)	Type of Experiment
DIPG cells	gDNA	2.26	LOD and linearity of ddPCR technique after pre-amplification PCR
DIPG cells	Supernatant	20	Tumor burden *in vitro*
Mouse	CSF	2 to 4	Pre-amplification PCR standardization and tumor burden *in vivo*
Mouse	Plasma	2 to 4	Pre-amplification PCR standardization

To perform the ddPCR reactions, we loaded 10 µL of pre-amplified ctDNA, in duplicates.

7. Quantification of human DNA by droplet digital PCR (ddPCR)

We used digital droplet polymerase chain reactions (ddPCR) to quantify mutated sequences in the gDNA of cancer cell pellets and mouse tissues, and in the circulating tumor DNA (ctDNA) of cell culture supernatants, mouse CSF and plasma. For the amplification of *H3F3A* K27M and G34R, we used a commercially available assay (dHsaMDV2510510 and dHsaMDS2512308 respectively, Bio-Rad, Hercules, CA, USA), and the thermocycler protocol of the manufacturer. For *ACVR1* R206H, the sequence-specific primers and fluorescent locked nucleic acid probes for amplification were from Applied Biosystem, previously reported by Carvalho *et al*[167].

Following the amplifications, we used a digital droplet reader (QX200, Bio-Rad) to count droplets for wild type (VIC/HEX-tagged) and mutant (FAM-tagged) alleles. We stablished the threshold of positivity using the pHGG cell line DIPG-007, which carries the mutations *H3F3A* K27M and *ACVR1* R206H. We used non-template (blank) control sample to detect false positive droplets.

Before using the techniques in our experiments, we calculated their sensitivity. To establish the lower limit of detection (LOD), we performed three independent (inter-assay) calibration experiments using gDNA obtained from DIPG-007 cells. In each experiment, we quantified the amount (ng) of *H3F3A* and *ACVR1* in serial DNA dilutions in triplicates (intra-assay). The maximum amount of DNA loaded in the ddPCR was 20.4 ng and 2.26 ng for pre-amplified studies. We defined the LOD as the lowest DNA amount (ng) per reaction detected with at least three positive droplets in all the triplicates in the three independent calibration experiments, for both wild type (WT) and mutated alleles of each gene.

To evaluate the linearity of the technique, we considered acceptable linearity when the slope for both analyzed genes was statistically different from zero and $R^2 > 0.9$.

In our studies, we represented ddPCR data as the total amount (ng) of human *H3F3A* (K27M and WT alleles). To calculate the ng obtained from the ddPCR results, we followed the next rules:

- *H3F3A* K27M (ng): ConcMut_original x Vreaction x 1 haploid genome
- *H3F3A* WT (ng): ConcWT_original x Vreaction x 1 haploid genome
- *H3F3A* total (ng): *H3F3A* K27M (ng) + *H3F3A* WT (ng),

being ConcMut_original the concentration of K27M allele of the gene obtained from ddPCR reaction, in copies/µl; ConcWT_original the concentration of WT allele of the gene obtained from ddPCR reaction, in copies/µl; Vreaction the volume used for the reaction mix; and the mass of 1 haploid genome was set at 0.003 ng[74].

8. Real time quantitative polymerase chain reaction (RT-qPCR)

This assay aimed to examine the expression of various genes in DIPG cells or tissues, as well as in normal brain tissue. Samples (cells or tissues) were lysed and homogenized using TRIzol Reagent (Thermo Fisher), and RNA was extracted following the standard protocol. The RNA was then reverse-transcribed using Superscript II reverse transcriptase (Thermo Fisher).

The quantitative RT-qPCR was performed using Syber Green qPCR Master Mix on an Applied Biosystems QuantStudio 6 Flex instrument. Each reaction contained 1 µg of RNA, and the expression levels of the genes were measured in triplicate (**Table 6**). Human GAPDH served as the housekeeping gene, and differential expression was determined using the delta Ct method.

Table 6. cDNA primers used for qPCR assay. Table provides detailed information relative to the gene, primers sequences and the reference of each.

Gene	**Primer Fw (5’ → 3’)**	**Primer Rv (3’ → 5’)**	**Supplier**
PIK3CA	GAGTAACAGACTATCTAGAGAC	AGAAAATCTTTCTCCTGCTC	Sigma
PIK3R1	AAGAAGACTTGAAGAAGCAG	TCAACCACATCAAGTATTGG	Sigma
AKT1	AAGTACTCTTTCCAGACCC	TTCTCCAGCTTGAGGTC	Sigma
AKT2	CACCATGAATGAGGTGAATAC	CTACGGAGGAAGTTGTTTAAG	Sigma
AKT3	TTCTTCTCTGGAGTAAACTGG	TTGCTGACATTTTTCAGGTG	Sigma
EGFR	TTGCTGACATTTTTCAGGTG	CAGCCACCTCCTGGATGGTCT	Sigma
FGFR1	AGGAACTTTTCAAGCTGC	CATCATGTACAGCTCGTTG	Sigma
PDGFRα	TCAAGTTCCTTCATCCATTC	CATCCACTCAATATCAGGAAG	Sigma
GAPDH	ATGGAAATCCCATCACCATCT	CGCCCCACTTGATTTTGG	IDT

For the purpose of analyzing many genes at the same time, we used the TaqMan™ Array Human PI3K Signaling (Applied Biosystems) to analyse gene expression associated with the PI3K signalling pathway in our cell models. This array facilitates the evaluation of multiple genes involved in the PI3K pathway simultaneously, enabling high-throughput and reproducible results.

9. Drug activity assays

We characterized the cytotoxicity of the drugs *in vitro* with the compound [3-(4, 5-dimethylthiazol-2-yl)-5-(3-carboxymethoxyphenyl)-2-(4-sulfophenyl)-2H-tetrazolium] or MTS assay (Promega, Fitchburg, WI, USA). In general, we plated 3000 cells/well on 96-well plates and incubated at 37ºC under 5% CO_2 for 24 h. Then, we added the drugs to each well in concentrations ranging typically 0.000001 to 100 µM (1:10 serial dilutions) in sextuplicates, and incubated between 3 days (72 h) to 6 days. The MTS compound was metabolized by proliferating cells. The absorbance was measured at 490 nm on a Multimode Plate Reader Infinite M nano (Tecan) for cell activity quantification.

The viability of the cells in each well was determined by normalizing absorbance values to those of cells untreated (or treated with vehicle control), following background subtraction. The half maximal inhibitory concentration, IC_{50}, was calculated using a log (inhibitor) vs. response curve, with a variable slope (four-parameter) model. All analyses were performed using Prism 9 software (GraphPad).

10. Colony formation assay

We performed this assay to study the ability of a single cell to grow into a colony, in the presence or absence of ipatasertib and inavolisib inhibitors. To perform the study, we followed the procedure standardized previously by Zhang, L., *et al*[168]. Briefly, we plated five thousand cells/well on 6-well plates coated with 2.5% matrigel and incubated at 37 ºC under 5% CO_2 overnight. Next day, we treated the cells with either vehicle or five concentrations of ipatasertib or inavolisib (0.1, 0.5, 1, 5 and 10 µM or 0.01, 0.05, 0.1, 0.5 and 1 µM, respectively) for 48 h. At the end of treatment, we replaced the medium with fresh TSM, and cells were incubated for 10 days. Then, we fixed the cells with 4% PFA for 30 min we stained them with Coomassie stain. The experiments were repeated three times. We quantified the colonies using iBright Software Analysis.

11. *In vitro* capillary-like tubule formation assay

Because the PI3K/Akt pathway promotes the angiogenesis, we performed an assay with human brain endothelial hCMEC/D3 cells to evaluate the antiangiogenic ability of its inhibitors. Briefly, we coated 24-well plates with 100 µL matrigel and we plated 5.5 x 10^4 cells per well. We treated the cells at different conditions, according to the following schedule:

- Group 1: endothelial medium, as negative control
- Group 2: TSM medium, as negative control
- Group 3: supernatant (SN) obtained from DIPG-007 cells, to ensure the presence of DIPG secretome as positive control
- Group 4: DIPG-007 SN with inavolisib 1 µM
- Group 5: DIPG-007 SN with inavolisib 10 µM
- Group 6: DIPG-007 SN with ipatasertib 1 µM
- Group 7: DIPG-007 SN with ipatasertib 10 µM

Cells were incubated at 37 ºC under 5% CO_2 for 24 h. Then, we quantified the formation of a capillary-like network by digital image analysis using Image J software angiogenesis analyser pluging. We repeated the assay four times.

12. Flow cytometry analysis

We used a flow cytometry assay (NovoCyte flow cytometry system, ACEA Biosciences, San Diego, CA, US) to measure cell apoptosis. Briefly, after treatment with different concentrations of inavolisib (0.01, 0.1 and 1 µM) for 24 h, we collected DIPG-007 cells (1 x 10^6) and fixed them with ethanol 70% overnight at -20ºC. Then, we washed the cells with PBS and incubated with PBS containing 1% FBS and 1% BSA for 30 min on ice. Next, we incubated cells with anti-cleaved PARP antibody (1:400, #5625S, Cell Signaling) for 20 min at 4ºC, and with secondary antibody (Anti-rabbit-Alexa 488, 1:500, ab150077 Abcam) for 20 min at 4ºC in the dark. We analysed the percentage of apoptotic cells using the NovoExpress software (ACEA Biosciences).

13. Animal models

We established xenografts by orthotopic injection in athymic nude mice (Envigo, Barcelona, Spain)[89]. We performed animal experimentation according to the Institutional and European guidelines (EU Directive 2010/63/EU) and with the approval of the local animal care and use committee (Comité Ético de Experimentación Animal at Universidad de Barcelona, protocol 135/11). Briefly, on the day before the inoculation in mice, we disaggregated the tumorspheres, counted cells, and cultured them overnight. The next morning, we isolated the growing spheres by mild centrifugation and kept the pellets in 1.5 mL tubes on ice. We inoculated nude mice in the fourth ventricle with a dispersion of 5×10^5 cells in 5 µL matrigel (BD Biosciences, San Diego, CA, USA). For this procedure, mice were anesthetized with a mixture of 100 mg/kg ketamine and 10 mg/kg xylazine, intraperitoneal, and immobilized in a stereotaxic apparatus (Stoelting, Wood Dale, IL), in direct contact with a heating pad to maintain body temperature. We loaded the cells in a 50 µL glass syringe (1705 RN Rheodyne, Hamilton, Bonaduz, Switzerland) with a 22 G dull needle, and injected them through a burr hole in the skull, performed with a drill (Microtorque II, Harvard Apparatus, Cambridge, MA, USA)[89]. After recovery, we weighed the mice weekly throughout the study time. Mice achieved experimental endpoint at the time of 20% body weight loss due to tumor progression (using the maximum weight as a reference). We sacrificed the mice by decapitation and fixed the brains for 24 h in formalin (4% paraformaldehyde, Sigma), until processing in paraffin for further studies.

14. Collection of CSF from mice

We extracted the CSF from the cisterna magna of the mice. In brief, we anesthetized the mice, secured them in a stereotaxic apparatus, and obtained the CSF (2-10 µL) using a flame-sharpened glass microcapillary (P0549, Sigma). Subsequently, we stored the samples at -80 ºC until analysis.

We evaluated the feasibility of collecting serial CSF samples to assess cancer cell DNA as a marker of tumor progression *in vivo*. We used five DIPG-007-inoculated mice, from each of which we obtained 2-3 serial CSF samples. After each procedure for CSF sampling, we sutured the skin and injected subcutaneously 1 mL of 0.9% NaCl to prevent de-hydration, as previously described[169]. We monitored animal weight three times per week. After CSF collection at the last scheduled time point, we sacrificed the mice and processed the brains for histopathology. We analyzed CSF and brain samples as in the previous experiments, using pre-amplification for the CSF.

15. Preclinical efficacy studies in mice

For the studies in xenografts, we injected DIPG-007 cells (5 x 10^5 cells in 5 µL matrigel) into the pons of athymic mice as described above. In general, after completing the treatments, we monitored the animals until the endpoint. We then built the survival curves with the data obtained. At the endpoint, we collected brains of selected animals for quality control purposes (to ensure animals died of diffuse infiltrative DIPG).

15.1. M4K2009 and M4K2163

I evaluated the anti-tumor activity of two small molecule inhibitors of ALK2 (*ACVR1*), M4K2009 and M4K2163 that target the intracellular kinase activity of the ALK2 protein[170,171].

For M4K2009, DIPG-007 (*ACVR1* mutant) tumor-bearing mice were distributed in four groups for the efficacy analysis and we treated once daily, 5 days-on and 2 days-off (oral administration), starting day 32 post-tumor inoculation, according to the following regimens:

- Group 1: vehicle controls (0.5% Tween20 + 0.25% carboxymethylcellulose (CMC)), n = 13
- Group 2: 100 mg/kg M4K2009 for two 2-week cycles, with a 1-week break between cycles, n = 12
- Group 3: 50 mg/kg M4K2009 for two 2-week cycles, with a 1-week break between cycles, n = 13
- Group 4: 100 mg/kg M4K2009 for three 2-week cycles, with a 1-week break between cycles.

For M4K2163, DIPG-007 tumor-bearing mice were also distributed in four groups for the efficacy analysis and we treated once daily, 5 days-on and 2 days-off (oral administration), starting day 36 after tumor inoculation, according to the following schedule:

- Group 1: vehicle-treated control (0.5% Tween20 + 0.25% CMC) , n = 13
- Group 2: 100 mg/kg M4K2163 for 4 weeks, n = 13
- Group 3: 50 mg/kg M4K2163 for 4 weeks, n = 12
- Group 4: 100 mg/kg M4K2163 for 8 weeks, n = 10

15.2. Trametinib

We conducted an *in vivo* efficacy study using DIPG-007 tumor-bearing mice to test trametinib, given its high sensitivity in this cell model *in vitro* (data from Dr. Nagore G. Olaciregui).

DIPG-007 tumor-bearing mice were distributed in two groups for the efficacy analysis and were treated during four weeks, five times per week (5 days-on and 2 days-off), starting day 46 after tumor inoculation, according to the following regimen:

- Group 1: Control group, received vehicle (10% DMSO/40% PEG300/50% PBS), n = 13
- Group 2: 1 mg/kg trametinib for 4 weeks, oral administration, n = 13

15.3. ONC201

As mentioned in the Introduction, ONC201 appeared in the scientific literature around 2013, identified as small molecule compound with potential anti-cancer properties. Since then, research on ONC201 has progressed, leading to preclinical and clinical studies in DIPG tumors. When clinical trials emerged for patients diagnosed with DIPG, we performed a preclinical study to evaluate the efficacy of the drug in DIPG-007 tumor-bearing mice.

DIPG-007 tumor-bearing mice were distributed in two groups for the efficacy analysis and were treated during four weeks, once weekly, according to the following regimen:

- Group 1: vehicle-treated controls (20:80 DMSO/PBS), n = 5
- Group 2: 100 mg/kg ONC201 for 4 weeks, intraperitoneal administration, starting day 32 after tumor inoculation, n = 5

15.4. Taselisib

The decision to test taselisib in the DIPG-007 xenograft model was based on the genetic profile of this cell model.

For the experiment, DIPG-007 tumor-bearing mice were distributed in two groups for the efficacy analysis and were treated during four weeks, 5 days-on and 2 days-off, starting treatments at day 31, according to the following regimen:

- Group 1: vehicle-treated controls (0.25% CMC - 0.5% Tween20), n = 15
- Group 2: 11.25 mg/kg taselisib for 4 weeks, oral administration, n = 15

15.5. Inavolisib

Because taselisib showed significant toxicity in our studies using DIPG xenografts, we opted to evaluate another PI3K inhibitor, inavolisib, which has shown reduced toxicity in preclinical studies involving breast cancer[151].

For inavolisib, DIPG-007 tumor-bearing athymic nude mice were stratified in two groups for the survival study and were treated once daily (oral administration, 5 days-on 2 days-off) for 2 cycles of 2 weeks-on 1 week-off, starting treatments at day 32, according to the following schedule:

- Group 1: control group, received no treatment (only vehicle 0.25% CMC - 0.5% Tween20), n = 5
- Group 2: inavolisib 50 mg/kg for 20 days, n = 5

These mice were monitored until the endpoint and we obtained the survival curves.

Next, we performed a study to address the pharmacodynamics of inavolisib. DIPG-007 tumor-bearing athymic nude mice were stratified in two groups, and were treated once daily (oral administration), starting treatments at day 23, according to the following schedule:

- Group 1: control group, received no treatment (only vehicle), n = 5
- Group 2: inavolisib 50 mg/kg for 14 days, n = 5

The last day of treatment, 2 h after last dose, we collected CSF and brains from treated and control mice to analyse tumor burden. We processed brains in PFA 4% and stored CSF at -80ºC for tumor burden studies.

15.6. Ipatasertib

For ipatasertib, DIPG-007 tumor-bearing nod.scid mice were distributed in three groups for the efficacy analysis and were treated once daily (oral administration, 5 days-on 2 days-off), starting treatments at day 32, according to the following schedule:

- Group 1: control group, received no treatment, n = 16
- Group 2: ipatasertib 25 mg/kg for 25 days, n = 16
- Group 3: ipatasertib 100 mg/kg for 25 days, n = 11

From groups 1 and 2, we sacrificed 5 mice 2 h after the last dose of treatment, and we collected brains to evaluate tumor burden. We included the remaining alive mice in the survival study.

16. Pharmacokinetics

16.1. Inavolisib

To study the CNS and plasma biodistribution profile of ipatasertib, we treated 30 non-tumor three-week-old female athymic nude mice (Envigo, Barcelona, Spain) with a single dose of 50 mg/kg inavolisib by oral gavage. We took blood, brain and CSF samples at 0.25, 0.5, 1, 2, 6, 12, 18, and 24 h post-dose of 3-4 mice for each time point. We collected blood samples (approximately 800 µL) from each animal by terminal cardiac puncture into tubes containing heparin as an anticoagulant and centrifuged at 1500–2000 g to isolate plasma. The analysis of the accumulation data of inavolisib was carried out by liquid chromatography-tandem mass spectrometry (LC-MS/MS) by our collaborator, Dr. Nora Unceta at the Department of Analytical Chemistry, Universidad del País Vasco, Spain.

16.2. Ipatasertib

To study the CNS and plasma biodistribution profile of ipatasertib, we treated 24 non-tumor three-week-old female athymic nude mice (Envigo) with a single dose of 100 mg/kg ipatasertib by oral gavage. We took blood and brain samples in triplicate at 0.25, 0.5, 1, 2, 6, 12, 18, and 24 h post-dose. We collected blood samples (approximately 800 µL) from each animal by terminal cardiac puncture into tubes containing heparin as an anticoagulant and centrifuged at 1500–2000 g to isolate plasma. We analysed the accumulation data of ipatasertib by LC-MS/MS at the laboratories of our collaborator Jordan Gonçalves at Oncodesign (formerly Bertin Pharma) in Orleans, France.

Chapter 4. Results I

Methods to follow up disease of pHGG xenografts and application to studies of drug activity.

1. Primary pHGG cultures and xenografts

In my PhD project I have handled (either established or maintained, and characterized) 15 primary pHGG cultures derived from 15 patients at Hospital SJD (**Table 7**). Thirteen of them were from biopsies at diagnosis and two from post-mortem samples. The overall success rate for establishing cultures from autopsies was 10.5% (2/19) and from biopsies was 22% (13/59). The mutation *H3F3A* K27M appeared in the majority (13/15) of the established cell models, the mutation *H3F3A G34R* appeared in one line, and one was H3 wild type pHGG

Table 7. Patient-derived pHGG models stablished at HSJD Barcelona.

Primary culture ID	**Type of sample**	**Sex**	**Age at diagnosis (years)**	**Tumor location**	***H3* mutation**	***ACVR1* mutation**	***PT53* mutation**	**Current passage number**	**Culture phenotype**	**Xenograft**
DIPG-007	Necropsy	M	10	Pons	*H3F3A K27M*	R206H	wild type	166	Spheroids	Yes
DIPG-008	Biopsy	M	7	Pons	*H3F3A K27M*	wild type	wild type	15	Spheroids	No
DIPG-011	Biopsy	F	3	Pons	*H3F3A K27M*	wild type	wild type	76	Spheroids	No
DIPG-012	Biopsy	M	10	Pons	*H3F3A K27M*	wild type	R273C	51	Spheroids	No
DIPG-013	Biopsy	F	6	Pons	*H3F3A K27M*	wild type	R248Q	54	Spheroids	No
DIPG-014	Biopsy	F	8	Pons	*H3F3A K27M*	wild type	wild type	48	Spheroids	No
DIPG-017	Biopsy	M	9	Pons	*H3F3A K27M*	wild type	R158P	47	Spheroids	No
DIPG-018	Biopsy	F	3	Pons	*HIST1H3B K27M*	R258G	wild type	7	Adherent	Not tested
DIPG-019	Biopsy	M	6	Pons	*H3F3A K27M*	wild type	wild type	23	Spheroids	No
DIPG-021	Biopsy	F	6	Pons	*H3F3A K27M*	wild type	C135Y	28	Adherent	No
DMG-003	Biopsy	F	6	Pons	*H3F3A K27M*	wild type	R248Q	5	Spheroids	Yes
DMG-005	Necropsy	F	7	Medulla	*H3F3A K27M*	wild type	R273C	12	Spheroids	Yes
DMG-007	Biopsy	F	6	Pons	*H3F3A K27M*	wild type	wild type	5	Spheroids	Not tested
DMG-008	Biopsy	F	7	Pons	*H3F3A K27M*	wild type	wild type	2	Spheroids	Not tested
GBM-001	Biopsy	F	11	Right frontal lobe	wild type	wild type	G245S	74	Spheroids	Yes
GBM-002	Biopsy	M	15	Left hemisphere	*H3F3A G34R*	wild type	wild type	43	Adherent	Yes

In this PhD work, we characterized 12 of the established cultures using whole exome sequencing. The most relevant findings of the analysis are represented in **Figure 19**. Results on H3 mutations confirmed those reported through clinical diagnosis work for each patient at our institution (HSJD) and previously published results on some of the cultures, such as DIPG-007, with the activating mutation in *ACVR1* R206H[172] (**Figure 19**).

We addressed whether the established HSJD cells had co-occurrence of histone-3 driver mutations with alterations in cell cycle regulatory genes, such as *TP53* or *PPM1D*. This event has been well documented[173]. We found that eight of the cell models had *TP53* mutations, resulting in protein inactivation. The H3.3K27M/*TP53*-mutant genotype is associated with a poorer prognosis of the patients, as evidenced by reduced tumor responsiveness to irradiation and earlier recurrence post-radiotherapy[173]. We observed that the majority of the cells which did not harbor *TP53* alterations, such as DIPG-007, DIPG-008 and DIPG-014, presented a gain-of-function mutation in *PPM1D*. This mutation modulates the *TP53*-mediated cell-cycle checkpoint, thereby conferring a p53-deficient phenotype in the absence of *TP53* mutations[174].

We expected to find mutations or alterations in genes within the PI3K/Akt/mTOR pathway, including *PIK3CA* or *PTEN*, which can enhance and accelerate tumor growth but are not strictly necessary for tumor initiation[10,175]. We found one model with PIK3CA missense mutation and one with PTEN mutation.

In the only cell model with wild-type H3, GBM-001, we observed the absence of *IDH1/2* mutations, along with copy number gains in *MYC* and *MYCN,* matching well with H3-wildtype and IDH-wildtype pHGG subgroup of diffuse pediatric-type high-grade gliomas[2].

In the only cell model with H3 G34R mutation, GBM-002, there was also an *ATRX* nonsense mutation, producing a loss of ATRX expression[176], which is the characteristic phenotypic profile of this entity described in the 5th CNS WHO classification for these subgroup of pediatric gliomas[2]. This mutation results in the loss of ATRX protein expression due to the nonsense-mediated mRNA decay pathway, which facilitates the swift breakdown of mRNAs that contain premature stop codons[177].

Genomic alterations in the *PDGFRA* receptor were restricted to the cells established from two tumors located in the cerebral hemispheres, GBM-001 and GBM-002. This alteration is more common in hemispheric cancers than in the brainstem and is typically associated with older patient age[178].

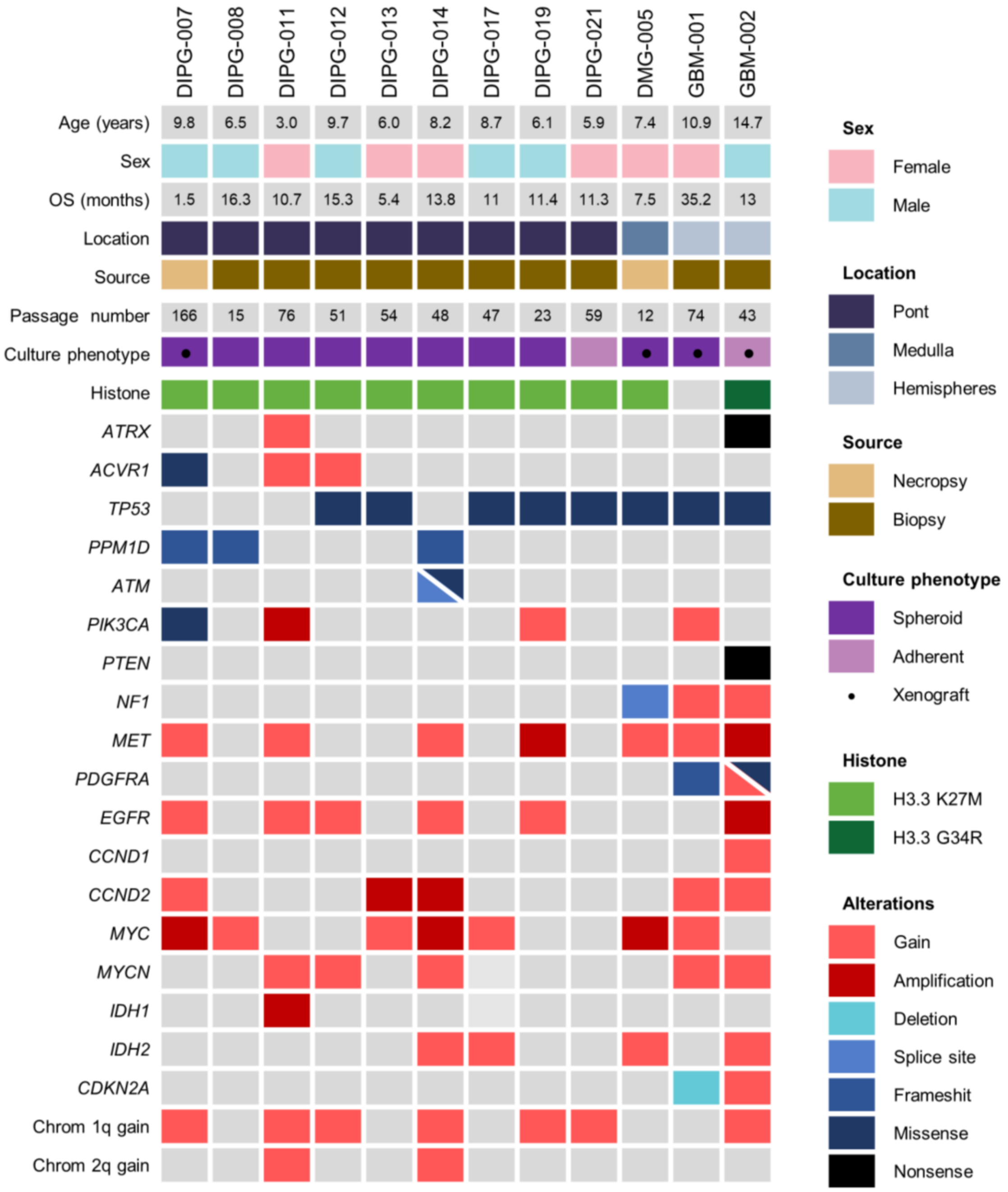

Figure 19. Whole-exome sequencing of HSJD pHGG cultures. An Oncoprint visualizes an integrated annotation of single-nucleotide variants and DNA copy-number alterations in patient-

derived models of pHGG (n = 12). In the representation, samples are displayed in columns, and genes are listed in rows. The passage number represents the passage we have currently managed to reach in the laboratory. Clinicopathological and molecular annotations are illustrated with bars as indicated in the accompanying key.

Most cultures grew as spheroids and expressed the cancer stem cell marker nestin and the astrocytic marker GFAP (**Figure 20A**). Immunostaining of histone mutations H3.3 K27M and H3.3 G34R corresponded to the genetic phenotype of the models and histone trimethylation in K27 was absent in the H3 K27M mutants (**Figure 20A**). We confirmed the results using immunoblotting (**Figure 20B**).

We established four xenografts that grow diffusely in the mouse brain and are lethal for the mice (**Figure 20C**). According to the molecular classification of pHGG, two of them, DIPG-007 and DMG-005, are DMG H3 K27-altered; one, GBM-001 is a diffuse pediatric-type high-grade glioma H3-wildtype and IDH-wild type; and the last, GBM-002, is a diffuse hemispheric glioma H3 G34-mutant. Tumors grow infiltrating the brainstem of mice, with 100% take rate. The median survival of is 90 days for DIPG-007 (median of 5 experiments, range 76-116 days, n = 49), 51 days for DMG-005 (3 experiments, 42-84 days, n = 15), 32 days for GBM-001 (2 experiments, 29-35 days, n = 15) and 233 days for GBM-002 (one experiment, 166-282 days, n = 8) (**Figure 20C**).

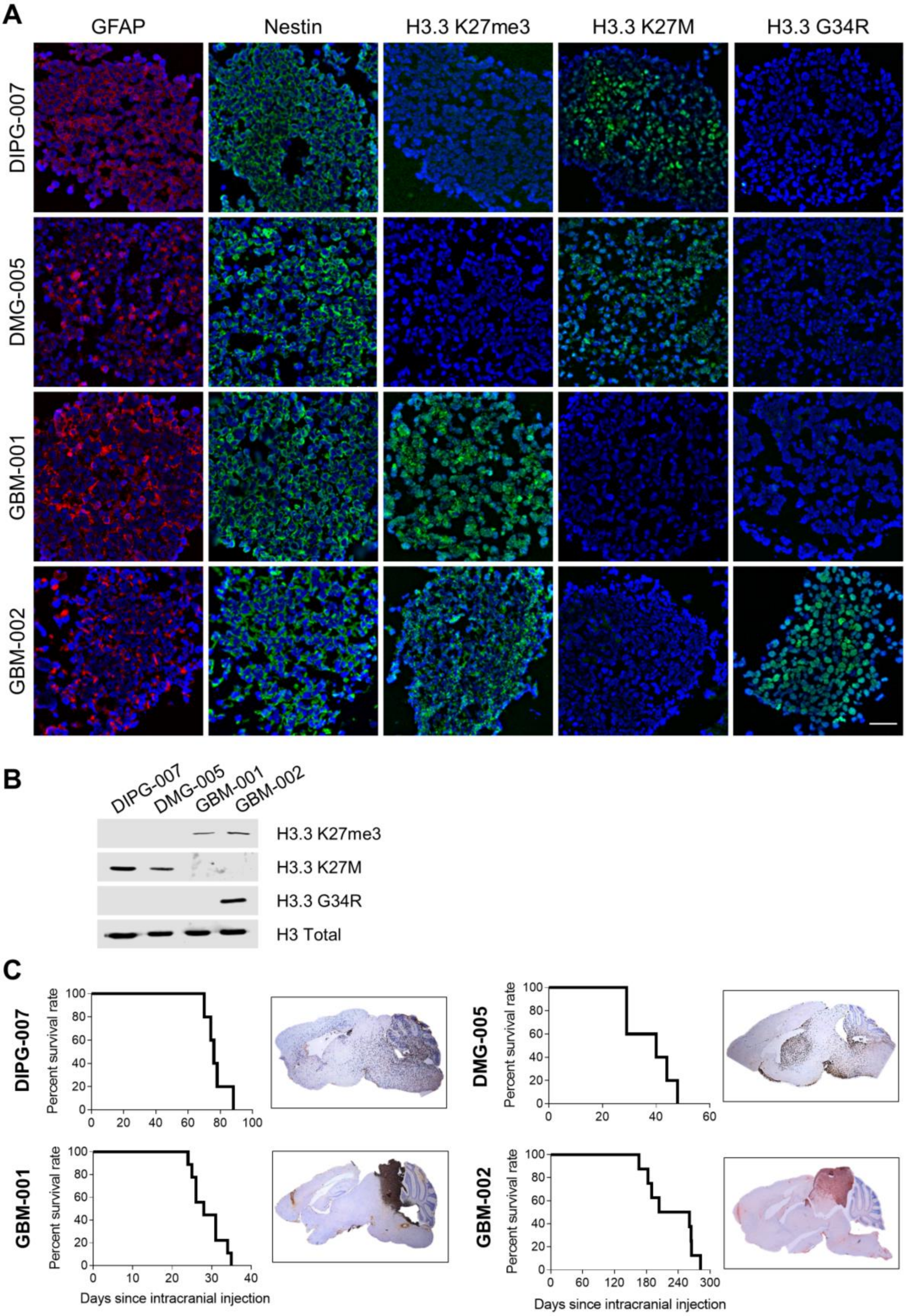

Figure 20. Characterization of pHGG cultures and xenografts**.** (A) Immunofluorescence of GFAP (red), nestin (green), H3.3 K27M (color), H3.3 G34R (color) in DIPG-007, GBM-001, GBM-002 and DMG-005 tumorspheres (x40 magnification, scale bar = 50 µm). (B) Immunoblotting of the mutant proteins H3.3 K27M and H3.3 G34R, trimethylated H3K27M (H3K27me3) and H3 as

loading control in pHGG cultures. (C) Representative Kaplan Meier curves of DIPG-007, GBM-001, GBM-002 and DMG-005 orthotopic xenografts in mice, and representative FFPE slides showing staining of human cells (human nuclei, brown) at endpoint.

We confirmed histone H3.3 K27me3 and histone H3 mutation status by immunohistochemistry in the brain tumor xenografts and in the corresponding patient biopsies (**Figure 21**).

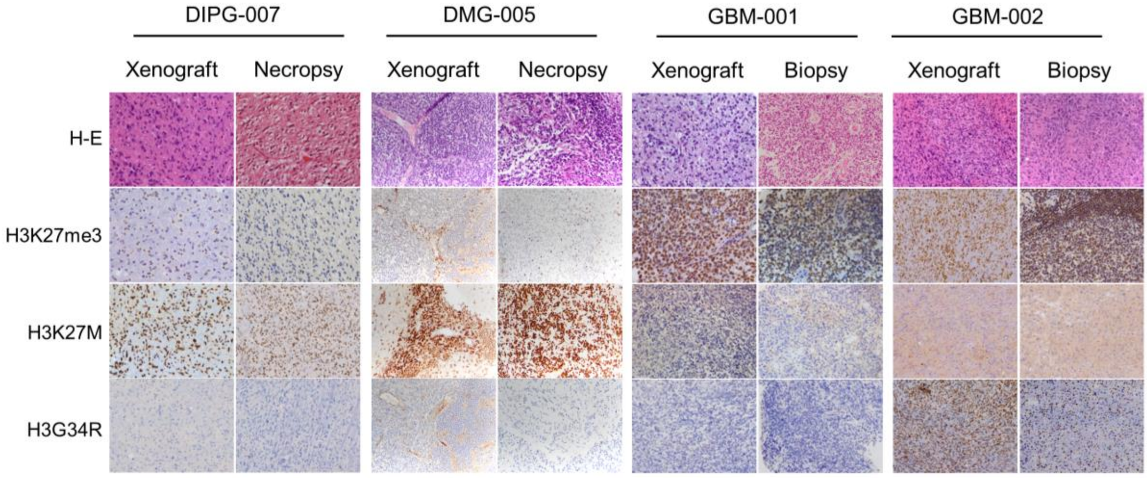

Figure 21. Histological characterization of orthotopic patient-derived pHGG xenograft models and matching patient biopsies. Hematoxylin and eosin, H3.3 K27me3, H3.3 K27M and H3.3 G43R staining are shown (images at magnification 20x).

After establishing the preclinical pHGG models, our main purpose was to compare the methods of paraffin tissue analysis, liquid biopsy (CSF) and mouse weight monitoring to assess tumor burden in mice with orthotopic pHGG xenografts. These goals are addressed in the next sections of this chapter.

2. Limits of detection of *H3F3A* and *ACVR1* DNA sequences and analysis of pHGG models.

We developed a ddPCR method to quantify copies of the genes *H3F3A* and *ACVR1* in cell-tumor DNA (ctDNA) and genomic DNA derived from pHGG cell models. Using gDNA from DIPG-007 cells, we established that the limit of detection of the ddPCR assays for *H3F3A (*K27M and WT*)* and *ACVR1 (*R206H and WT) sequences were 32.6 and 81.5 pg of DNA per reaction, respectively. Using gDNA from GBM-002 cells, we found that the LOD of the ddPCR assay for *H3F3A* G34R was 40.8 pg of DNA. Inter-assay R^2 coefficients were above 0.97

for the assays of *H3F3A* (K27M and *G34R*-mutant and WT) and *ACVR1* (*R206H*-mutant and WT) (**Figure 22A**). All the slopes were different from zero ($P < 0.0001$). We did not detect false positives in any of the analyzed blank samples. All pHGG models in culture released ctDNA to the supernatant, corresponding to 29.8% (6.4% – 58.4%) of the gDNA (median and range of six cell models). At a density of 1 x 10^6 cells/mL in culture medium, we detected *H3F3A* and *ACVR1* WT alleles in the ctDNA and gDNA of all cells (**Figure 22B**).

For *H3F3A* K27M mutant models, the mutant-to-WT allele ratio was in the range 1-3 (**Figure 22B**). DIPG-007 and DIPG-011 exhibited a mutant-to-WT allele ratio of 2 and 3, respectively, suggesting that a subset of tumor cells exhibited heterozygous mutation of the oncogene, as a result of the copy number alterations associated with the mutant allele, known as mutant allele specific imbalance (MASI)[179,180]. The *H3F3A* K27M mutant allele was not present in GBM-001 and GBM-002 cell lines (**Figure 22B**). We detected the *H3F3A* G34R and the *ACVR1* R206H alleles exclusively in the cells bearing these mutations (**Figure 22C, D**). The proportion of *ACVR1* R206H in DIPG-007 was below 1, as expected, because this is a subclonal heterozygous mutation[181].

In a first experiment in four mice bearing intracranial DIPG-007 tumors at endpoint, we detected *H3F3A* K27M and *ACVR1* copies in all brain formalin-fixed paraffin-embedded (FFPE) sections (**Figure 22E, F**). CSF samples were slightly positive for *H3F3A* K27M and *ACVR1* copies in three and two samples, respectively (**Figure 22E, F**). All plasma samples were negative for both sequences (**Figure 22E, F**). In GBM-002 tumors at endpoint, we detected human *H3F3A* G34R sequences in 100% (4/4) of tumor-bearing brains (**Figure 22G**). We did not detect human sequences in brain, CSF and plasma obtained from non-tumor mice (**Figure 22E, F, G**). Overall, data suggested that the specificity of the ddPCR techniques was appropriate, with no positives in the control samples. However, the sensitivity was not sufficient to detect DNA copies in part of the CSF samples and all plasma samples.

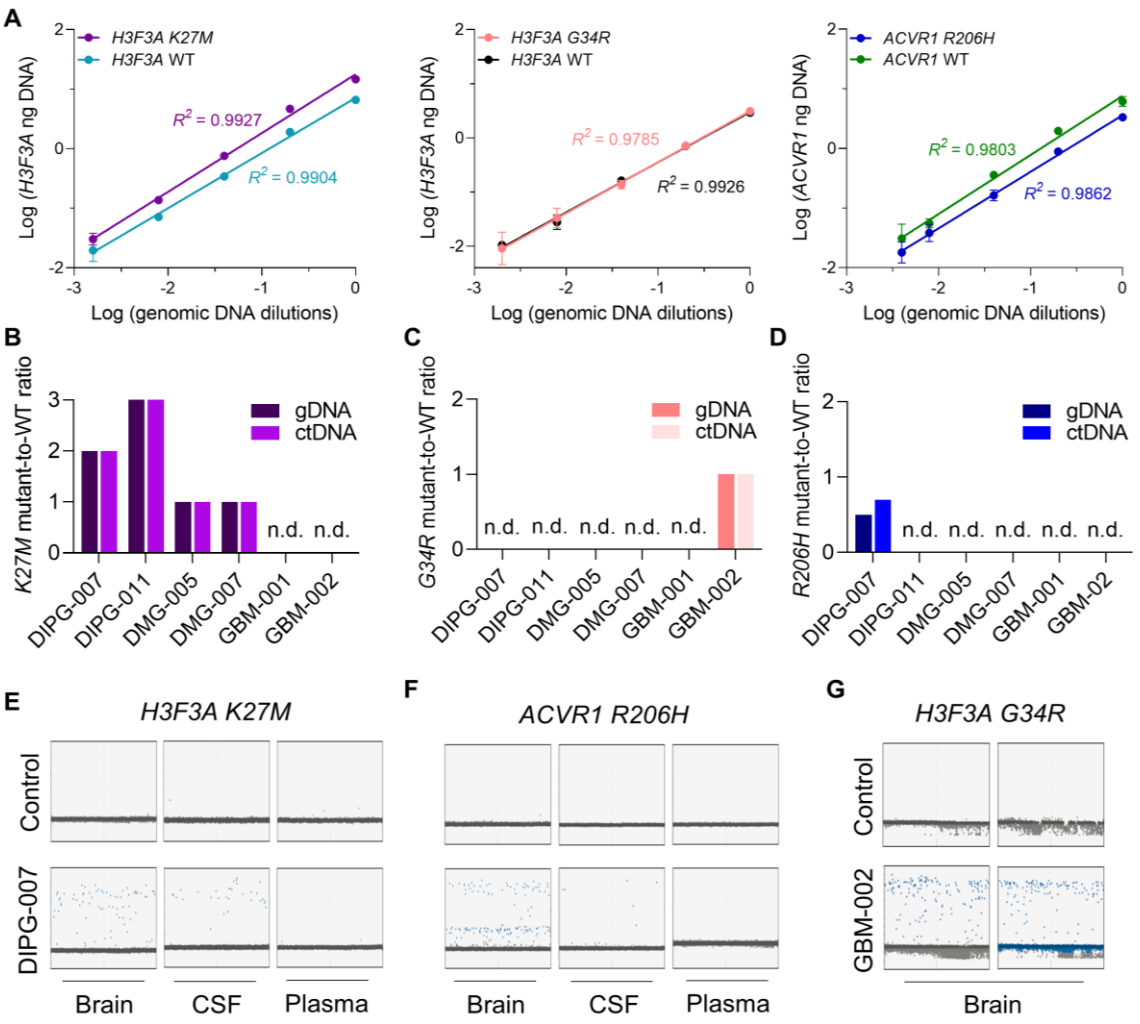

Figure 22. Linearity of the ddPCR techniques and quantification of wild type (WT) and mutant alleles of *H3F3A* and *ACVR1* genes in pHGG. (A) Amount (ng) of DNA of *H3F3A* K27M and WT alleles (DIPG-007 cells), *H3F3A* G34R and WT alleles (GBM-002), and *ACVR1* R206H and WT alleles (DIPG-007) in serial dilutions of genomic DNA. Genomic DNA input was 20.4 ng in dilution 1. Dots and error bars are inter-assay means and SD of the three independent calibration experiments. Lines are regression curves following a simple linear regression model. (B) Proportion of *H3F3A* K27M and WT alleles in pHGG models. (C) Proportion of *H3F3A* G34R and WT alleles in pHGG models. (D) Proportion of *ACVR1* R206H and WT alleles in pHGG models. (E) Representative plots of *H3F3A* K27M ddPCR droplets in brain, CSF, and plasma obtained from one control mouse without tumor (Control) and one tumor-bearing mouse (DIPG-007) at endpoint. (F) Representative plots of *ACVR1* R206H ddPCR droplets in brain, CSF, and plasma obtained from one control mouse without tumor (Control) and one tumor-bearing mouse (DIPG-007) at endpoint. (G) Representative plots of *H3F3A* G34R ddPCR droplets in brain obtained from two control mouse without tumor (Control) and two tumor-bearing mouse (GBM-002) at endpoint. N.d.: not detectable.

3. Development of ddPCR assays with pre-amplification PCR.

To improve the sensitivity of the assays in the limited volume of 5 µL of CSF collected from the mouse cisterna magna, we developed a pre-amplification PCR for *H3F3A*. Pre-amplification with up to 15 cycles enabled the detection of *H3F3A* in the CSF of DIPG-007-bearing mice, while there was no amplification in control non-tumor samples (**Figure 23A, B**). Pre-amplified plasma from DIPG mice at endpoint remained negative for ddPCR analyses (**Figure 23B**). From these results, we concluded that 12 cycles of pre-amplification PCR provided an optimal number of positive droplets for *H3F3A*, avoiding saturation of the reaction. The ddPCR technique for pre-amplified gDNA (DIPG-007), at an initial input of 2.3 ng and further diluted until 0.001 pg, was linear, with inter-assay R^2 coefficients above 0.92 for K27M-mutant and WT *H3F3A* alleles (**Figure 23C**). Slopes for all sequences were different from zero ($P < 0.0001$). Preamplification increased the sensitivity of the technique by 200 times, achieving a limit of detection (LOD) for *H3F3A* of 0.145 pg of DNA per ddPCR reaction. Without preamplification, loading 2-10 ng of ctDNA (the maximum volume feasible) allowed the detection of 0.10 ng of human *H3F3A* in mouse CSF (equivalent to a concentration of 1.68 copies/µL). After 12 cycles of preamplification, loading 4 ng of ctDNA resulted in a detection of 13.42 ng (equivalent to 213 copies/µL).

For DIPG-007 cells in culture, we compared the amount of *H3F3A* detected in the supernatant following a preamplification PCR step or without it, using 20 ng ctDNA from supernatants. Only when using the preamplification step, the amount of *H3F3A* detected in the supernatant increased steadily during a period of seven days and correlated with the count of viable cells (**Figure 23D**). These results demonstrated the relevance to preamplify the ctDNA before the ddPCR analysis.

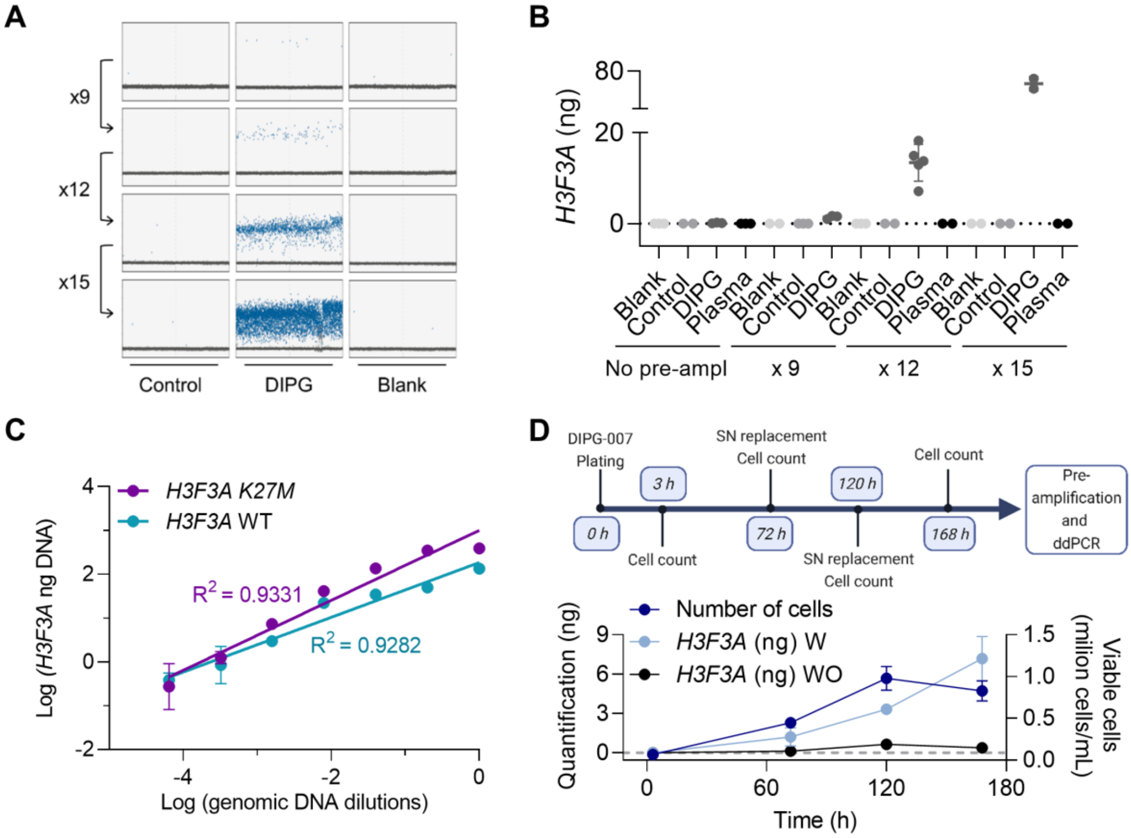

Figure 23. Optimization of the preamplification PCR for CSF samples. (A) Representative plots of *H3F3A* K27M droplets generated by ddPCR of CSF samples subjected to no preamplification (top panels) or preamplification of 9, 12 and 15 cycles of PCR, obtained from four DIPG-007-bearing mice at endpoint (DIPG) and four non-tumor (Control) mice. Additional negative controls (Blank) are sterile water. (B) ddPCR quantification of *H3F3A* DNA (ng) obtained with 0-15 amplification cycles of CSF and plasma from 10 DIPG-007 xenografts at endpoint and seven non-tumor (Control) mice. Additional negative controls (Blank) are sterile water. Each dot of the groups DIPG and Control in the graph is data from one mouse. (C) Amounts (ng) of DNA of *H3F3A* K27M and WT alleles in serial dilutions of preamplified gDNA of DIPG-007. Preamplified DNA input was 2.26 ng in dilution 1. Dots are inter-assay means and SD of the three independent calibration experiments. Lines are regression curves following a simple linear regression model. (D) Quantification of *H3F3A* in DIPG-007 cell culture supernatant (SN) during one week. At each time, we counted viable cells, preamplified the ctDNA, and quantified *H3F3A* (ng) with (W) or without (WO) preamplification. The diagram represents the workflow of the study. Dots are mean and errors of two replicates.

4. *H3F3A* ddPCR of pre-amplified CSF samples to evaluate DIPG progression in mice.

First, we evaluated the progression of the diffuse infiltrative DIPG-007 in the brain of 30 nude mice by immunohistochemistry, sacrificing 4-5 mice at each time point (**Figure 24**). Cancer cells inoculated in the fourth ventricle invaded the surrounding parenchyma between days 15 and 30 after inoculation (**Figure 25A**). Tumor burden increased progressively until endpoint, in which cells invaded extensively areas of the brainstem, cerebellum, midbrain and thalamus (**Figure 24, Figure 25A**).

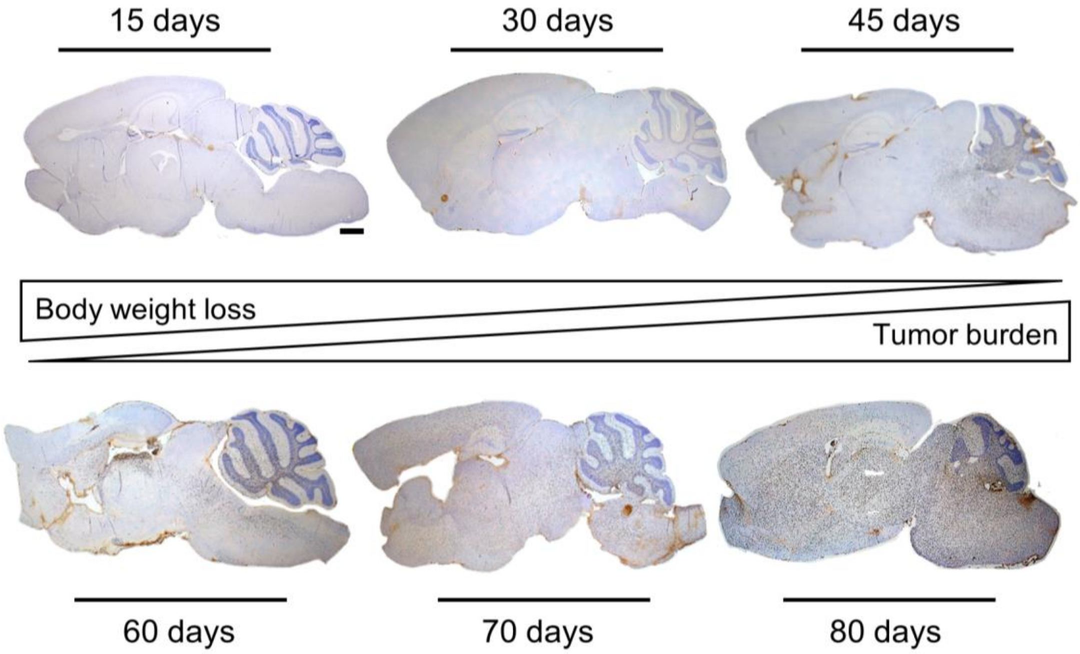

Figure 24. Panoramic vision of tumor progression in mice bearing HSJD-DIPG-007 cells at different time points. Immunochemistry for anti-human nuclear antigen (brown dots in the pictures) of a representative tumors at 15, 30, 45, 60, 70 and 80 days after cell inoculation of the hole brain (x1.25 magnification, scale bar = 1.6 mm).

Body weight loss with mild neurological symptoms (ataxia) appeared between days 45 and 60 (**Figure 25B**). At the end of the study (day 80), the remaining mice achieved endpoint (>20% weight loss). No mouse experienced severe neurological symptoms.

To address the correlation of *H3F3A* (detected by ddPCR) and disease progression, we quantified the amount of *H3F3A* gDNA and human cells in FFPE sections of the mouse brains. We found that *H3F3A* counts increased steadily from the first sampling point at day 15 until the last at day 80 (**Figure 25C**). The count of human nuclear-positive cells infiltrating the brainstem increased steadily from the second sampling point at day 30, until day 80 (**Figure 25C**). In the CSF samples, *H3F3A* ctDNA was detectable from day 15, remained at the same level until day 60, and increased from there until endpoint (**Figure 25C**).

There was a significant correlation between the count of human nuclear-positive cells in the tissue slide and the amount of *H3F3A* gDNA detected using ddPCR (**Figure 25D**). In contrast, the amount of *H3F3A* ctDNA extracted from CSF samples did not correlate neither with the number of infiltrating human cancer cells nor with the amount of human *H3F3A* gDNA in FFPE slides (**Figure 25E**). At the time of sacrifice, weight loss (main sign of disease progression in the DIPG-007 xenograft) of the 30 animals correlated well with the number of human nuclear-positive cells infiltrating the brain, with the amount of *H3F3A* gDNA extracted from FFPE slides, and with the amount of *H3F3A* ctDNA extracted from CSF samples (**Figure 25F**).

Overall, these results demonstrate that the ddPCR technique applied to the analysis of ctDNA in the liquid biopsy (CSF) detects progressive disease only after animals start symptoms (weight loss), which occurs around day 60 after tumor inoculation in DIPG-007-bearing mice. In contrast, both the ddPCR technique applied to the analysis of tumor gDNA and the count of human nuclei-positive cells are more accurate methods to measure the degree of the disease progression, independently of the disease symptoms.

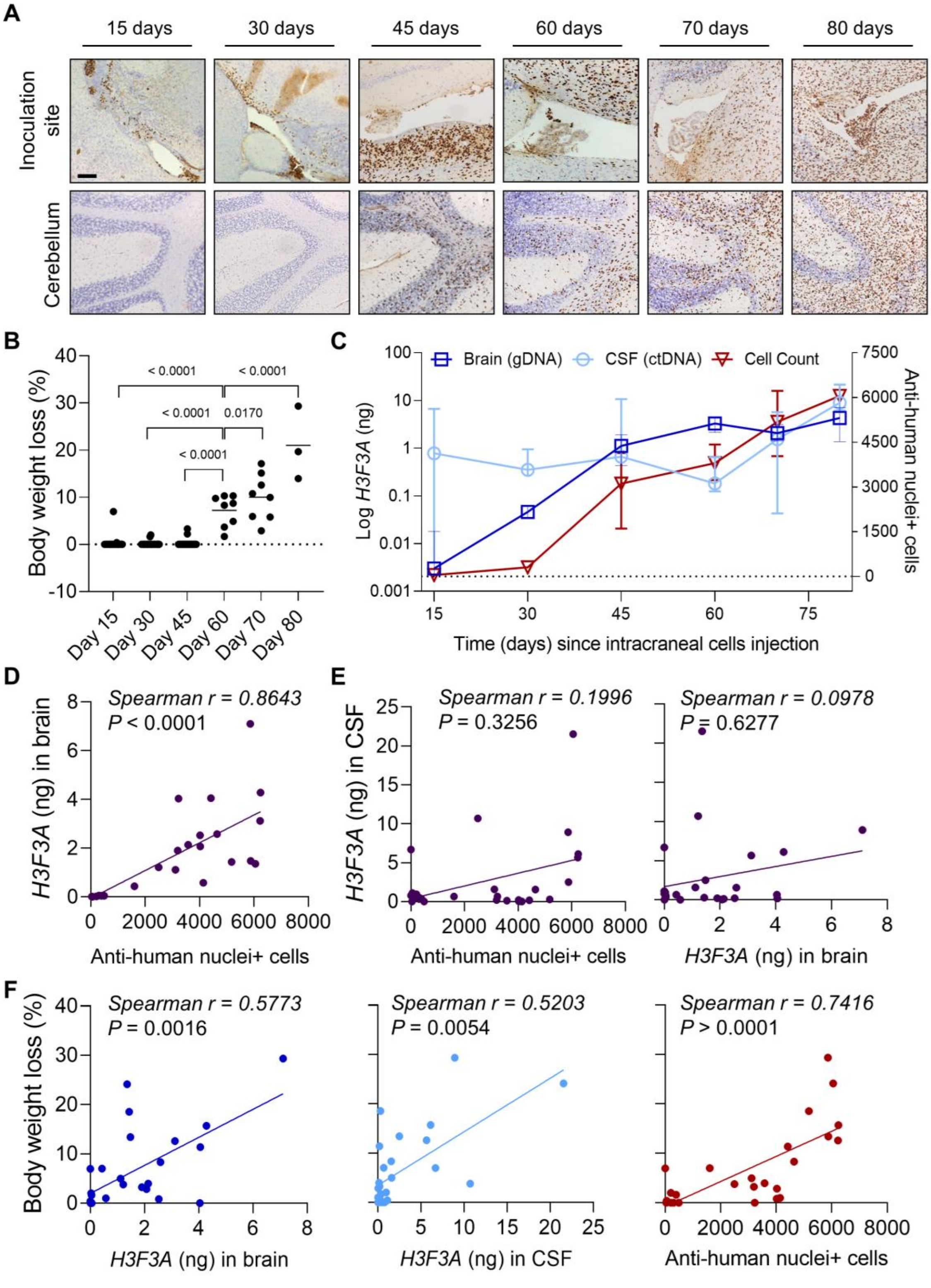

Figure 25. Analysis of DIPG-007 xenograft progression through human cell infiltration, body weight loss and *H3F3A* DNA (ng) in brain parenchyma and CSF samples. (A) Immunostaining of human cells (anti-human nuclear antigen, in brown) at the inoculation site (fourth ventricle) and at a main infiltration site (cerebellum) at time points 15-80 days after cell inoculation. Photos are from representative cases. Scale bar = 100 µm. (B) Scatter plot of mouse weight loss along time after the inoculation of DIPG-007 cells. Each dot represents data from one mouse and lines are

means. (C) Amount-time curves of (i) *H3F3A* gDNA (ng) in mouse brain FFPE slides, (ii) *H3F3A* ctDNA (ng) in pre-amplified CSF and (iii) human cell count in mouse brain FFPE slides. Data connected by lines are the median and the interquartile range of 3-5 samples. (D) Correlation between *H3F3A* gDNA (ng) and the human cell count in mouse brain FFPE slides. Dots are paired data from individual animals. The Spearman correlation coefficient, r, and the P value are displayed in the graph. (E) Correlation between *H3F3A* ctDNA (ng) in pre-amplified CSF and either (i) the human cell count in mouse brain FFPE slides, or (ii) *H3F3A* gDNA (ng) in mouse brain FFPE slides. Dots are paired data from individual animals. (F) Correlation between weight loss at the time of tissue sampling and (i) the human cell count in mouse brain FFPE slides, (ii) *H3F3A* gDNA (ng) in mouse brain FFPE slides, or (iii) *H3F3A* ctDNA (ng) in pre-amplified CSF.

5. Serial liquid biopsy of CSF in mice.

Time points for serial CSF collection in five animals ranged from 15 to 80 days and are represented in **Figure 26A**. All animals survived the procedures, with no neurological symptoms after puncturing the cisterna magna. *H3F3A* ctDNA counts increased in the CSF after day 60 (**Figure 26B**). All animals lost weight from day 60 (**Figure 26C**). At the endpoint, cancer cells invaded the brain parenchyma profusely, with no cells in the ventricular system (**Figure 26D**).

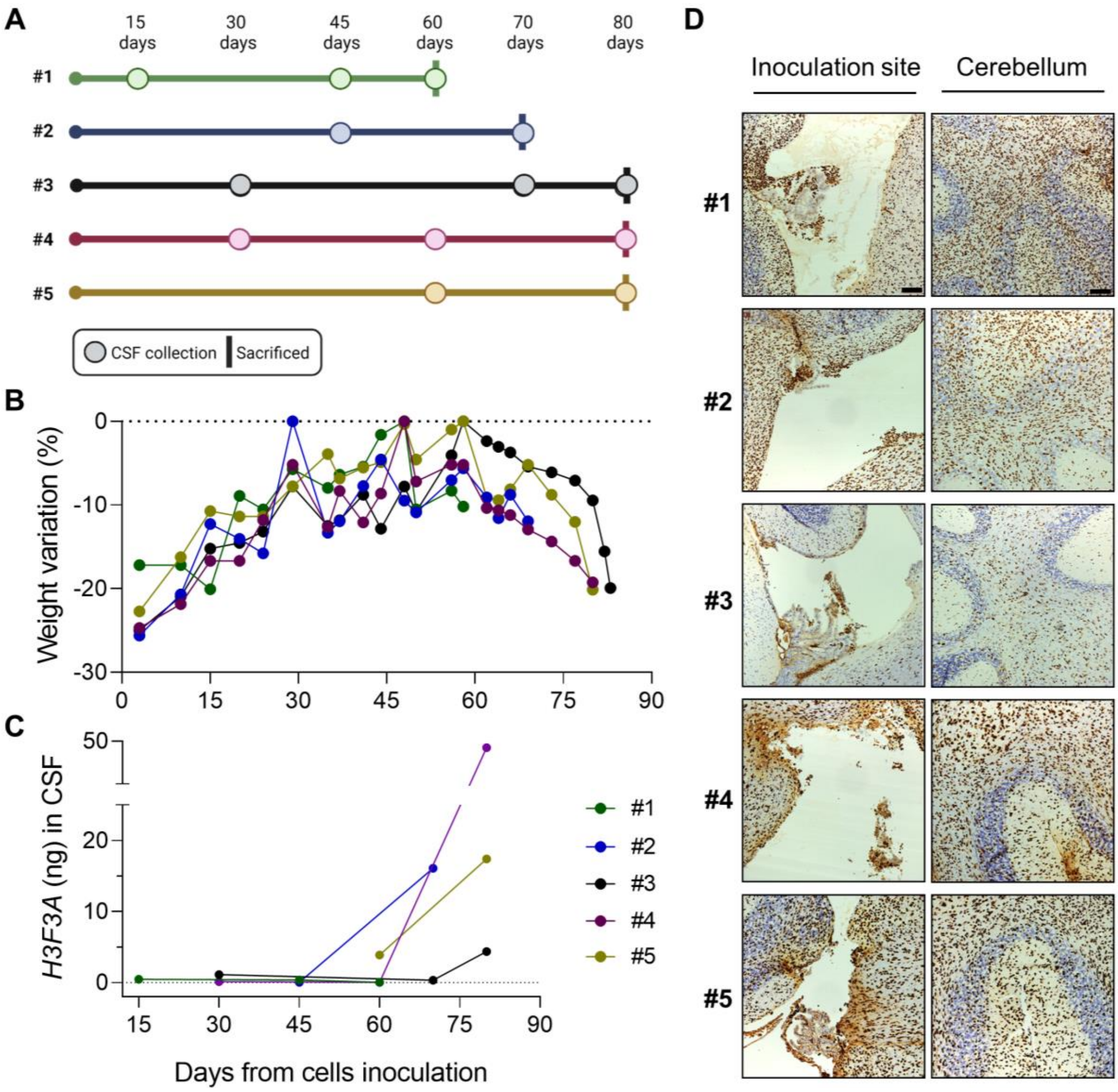

Figure 26. Serial sampling and analysis of the CSF of DIPG-007 xenografts. (A) Diagram of the CSF sampling times (days) of the five animals included in the study. (B) Changes (%) of the individual mouse body weight, relative to the individual maximum weight (100%). (C) *H3F3A* ctDNA ddPCR analysis of pre-amplified CSF samples. Results from individual animals are connected with lines. (D) Immunostaining of human cells (anti-human nuclear antigen) in the inoculation site (fourth ventricle) and in a main infiltration site (cerebellum) at the time of mouse sacrifice. Scale bar = 100 µm.

6. Selected examples of the application of the developed pHGG models in preclinical studies of drug activity.

During my PhD studies, we used the developed pHGG models to perform important *in vivo* studies to evaluate treatment activity. Briefly, we injected DIPG-007 cells in the fourth ventricle of athymic nude or NOD-SCID mice, and started treatments, usually at the maximum tolerable doses, around one month later. We followed up mouse weight to assess treatment toxicity and/or disease symptoms, and euthanized all mice upon reaching 20% weight loss, defined as endpoint. Statistical analyses were conducted using GraphPad Prism 9 software.

I will present examples for treatments using *ACVR1* inhibitors, trametinib, ONC201 and taselisib. For all the selected animal studies, we followed up disease using the body weight follow-up method, which we demonstrate correlative to the tumor burden using ddPCR analysis and/or staining of human cells infiltrating the brain.

6.1. New *ACVR1* inhibitors: M4K2009 and M4K2163

As mentioned in the introduction section, about 20% of DIPG bear mutations in *ACVR1* (ALK2), an activator of the TGFβ pathway, and thus is a potential target for therapeutic intervention. *Smil et al.* adopted an open science approach to develop a series of potent, selective, orally bioavailable, and brain-penetrant ALK2 inhibitors based on the lead compound LDN-214117[170]. In the frame of a collaboration agreement with M4K, I evaluated two small molecule inhibitors of ALK2, M4K2009 and M4K2163 that target the intracellular kinase activity of the ALK2 protein[170,171].

First, I evaluated the activity of M4K2009. To evaluate the cytotoxic activity *in vitro*, I plated 500 cells/well and measured cell viability 6 days after starting drug exposure at concentrations ranging of 0.039 to 10 µM. The assay revealed antiproliferative activity of the treatment, with a calculated IC_{50} of 0.81 µM (**Figure 27A**). A human brain endothelial cell line (hCMEC/D3) was not sensitive to the drug (**Figure 27A**).

These *in vitro* results, together with the favorable CNS distribution profile of M4K2009[170], encouraged us to assess drug activity *in vivo*. First, we evaluated M4K2009 in 48 mice, divided in four groups. The survival of treated groups was 88-90 days, not significantly different compared to the control group (82 days) (**Figure 27B**). By monitoring the body weight loss during the study, we evaluated the tumor growth and drug toxicity. We detected toxicity in all groups treated with the drug, with more pronounced effects in the groups at 100 mg/kg dosage (up to 10% body weight loss) (**Figure 27C**). Animals treated with the vehicle were administered one week later, at which point we began to observe weight loss, likely due to the inherent toxicity of the vehicle itself. By the end of the treatment, the animals did not regain weight, which could indicate the high toxicity of the vehicle used for drug administration (**Figure 27C**).

At the endpoint, all animals had fill infiltration of cancer cells in their brains (**Figure 27D**). This finding confirms that exceeding a 20% body weight loss in mice is a reliable indicator of significant tumor progression.

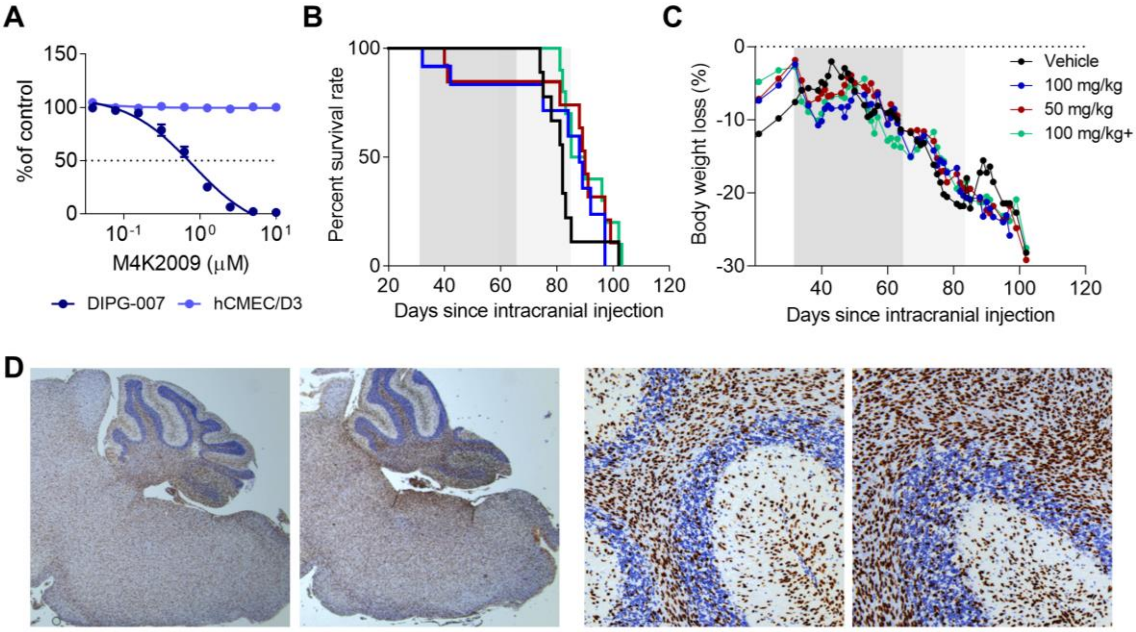

Figure 27. Preclinical results activity of M4K2009 in DIPG-007 model. (A) *In vitro* cytotoxicity of M4K2009 against DIPG-007 and hCMEC/D3 cells. Dots represent the mean and SD of 6 replicates. (B) Kaplan Meier curves showing M4K2009 activity in DIPG-007 bearing mice compare to controls. (C) Body weight variation of mice treated with M4K2009 compared to controls. (D) Immunochemistry for anti-human nuclear antigen tumors at the endpoint of the study (x1.25 and x10 Magnification).

We evaluated a second anti-*ACVR1* candidate M4K2163, that demonstrated a similar IC$_{50}$ in DIPG-007 cells *in vitro* (0.60 µM) after 6 day treatment (**Figure 28A**).

After completion of the treatments, 10-12 animals of each group were left untreated until endpoint, followed by body weight monitoring. The survival of treated groups (groups 2 and 3, median survival 94 days) was not significantly different compared to the control group (group 1, median survival 92 days). Animals belonging to group 4, treated with 100 mg/kg M4K2163 during 8 weeks, demonstrated an increase in survival compared to animals treated with vehicle (92 versus 121 days, p = 0.0142) (**Figure 28B**). The vehicle administered was toxic, resulting in weight loss in the animals during treatment, regardless of the treatment group (**Figure 28C**).

Again, at the endpoint, immunohistochemical staining with anti-human nuclear antigen revealed high tumor cellularity in all brains (**Figure 28D**).

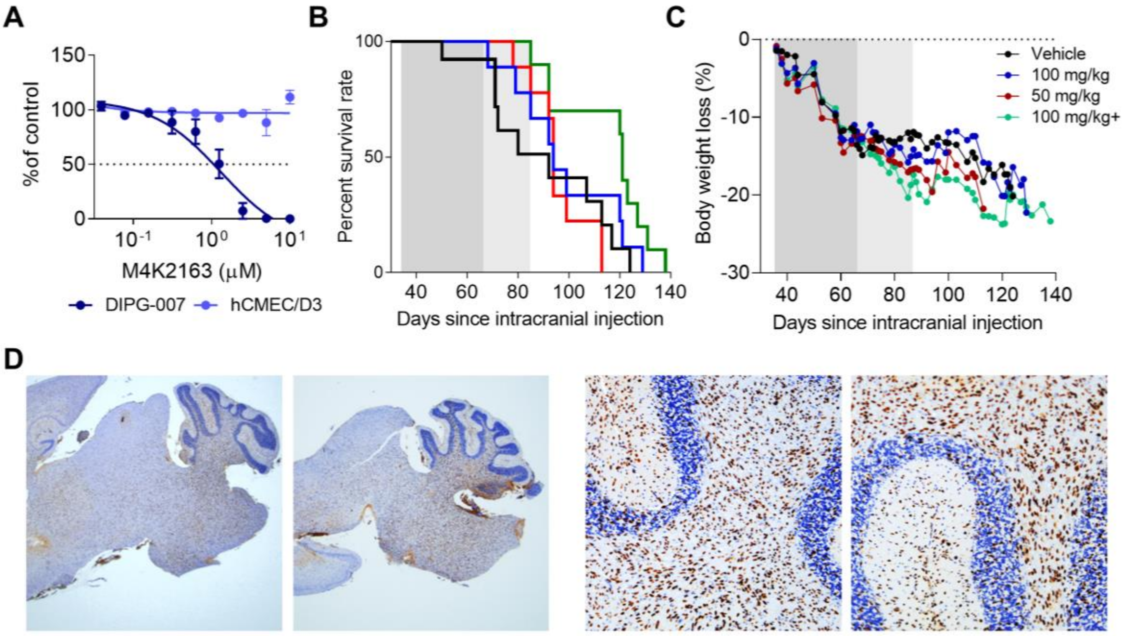

Figure 28. Preclinical results activity of M4K2163 in DIPG-007 model. (A) *In vitro* cytotoxicity of M4K2163 against DIPG-007 and hCMEC/D3 cells. Dots represent the mean and SD of 6 replicates. (B) Kaplan Meier curves showing M4K2163 activity in DIPG-007 bearing mice compare to controls. (C) Body weight variation of mice treated with M4K2163 compared to controls. (D) Immunochemistry for anti-human nuclear antigen tumors at the endpoint of the study (x1.25 and x10 Magnification).

6.2. Trametinib

Alterations in the MAPK pathway are commonly found in childhood cancers, particularly brain tumors, and especially low- and high-grade gliomas, including non-brainstem pHGG, with described alterations in *FGFR1*, *NF1*, *BRAF*^{V600E}, *NTRK2*^{ITD} and *MET*, and DIPG, with described alterations in *PIK3R1* and *NF1*. These alterations represent an unexplored option in a tumor type desperately needing novel treatment strategies. Trametinib is a highly specific and potent MEK1/2 inhibitor that binds to the allosteric pocket of MEK. Specifically, these alterations involve multiple nodes of the MAPK signalling pathway and include *PIK3R1*^{N564D}, *NF1*^{I1824S}, and *BRAF*^{G469V}. These results suggest a possible rationale for the use of trametinib in DIPG, as investigated in the phase II clinical trial TRAM-01 (NCT03363217), which explored the use of trametinib in pediatric gliomas harboring MAPK alterations/activation[160]. Subsequently, various clinical trials are emerging that combine trametinib with other inhibitors, such as everolimus, for the treatment of low and high-grade gliomas (NCT04485559).

Considering this rationale and the previous *in vitro* results obtained in our group, we analysed the efficacy of trametinib in DIPG-007 tumor-bearing mice. We evaluated trametinib in 26 mice, divided in two groups. The median survival of the treated group (117 days) was not significantly different compared to the control group (120 days) (**Figure 29A**). Thus, trametinib did not have activity in this xenograft model. By monitoring body weight loss throughout the study, we observed a slight reduction in animal weight in both groups, likely indicative of the toxicity associated with the vehicle used for drug administration (**Figure 29B**). At the endpoint, we assessed tumor cellularity in the murine brains via immunohistochemical staining with an anti-human nuclear antigen. Consistent with the evolution of the body weight loss, a high number of tumor cells were detected across all groups (**Figure 29C**).

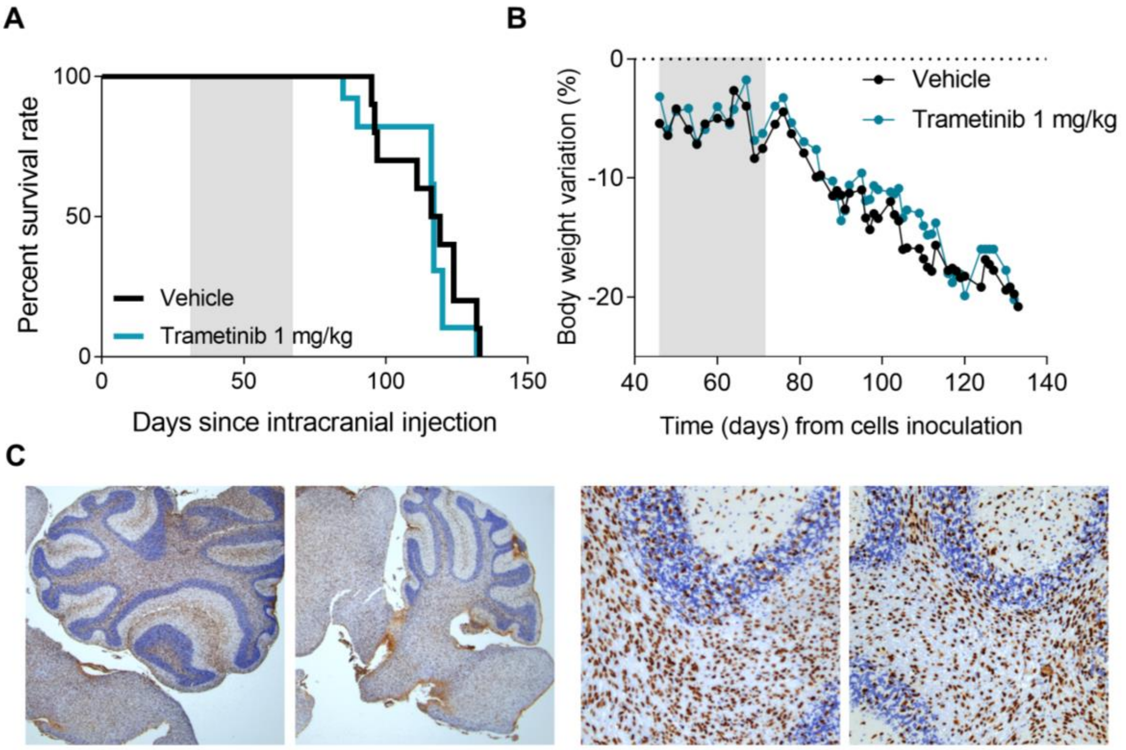

Figure 29. Preclinical results activity of trametinib in DIPG-007 model. (A) Kaplan Meier curves showing trametinib activity in DIPG-007 bearing mice compare to controls. (B) Body weight variation of mice treated with trametinib compared to controls. (C) Immunochemistry for anti-human nuclear antigen tumors at the endpoint of the study (x1.25 and x10 Magnification).

6.3. ONC201

ONC201, a small molecule compound exhibiting potential anti-neoplastic activity, has been investigated in clinical trials involving pediatric and young adult patients diagnosed with H3 K27M-mutant DIPG. These studies have demonstrated that ONC201 is well-tolerated in this patient population (NCT03416530). Thus, we analysed the efficacy of ONC201 in DIPG-007 tumor-bearing mice.

We evaluated ONC201 in 10 mice, divided in two groups. The median survival of the treated group (70 days) was not significantly different compared to the control group (76 days) (**Figure 30A**). By monitoring body weight loss throughout the study, we observed a slight reduction in animal weight in both groups, likely indicative of the high toxicity associated with the vehicle used for drug administration, although it was more pronounced in the ONC201 treated group, indicating the drug toxicity (**Figure 30B**). At the endpoint, we assessed tumor cellularity in the murine brains via immunohistochemical staining with an anti-human nuclear antigen. Consistent with the appearance of body weight loss, a high number of tumor cells were detected across all groups (**Figure 30C**).

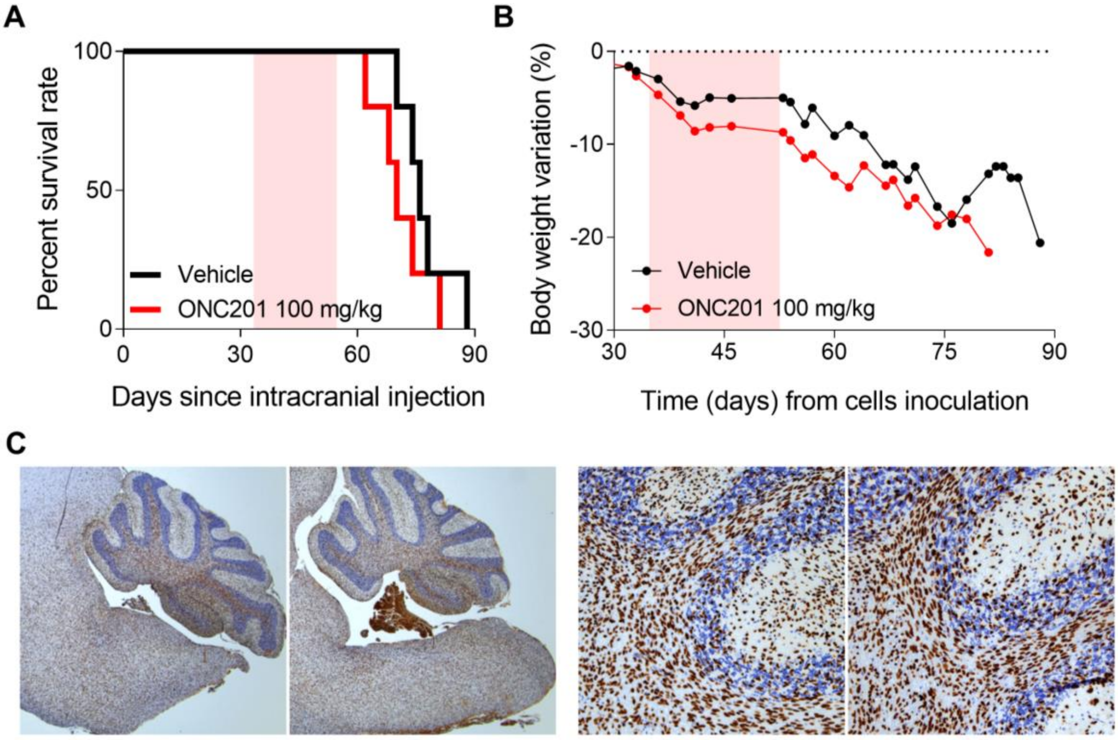

Figure 30. Preclinical results activity of ONC201 in DIPG-007 model. (A) Kaplan Meier curves showing ONC201 activity in DIPG-007 bearing mice compare to controls. (B) Body weight variation of mice treated with ONC201 compared to controls. (C) Immunochemistry for anti-human nuclear antigen tumors at the endpoint of the study (x1.25 and x10 Magnification).

In this study, we did not obtain the expected results. We chose the intraperitoneal route for administration, as previous preclinical studies had shown positive outcomes using this route[119], although none of them used DIPG-007 xenografts. In the clinical practice, this drug is administered orally and appears to be yielding promising results in clinical trials with patients diagnosed with DIPG[182]. We do not believe the administration route caused the lack of activity, which probably was more related to the inherent aggressive behavior of the DIPG-007 xenograft.

6.4. Taselisib

Taselisib, as a potent PI3K inhibitor that specifically targets the β isoform, demonstrates enhanced efficacy against tumors with mutations in the PI3K pathway[183]. This prompted me to assess its anti-tumor effects in DIPG-007 tumor-bearing mice, known to harbor the PI3K mutation H1047R.

For *in vitro* studies, we plated 3000 cells/well and we measured the cell viability 72 h after the drug was placed in contact with the cells at concentrations ranging 10^{-6} to 100 µM. We performed the assay with DIPG-007, DIPG-014, DIPG-021 and DMG-005 cell models. We observed promising efficacy of the compound against models with the PI3K mutation DIPG-007, achieving an IC_{50} of 0.01 µM. DIPG-014 also displayed sensitivity to taselisib, though to a lesser extent, whereas DIPG-021 and DMG-005 exhibited pronounced resistance to the drug (**Figure 31A**). The brain endothelial cell line hCMEC/D3 was affected by taselisib only at concentrations higher than 1 µM (**Figure 31A**). These *in vitro* results supported the subsequent *in vivo* experiments.

In a study in 30 mice, we observed a survival benefit of 12 days in the treated animals, being median survivals 83 and 94.5 days for the control and treatment groups, respectively ($p = 0.0337$) (**Figure 31B**). The drug was poorly tolerated by the mice, as evidenced by an initial weight loss of approximately 10% from their maximum weight at the beginning of treatment (**Figure 31C**). All animals died of tumors (**Figure 31D**).

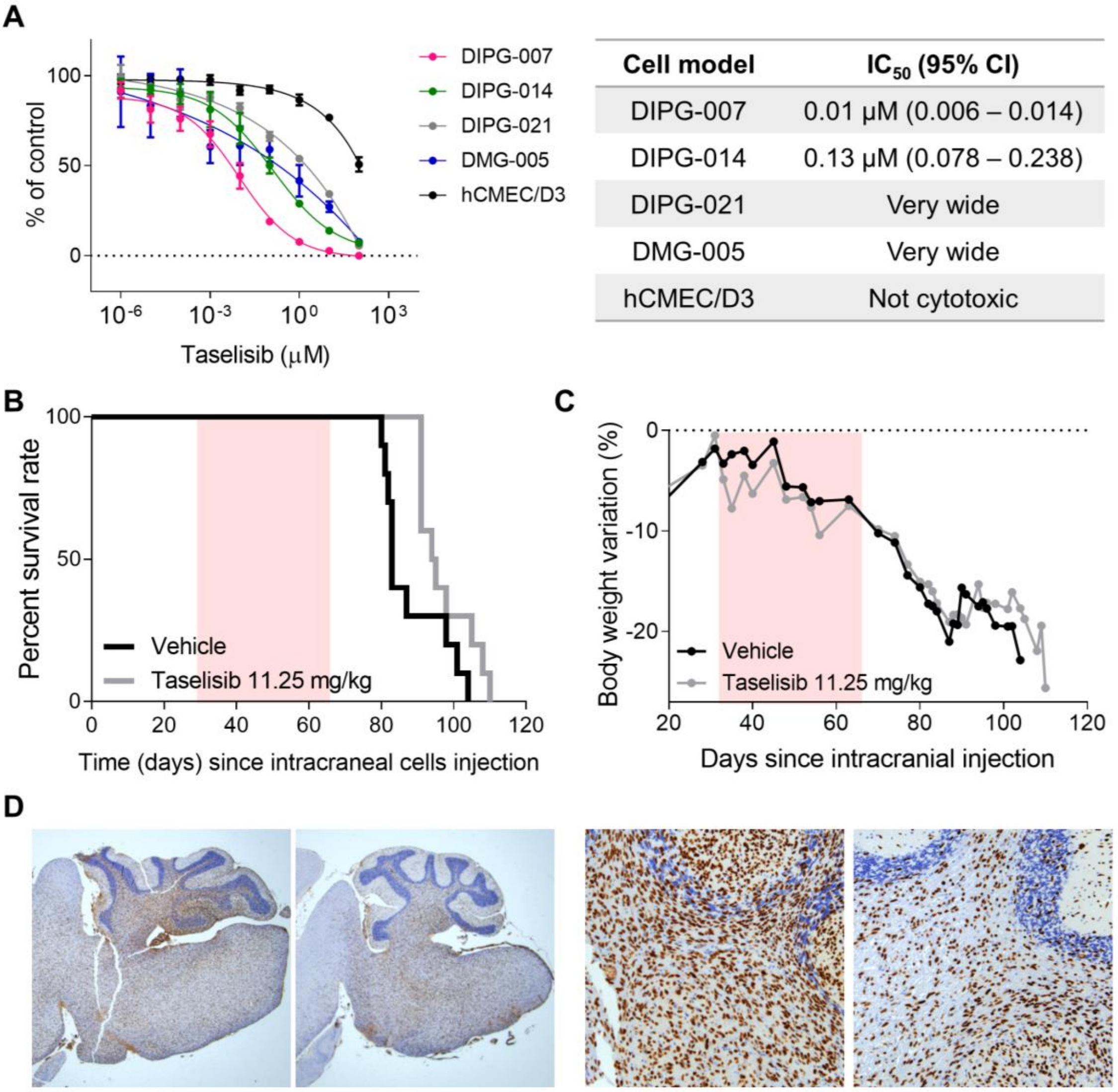

Cell model	IC_{50} (95% CI)
DIPG-007	0.01 µM (0.006 – 0.014)
DIPG-014	0.13 µM (0.078 – 0.238)
DIPG-021	Very wide
DMG-005	Very wide
hCMEC/D3	Not cytotoxic

Figure 31. Preclinical results activity of taselisib in DIPG-007 model. (A) *In vitro* cytotoxicity of taselisib against DIPG-007 and hCMEC/D3 cells. Dots represent the mean and SD of 6 replicates. (B) Kaplan Meier curves showing taselisib activity in DIPG-007 bearing mice compare to controls. (C) Body weight variation of mice treated with taselisib compared to controls. (D) Immunochemistry for anti-human nuclear antigen tumors at the endpoint of the study (x1.25 and x10 Magnification).

Despite promising results, we did not pursue further investigation with this drug against DIPG, due to reported toxicity in clinical trials for various cancers of adult patients[184].

Chapter 5. Results II

Characterization the PI3K/Akt/mTOR pathway in preclinical pHGG models and in patients with DIPG.

1. Dysregulation of PI3K/Akt pathway in pHGG/DIPG cell models.

Because alterations in the RTK-PI3K-MAPK pathway are shared by more than 60% patients with pHGG[10], we aimed to find them in 12 preclinical pHGG models established and available in our laboratory. Following the analysis of the whole exome sequencing data, we found abnormalities in genes associated with the RTK-PI3K pathway among all pHGG lines (**Figure 32**).

Among the genes encoding for the receptors of the pathway, we identified amplifications of epidermal growth factor receptor (*EGFR*) in six cases (50%), insulin-like growth factor 1 receptor (*IGF1R*) in five cases (42%), and platelet-derived growth factor receptor alpha (*PDGFRA*) in one case (8%). Of note, *PDGFRA* was mutated in the two models derived from hemispheric tumors.

One or more subunits of PI3K were altered in 10 models, with notable alterations in the p110α catalytic subunit *PIK3CA* (in which we allocate the *PIK3CA*-mutant model DIPG-007), the p110β catalytic subunit *PIK3C2B*, and the regulatory subunit *PIK3R1*, which was uniquely gained in GBM-002.

The PI3K activity inhibitor *PTEN* presented a nonsense mutation in one line, GBM-002 (**Figure 32**).

We included in the analysis alterations of the MAPK/ERK pathway, because MEK signalling is frequently co-activated as a resistance mechanism when the PI3K pathway is inhibited with medicines[163,185], providing the rationale for double therapies against MAPK/ERK and PI3K/Akt[162,186]. In our panel, we found *BRAF* amplified in 12% samples and gained in 42%, *MAP2K1* (encoding MEK) gained in 25%, and *MAPK3* (encoding ERK) gained in 12 %, with one line, DMG-005, having alterations in the three mentioned genes (**Figure 32**).

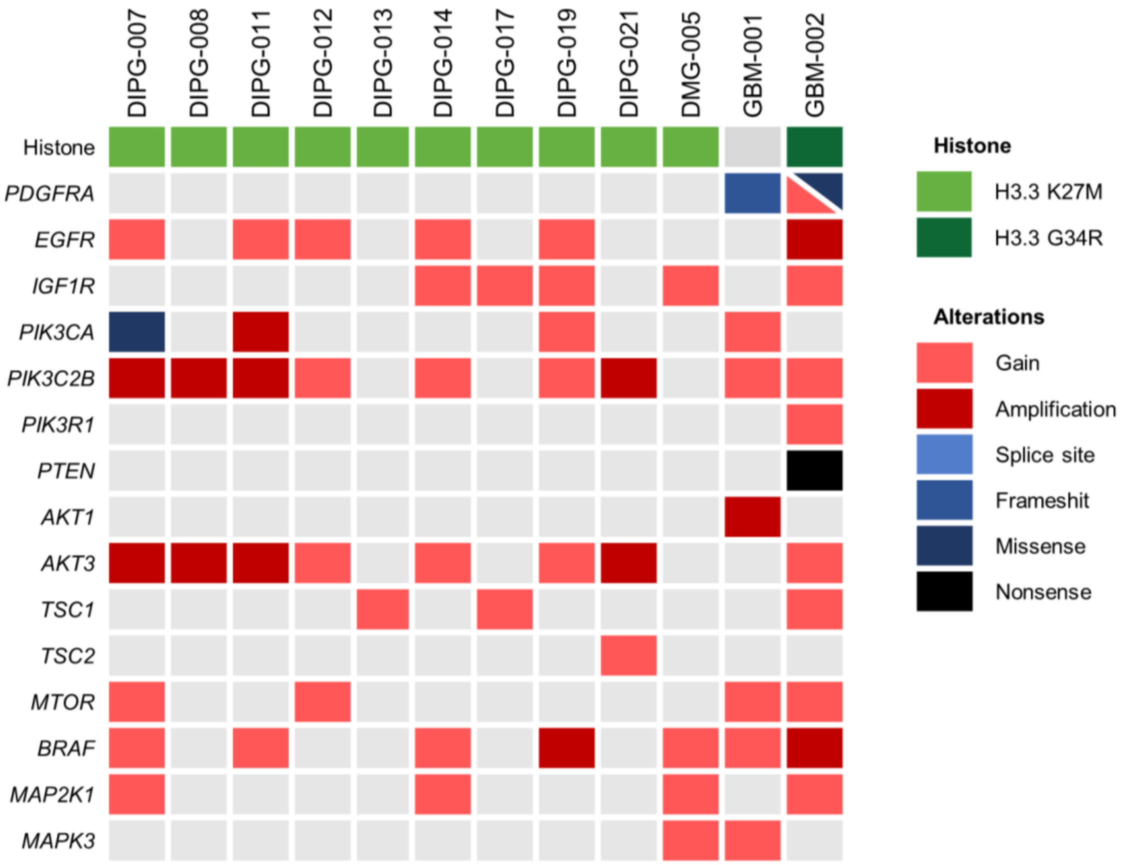

Figure 32. Whole-exome sequencing of the PI3K/Akt and MAPK/ERK pathway-related genes on 12 lines of pHGG. The Oncoprint visualizes the single-nucleotide variants and DNA copy-number alterations found in patient-derived models of pHGG (n = 12). In the representation, samples are displayed in columns, and genes in rows. Clinicopathological and molecular annotations are illustrated with bars as indicated in the accompanying key.

To investigate the effect of the detected DNA alterations in the expression of genes related to PI3K/Akt pathway, we analyzed RNA and protein expression in the pHGG models.

At the RTK level, we detected increased expression of *EGFR* in most (8 of 12) pHGG models, in contrast to insulin-like growth factor 1 receptor *IGF1R* (1 overexpressed of 12) or *KIT* (0 of 12) (**Figure 33A**). Of note, two lines (DIPG-008 and DIPG-021), without increased expression of *EGFR* had *PDGFRA* overexpressed instead (**Figure 33A, B**). Two lines, DIPG-017 and GBM-002, showed overexpression of both *EGFR* and *PDGFRA* (**Figure 33A, B**). Additionally, *KRAS* overexpression in four pHGG highlights its frequent hyperactivation in DIPG, which could be driven by mechanisms such as recurrent growth factor activation, mutations in RTKs, and the genetic inactivation of RAS-regulatory proteins like NF1[10,187] (**Figure 33A**).

Regarding PI3K-related genes, regulatory subunit isoforms *PIK3R1*, *PIK3R2*, and *PIK3R4* showed higher expression levels, compared to catalytic subunit isoforms such as *PIK3CB* or *PIK3CD* (**Figure 33A**).

Concerning the tumor suppressor *PTEN*, which negatively regulates the PI3K/Akt signalling pathway[188], it was found overexpressed in 50% of the samples, coinciding with observed downregulation of genes associated with the PI3K/Akt pathway (**Figure 33A**).

There was low basal expression of the *AKT1* isoform across all pHGG (**Figure 33A**). This finding was anticipated, because different AKT isoforms exhibit preferential tissue expression patterns, with *AKT3* being particularly abundant in brain tissue[189], as corroborated in our results (**Figure 33B**). Additionally, *RPS6KB1*, direct target of AKT, exhibited elevated expression levels in those samples bearing increased expression of *PIK3* subunits and lack of *PTEN* expression, such as DIPG-007, DIPG-011, DIPG-014, and DIPG-017 (**Figure 33 A**).

Regarding the RAS/RAF/MEK/Erk pathway, which represents a primary compensatory mechanism for the PI3K/Akt pathway, we exclusively observed an upregulation of *RAF1* in DIPG-007 cells. Additionally, in DIPG-011, DIPG-017, and DMG-005, only *MAPK14* and *MAPK8*, both belonging to the MEK pathway kinases, showed elevated expression levels. In the former two models, this observation may suggest the relevance of the MEK pathway alongside the PI3K pathway. In the case of DMG-005, it appears that the MEK pathway may play a more pivotal role in its survival and proliferation, compared to the PI3K pathway, potentially due to overexpressed PTEN inhibiting the PI3K/Akt pathway (**Figure 33A**).

Subsequently, we examined the activation of the PI3K/Akt signalling pathway using Western blot (**Figure 33C**). We found that some cells, such as DIPG-008 and GBM-001, were more dependent on PDGFRα, compared to EGFR or IGF-1Rβ, as previously suggested by the RNA analysis. We observed phosphorylation of Akt at Ser473 in all the cultures (**Figure 33C**). The lowest levels of Akt activation belonged to DIPG-019 and DIPG-021, likely due to the low activity of PDGFRα, which is a primary RTK activator of PI3K/Akt pathway in pHGG (**Figure 33C**). PRAS40 protein, a direct effector of Akt, showed high expression in those cells with the highest levels of activated pAkt. Similarly phosphorylated S6 kinase was expressed by all the cultures, being DIPG-007 and DMG-005 the ones with highest expression (**Figure 33C**).

With regard to the MAPK pathway, ERK1/2 was substantially phosphorylated in DIPG-013, DIPG-017 and DIPG-021. At least in the last model, Erk phosphorylation may indicate the strong dependency on the MAPK pathway signalling (**Figure 33C**).

The distinct activation levels of pAkt found in the immunoblotting analysis were further demonstrated in DIPG-017 (high activation) and DIPG-021 (low activation) via immunofluorescence, revealing elevated and diminished protein activation (i.e., Akt phosphorylation), respectively (**Figure 33D**).

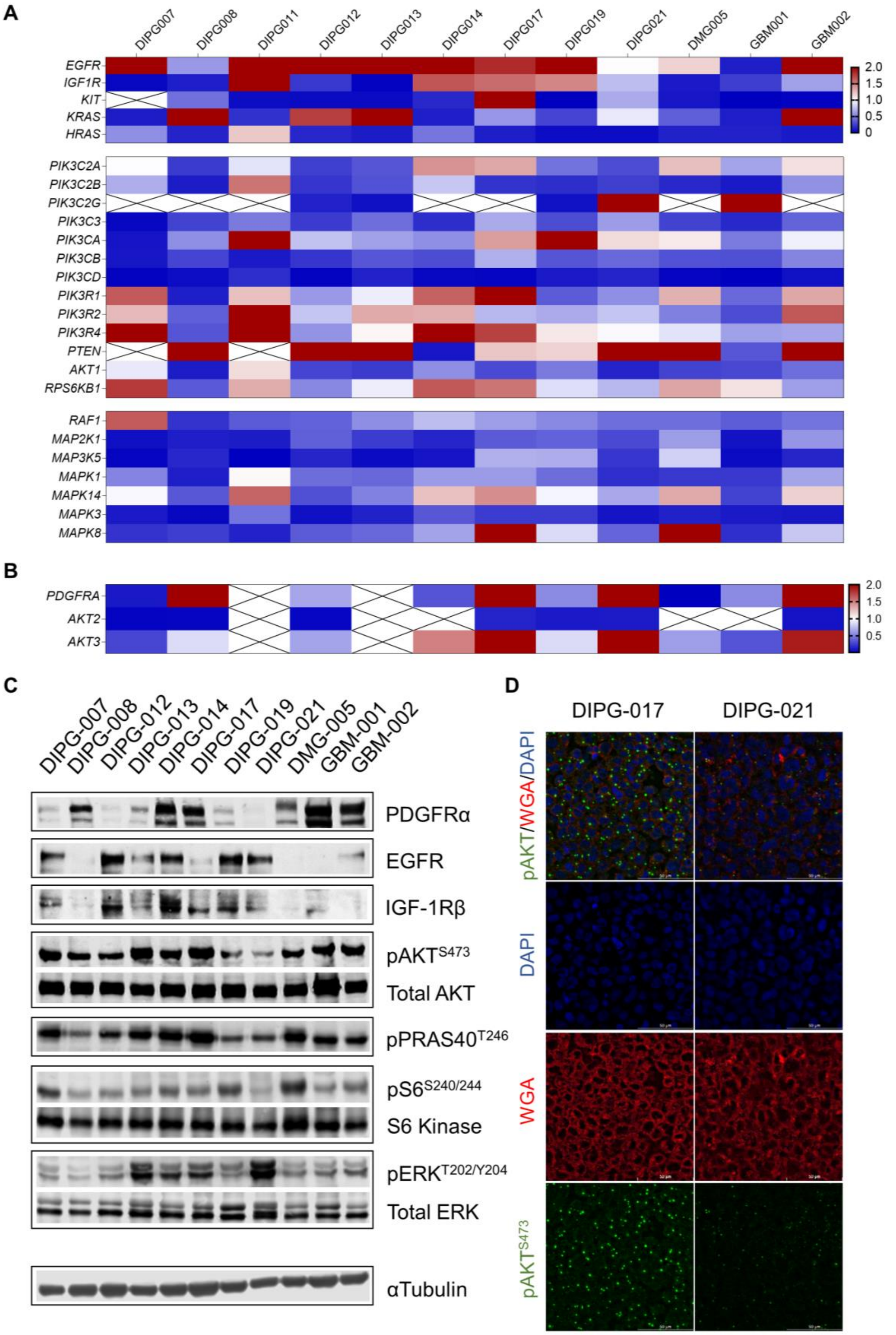

Figure 33. Analysis of the RTK-PI3K-MAPK axis in pHGG cell models. (A) RNA expression of genes related to RTK, PI3K/Akt and MEK/Erk pathway, normalized to RNA from a healthy brain (commercial RNA), included in the TaqMan™ Array Human PI3K Signaling. X indicates no

amplification of the gene. (B) RNA expression levels of PDGFRA, AKT2 and AKT3 genes not included in the array, related to GAPDH housekeeping, and normalized to RNA from a healthy brain. X indicates no amplification of the gene. (C) Expression of proteins involved in the RTK, PI3K/Akt and MEK/Erk nodes in 11 pHGG models in culture. (D) Immunofluorescence of phospho-Akt (green) in DIPG-017 (high expression) and DIPG-021 (low expression), staining the cytoplasmic membrane with WGA (red) and the nucleus with DAPI (blue). Scale bar = 50 µm.

2. Imbalance in the PI3K/Akt pathway in DIPG patients.

To verify the clinical relevance of our previous analyses, we performed similar studies in samples derived from necropsies and biopsies of patients with pHGG.

First, we obtained five samples from autopsies, all frozen, and assessed the expression of eight genes associated with the PI3K/Akt pathway: *EGFR*, *PDGFRA*, *FGFR1*, *PIK3CA*, *PIK3R1*, *AKT1*, *AKT2*, and *AKT3*. All tumors exhibited significantly elevated *PDGFRA* expression compared to healthy brain tissue. *EGFR* was overexpressed in three cases, and *FGFR1* was overexpressed in one. *PIK3CA* and *PIK3R1* were consistently overexpressed across most cases. One or more of the *AKT* subunits were also overexpressed in all but one of these tumors, with *AKT3* showing the highest level of expression, similar to our results for pHGG models (**Figure 34A**).

At the protein level, we assessed pathway activation by immunoblotting in two specific phosphorylation sites, namely serine-473 of Akt (pAkt) and threonine-246 of PRAS40 (pPRAS40), the readout of Akt activity. We detected pathway activation in three out of five necropsies (60%), a proportion consistent with the published data[10] (**Figure 34B**). Two samples exhibited pronounced Akt and PRAS40 activation, while in a third sample the activation was restricted to Akt (**Figure 34B**).

We also identified the activation of the PI3K/Akt pathway in paraffin samples obtained from recent patient biopsies performed at HSJD. These samples had routine pathological anatomy immunostaining analyses available for H3K27M and H3K27me3, being all positive for the mutant protein, and negative for the trimethylation of K27 (**Figure 34C**). Immunostaining for serine-240/244 of S6 kinase (pS6) was the chosen indicator for PI3K/Akt pathway activation, because it is a downstream effector of the mTORC1 pathway, which is influenced by the

PI3K/Akt signalling cascade[190]. The analysis was performed by our colleagues at the Laboratory of Molecular Oncology, led by Dr. Cinzia Lavarino. An expert pathologist revealed active pathway signalling in five biopsies (71%), with tumor cell positivity of pS6 ranging between 80% and 40% (**Figure 34C**).

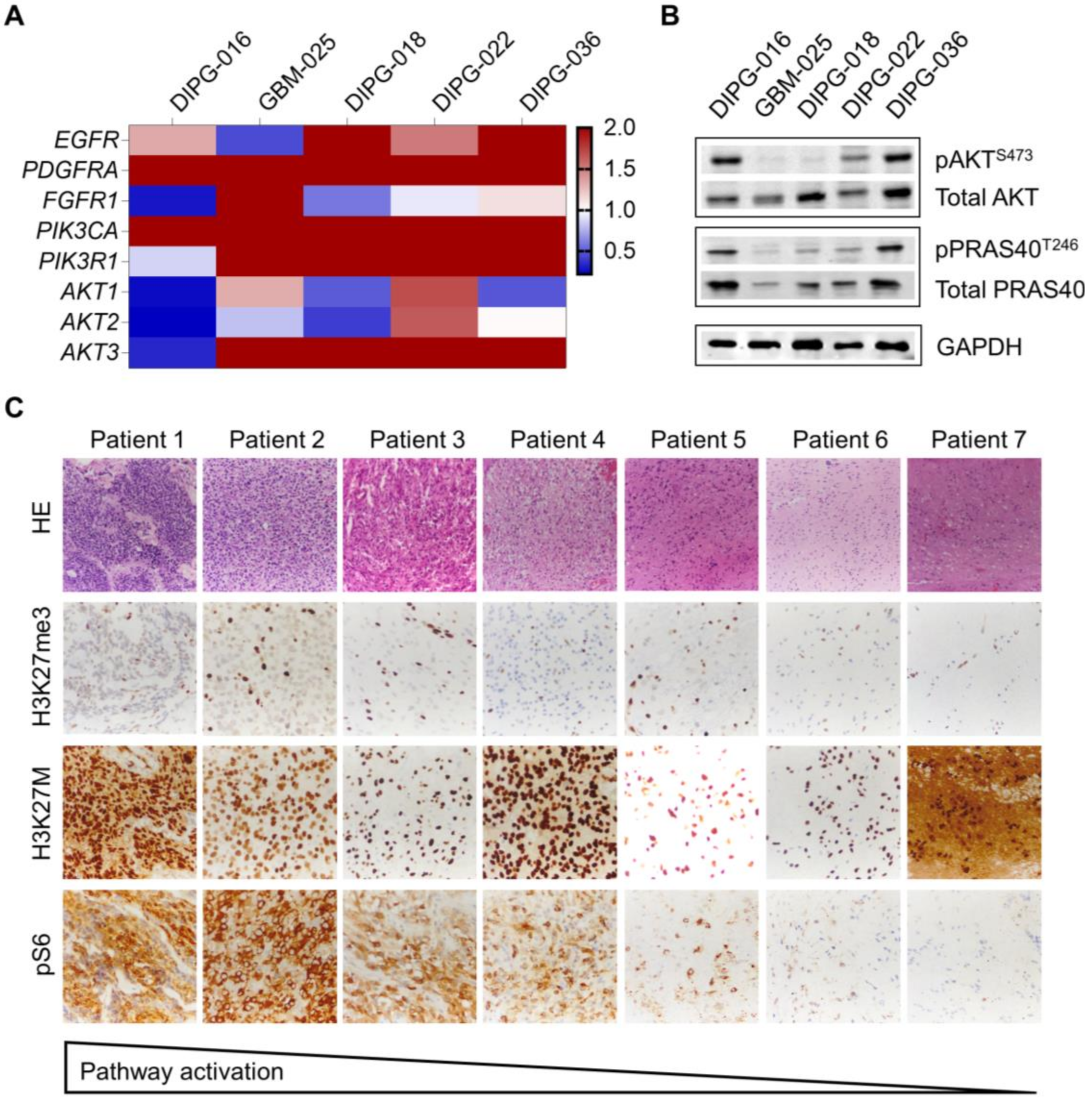

Figure 34. PI3K/Akt signalling in DIPG. (A) Expression of selected genes related to the PI3K/Akt pathway in pHGG autopsy samples, normalized to the mean of one RNA obtained from a healthy brain (commercial sample) and one RNA from the necropsy of a healthy pediatric brain. (B) Western blot analysis of proteins related to the PI3K/Akt signaling pathway in the same autopsy samples used for RNA analysis. (C) Immunohistochemistry analysis of H3K27me3, H3K27M and phospho-S6 kinase in DIPG biopsy samples (x40 Magnification).

Chapter 6. Results III

Targeting the PI3K/Akt/mTOR pathway in DIPG.

1. Anticancer and antiangiogenic activity of the PI3K/Akt inhibitors.

We studied and compared the anticancer activity of one PI3K inhibitor, inavolisib (GDC0077) and one AKT inhibitor, ipatasertib (GDC0068), as single therapeutic agents, in DMG models, most of them obtained from tumors in the brainstem (DIPG).

First, we observed that ipatasertib and inavolisib inhibited the proliferation of all the DIPG models included in the activity panel (**Figure 35A**). The IC_{50} values were in the range 0.01-10 µM range for both inhibitors, being the mean IC_{50} 0.6 µM for inavolisib and 4.2 µM for (**Table 8**). In agreement with the mechanism of action of inavolisib as PI3K inhibitor, we found that the *PIK3CA* H1047R-mutant DIPG-007 was the most sensitive to inavolisib (IC_{50} = 0.01 µM), and also to ipatasertib (IC_{50} = 1 µM), compared to all the other *PIK3CA* wild-type models (**Table 8**). To assess the therapeutic window of the treatments, we also treated the human brain endothelial cell line hCMEC/D3, which showed a marked lack of sensitivity to both drugs, compared to DIPG cells (**Figure 35A**) (**Table 8**). Overall, these data suggested that inavolisib and ipatasertib could become promising therapeutic approaches for DIPG, especially when PI3K is mutated, and provided they have favorable biopharmaceutic and pharmacokinetic properties, which we will address later in this PhD work.

To investigate the impact of PI3K/AKT on the clonogenic capacity of DIPG cells, we measured the number of colonies formed after treatment. Compared to the control, ipatasertib treatment did not affect colony formation significantly (**Figure 35B**) (**Table 9**). In contrast, inavolisib treatment, even at low concentrations of 0.1 µM, showed a potent effect on reducing colony formation (**Figure 35B**) (**Table 9**).

To investigate whether these drugs could inhibit the formation of the vasculature in DIPG, we designed an angiogenesis study in hCMEC/D3 cells treated with each inhibitor. We quantified the total length (mm) and the number of newly formed vascular junctions in cells treated at concentrations of inavolisib and ipatasertib of 1 and 10 µM, respectively, which are sub-cytotoxic for hCMEC/D3 cells. From the work of my laboratory mate Mercè Baulenas, we know that the supernatant of DIPG cells favors the formation of complex vascular structures by hCMEC/D3 cells (**Figure 35C**). Thus, we used this supernatant to stimulate vessel formation and to assess the antiangiogenic function of the evaluated agents. We found that the endothelial cells cultured in non-enriched media formed few and short vascular structures, compared to abundant, long and more complex structures when they were exposed to the proangiogenic DIPG supernatant (**Figure 35C**). Under similar proangiogenic conditions, such complex structures were almost completely inhibited by inavolisib at 1 µM, and partially inhibited by ipatasertib at 10 µM (**Figure 35C**). We confirmed the results by staining CD31 (endothelial marker) in hCMEC/D3 cells (**Figure 35C**).

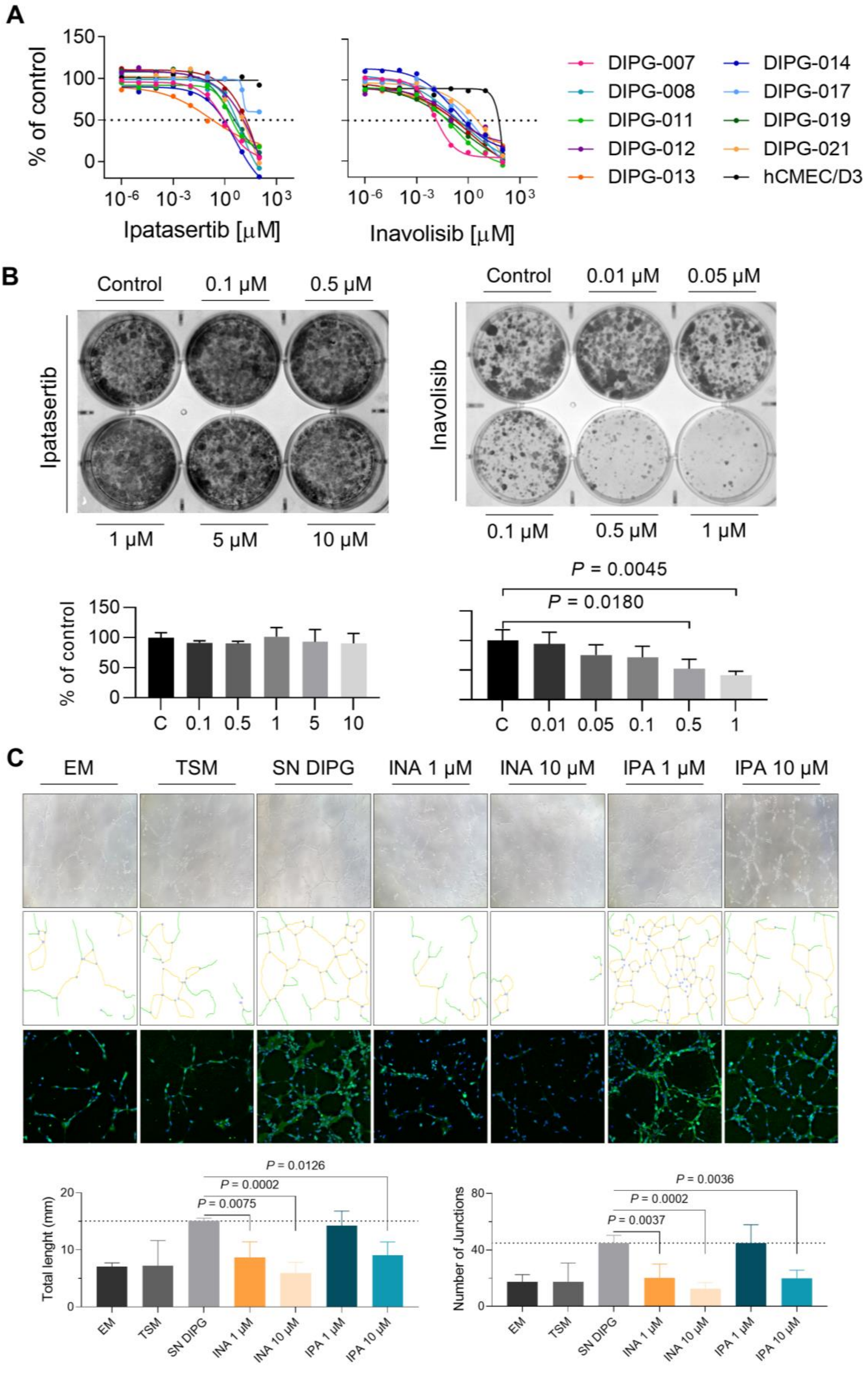

Figure 35. *In vitro* anticancer and antiangiogenic activity of PI3K/Akt pathway inhibitors inavolisib and ipatasertib. (A) Antiproliferative activity in 9 DIPG models and the brain endothelial cell line

hCMEC/D3. Dots are the mean of 3-6 replicates and curves were built using Graphpad Prism 9. (C) Colony formation assay of ipatasertib and inavolisib in DIPG-007 cells, after 48 h treatment. Graphics represent the percentage of colonies, with reference to the control condition. (D) Angiogenesis inhibition assay with ipatasertib (IPA) and inavolisib (INA) using hCMEC/D3 cells, after 24 h treatment. Images obtained directly from the hCMEC/D3 culture and the immunofluorescence of CD31 (x20 Magnification). Graphics represent the mean ± SD of the total length (mm) and the number of junctions formed between endothelial cells. Data were compared to the positive control condition in the presence of DIPG-007 supernatant (SN).

Table 8. Cytotoxic activity of ipatasertib and inavolisib in preclinical models of DIPG and hCMEC/D3 cell line. The concentrations of the drug required to cause a reduction of 50% in cell proliferation, IC50, were calculated using Graphpad Prism version 9.

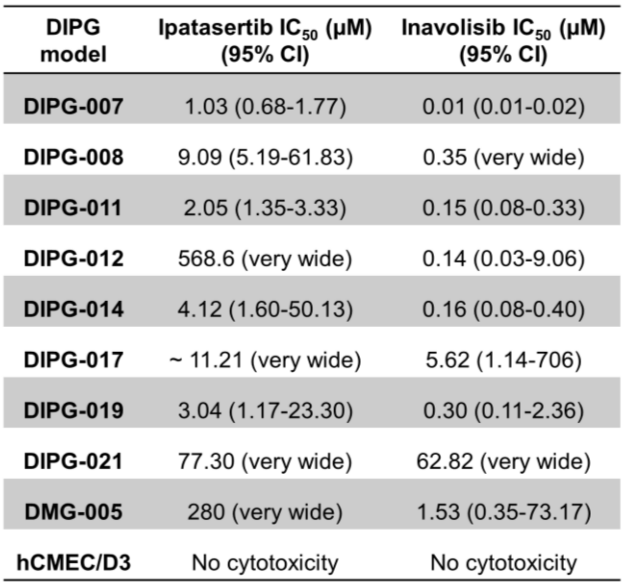

DIPG model	Ipatasertib IC_{50} (µM) (95% CI)	Inavolisib IC_{50} (µM) (95% CI)
DIPG-007	1.03 (0.68-1.77)	0.01 (0.01-0.02)
DIPG-008	9.09 (5.19-61.83)	0.35 (very wide)
DIPG-011	2.05 (1.35-3.33)	0.15 (0.08-0.33)
DIPG-012	568.6 (very wide)	0.14 (0.03-9.06)
DIPG-014	4.12 (1.60-50.13)	0.16 (0.08-0.40)
DIPG-017	~ 11.21 (very wide)	5.62 (1.14-706)
DIPG-019	3.04 (1.17-23.30)	0.30 (0.11-2.36)
DIPG-021	77.30 (very wide)	62.82 (very wide)
DMG-005	280 (very wide)	1.53 (0.35-73.17)
hCMEC/D3	No cytotoxicity	No cytotoxicity

Table 9. Colony formation assay after 48 h of treatment with ipatasertib or inavolisib in DIPG-007 cells. The values represent the percentage of colony quantification ± standard deviation, compared to the untreated controls.

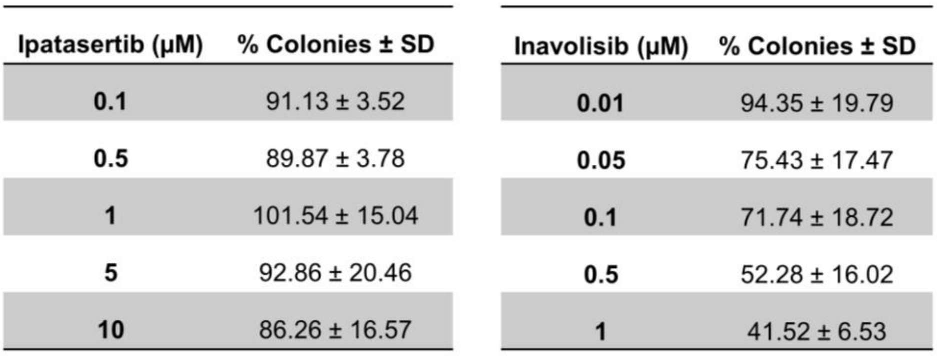

Ipatasertib (µM)	% Colonies ± SD
0.1	91.13 ± 3.52
0.5	89.87 ± 3.78
1	101.54 ± 15.04
5	92.86 ± 20.46
10	86.26 ± 16.57

Inavolisib (µM)	% Colonies ± SD
0.01	94.35 ± 19.79
0.05	75.43 ± 17.47
0.1	71.74 ± 18.72
0.5	52.28 ± 16.02
1	41.52 ± 6.53

2. Inhibition of the PI3K/Akt pathway and induction of apoptosis with inavolisib.

We addressed the inhibition of the downstream PI3K/Akt cascades using the most potent of the assayed drugs, inavolisib. We evaluated the phosphorylation of surrogate proteins of the PI3K/Akt pathway by an immunoblotting assay. Phosphorylation of Akt at S473 (pAkt) was used as readout for Akt activity, and phosphorylation of PRAS40 (pPRAS40) and S6 (pS6) ribosomal protein were used as surrogate readouts for mTOR activity. We selected for the assay the models DIPG-007 (*PIK3CA*-mutant), DIPG-014 and DIPG-021, all of them with constitutive phosphorylation of PRAS40 and S6 ribosomal protein in basal condition. Inavolisib potently inhibited the Akt/mTOR pathway in a dose-dependent manner in DIPG-007 and DIPG-014, with DIPG-007 cells being particularly sensitive the drug, even at 0.04 µM (**Figure 36A**). In contrast, DIPG-021 cells were resistant to inavolisib at concentrations below 1 µM (**Figure 36A**). We attributed these results to the *PIK3CA* mutational state which is likely a biomarker for inavolisib response in DIPG. As described in Chapter 5 of this thesis, the DIPG-021 model exhibits high basal levels of Erk phosphorylation, coupled with low Akt activation. This suggest a strong reliance on MAPK pathway signalling in this cell model, rather than on the PI3K pathway, rendering it less sensitive to inavolisib.

Next, we assessed whether inavolisib induced cell apoptosis. Caspase-3/7 were cleaved after inavolisib treatment, particularly after times of incubation of at least 48 h, and at concentrations of at least 1 µM (**Figure 36B**). The poly (ADP-ribose) polymerase protein (PARP), a useful hallmark of cell death, was also cleaved following inavolisib treatment (**Figure 36B**). We confirmed the immunoblotting results on cleaved PARP using flow cytometry. Inavolisib treatment for 24 h increased the apoptosis rate of DIPG-007 cells in a dose-dependent manner (**Figure 36C**).

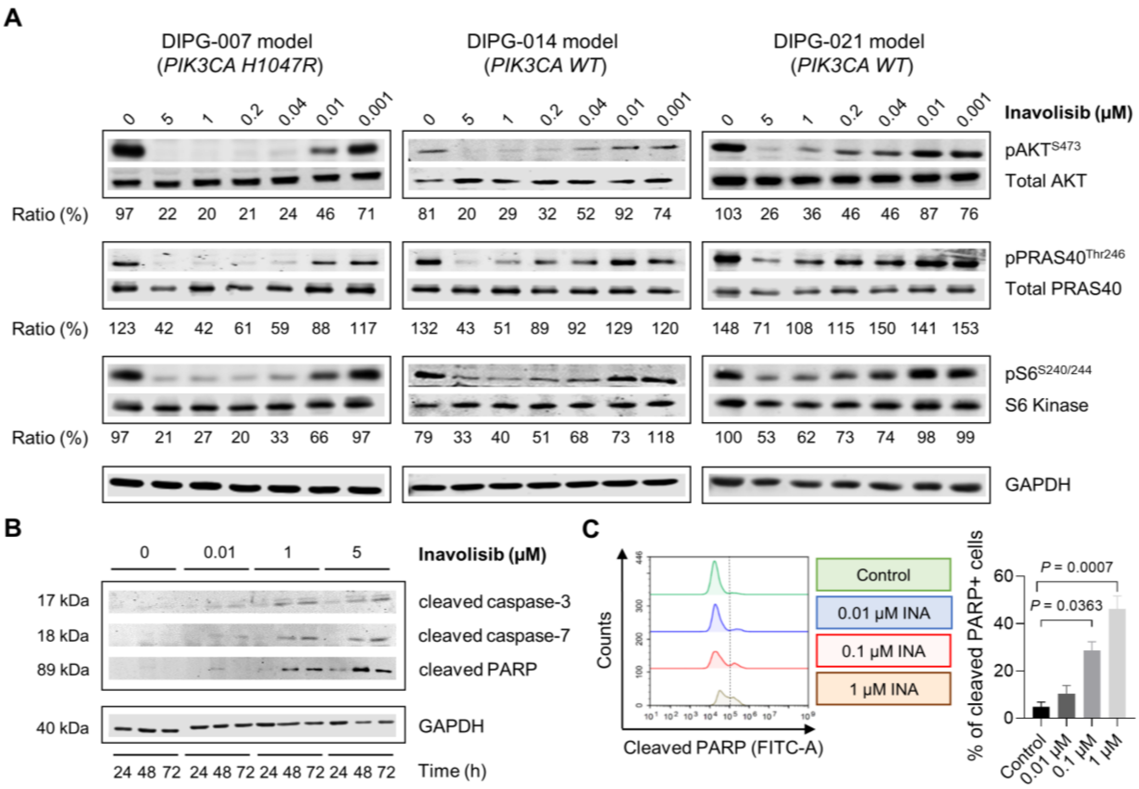

Figure 36. PI3K/Akt pathway inhibition and apoptotic response to inavolisib *in vitro*. (A) Pharmacologic effects on downstream signalling in response to inavolisib in DIPG-007, DIPG-014 and DIPG-021 cells by Western Blot. GAPDH was the loading control, used to normalize the protein expression levels of Akt, pAkt, PRAS40, pPRAS40, S6 Kinase and pS6. The relative ratio (represented in percentage) of pAkt/Akt, pPRAS40/PRAS40 and pS6/S6K was calculated for each DIPG model. (B) Inavolisib induced the activation of apoptotic-related proteins in DIPG-007 cells. After treatment with inavolisib (0, 0.01, 1 and 5 µM) for 24, 48 and 72 h, Western Blot assay were performed against cleaved caspase-3, cleaved caspase-7 and cleaved PARP. GAPDH was used as a loading control. (C) Inavolisib induced dose-dependent apoptosis in DIPG-007 cells. Cells were treated with inavolisib (0, 0.01, 0.1 and 1 µM) for 24 h and stained with cleaved PARP. The apoptosis induced by inavolisib was quantified. The percentage of apoptotic cells is shown in the bar graph. The data are represented as mean ± SD of four biologic replicates.

3. Inavolisib crosses the BBB and increases the overall survival of an orthotopic DIPG model.

We investigated the biopharmaceutical profiles of inavolisib and ipatasertib in terms of CNS penetration and *in vivo* anticancer activity in mice bearing intracraneal DIPG-007 xenografts. For the efficacy study, animals received daily oral ipatasertib (25 or 100 mg/kg) or daily oral inavolisib (50 mg/kg). For inavolisib, we observed transient toxicity induced by treatments (10% body weight loss during the initial days of treatment) (**Figure 37A**). Two cycles of inavolisib, for a total of 10 days in the first cycle and 10 days in the second cycle, prolonged the median survival of DIPG-007 xenografts to 85 days, significantly higher compared to control mice, which survived 75 days (P = 0.0072) (**Figure 37B**). Inavolisib concentrations in plasma achieved a maximum of 12.9 ± 0.56 µM after a single 50 mg/kg dose, and they were detectable for 24 h in the low micromolar range (**Figure 37C**). In the brain, inavolisib achieved a maximum concentration of 0.70 ± 0.12 µM at 0.5 h, and persisted above 0.01 µM until 18 h post-administration (**Figure 37C**). Because the IC_{50} value of inavolisib for DIPG-007 cells *in vitro* is 0.01 µM, these pharmacokinetic data are considered favorable and they would explain that mice receiving the drug survived longer than the control mice.

For ipatasertib, we observed transient toxicity only at the high dosage level (**Figure 37D**). Despite the administration of long treatments to the mice, for a total of 25 days, the treatment did not achieve therapeutic benefit in the xenografts, regardless of the dose (**Figure 37E**). Ipatasertib concentrations in plasma achieved a maximum of 13.1 ± 12.5 µM after a single 100 mg/kg dose, and they stayed in the range 3.59 - 2.19 µM between 2 h and 24 h (**Figure 37F**). In the brain, ipatasertib achieved a maximum concentration of 1.05 ± 0.93 µM at 0.5 h, and persisted in the range 0.87- 0.42 µM until 24 h post-administration (**Figure 37F**). Because the IC_{50} value of ipatasertib for DIPG-007 cells *in vitro* is 1 µM, these pharmacokinetic data, even at a non-clinically feasible dose (these mice received 100 mg/kg, while 25 mg/kg is the recommended dose for mice), are considered not favorable and they would explain that mice receiving the drug did not survive longer than the control mice.

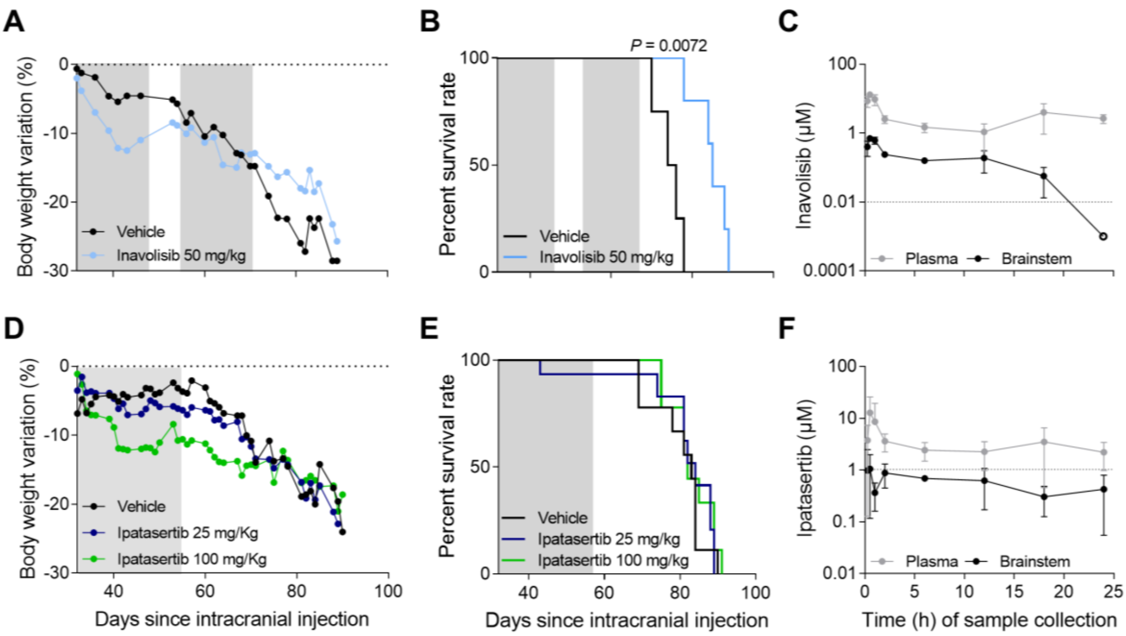

Figure 37. *In vivo* survival and pharmacokinetics of inavolisib and ipatasertib. (A) Body weight variation of mice treated with inavolisib, compared to controls. (B) Survival curves for mice treated with 50 mg/kg inavolisib, compared to vehicle-treated controls. (C) Plasma and brain concentrations of inavolisib up to 24 h post-administration of a single dose of 50 mg/kg in healthy mice. The discontinuous line show the IC_{50} threshold of inavolisib for DIPG-007. A different symbol shape indicates values below the detection limit of the technique. (D) Body weight variation of mice treated with ipatasertib, compared to controls. (E) Survival curves for mice treated with 25 or 100 mg/kg ipatasertib, compared to vehicle-treated controls. (F) Plasma and brain concentrations of ipatasertib until 24 h posterior to a single dose of 100 mg/kg in healthy mice. The discontinuous line show the IC_{50} threshold of ipatasertib for DIPG-007.

4. PI3K inhibition with inavolisib promotes tumor growth arrest *in vivo*.

Having characterized the CNS distribution kinetics of inavolisib and ipatasertib, we next investigated their pharmacodynamics in orthotopic DIPG xenografts. We treated 16 mice with daily oral dosages of 25 mg/kg ipatasertib, and 5 mice with 50 mg/kg inavolisib, and sacrificed them 2 h after the last dose of treatments. To evaluate tumor burden and histology in treated tumor-bearing brains, compared to controls, we performed an IHC staining of human nuclei. We found no differences in the tumor load after ipatasertib treatment, compared to controls, but the animals treated with inavolisib had less infiltration of cancer cells in the brain parenchyma (**Figure 38A**). Using the ddPCR technique developed in this PhD thesis, we processed paraffin slides and found that DIPG cells counts were lower in the inavolisib-treated tumors, as quantified by the number of human *H3F3A* copies in the sample (**Figure 38A, B**).

Next, we aimed to assess response to inavolisib in liquid biopsies. First, we performed a study in DIPG cells in culture, exposed to inavolisib, and we found an increase in *H3F3A* quantification in the supernatants following treatment, which we explained as a phenomenon related to cell death due to the treatment efficacy (**Figure 38C**). Considering these results *in vitro*, we isolated the ctDNA from the CSF of eight tumor-bearing mice, four of them treated with 50 mg/kg inavolisib, and four with vehicle, for 14 days. In agreement with the *in vitro* assay, we observed that the amount (ng) of human *H3F3A* gene present in the CSF obtained from the mice treated with inavolisib was significantly higher than the amount in those CSF obtained from animals treated with vehicle (P = 0.0159) (**Figure 38D**). Thus, the ddPCR technique in the CSF might be useful to detect apoptotic processes occurring in mice following successful anti-DIPG treatments.

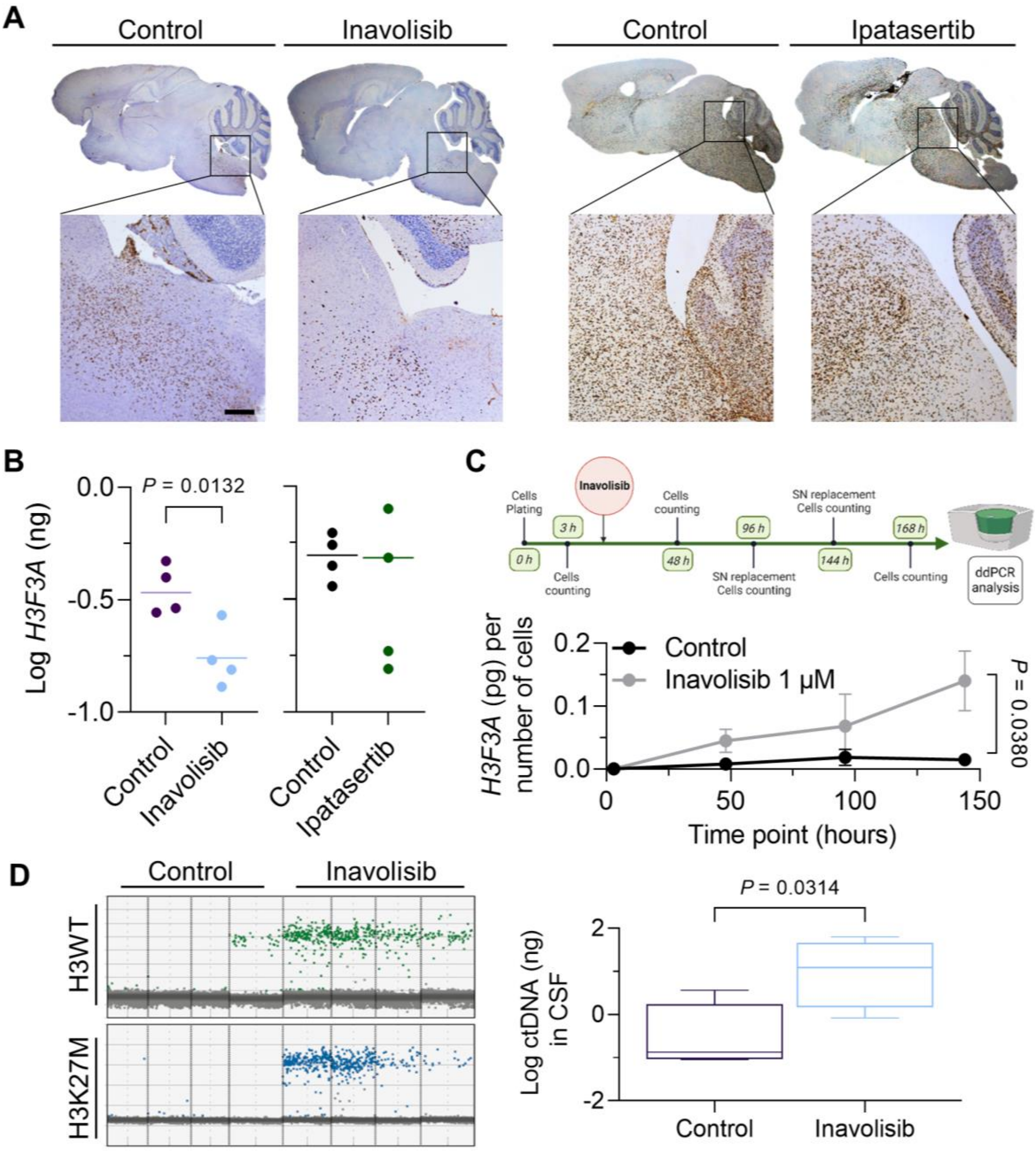

Figure 38. Efficacy of ipatasertib and inavolisib in DIPG-007 xenografts. (A) Representative immunostainings of human nuclei in animals of the efficacy study (x5 magnification, scale bar = 400 µm, scale bar 1.25x = 1.6 mm). (B) Quantification of the human *H3F3A* gene (ng) in paraffin slides from DIPG-007 tumor-bearing mice obtained during treatment with inavolisib and ipatasertib, compared to untreated mice. (C) *H3F3A* (ng) quantification (per viable cell) in the ctDNA isolated from the supernatant of DIPG-007 cell cultures, with or without exposure to 1 µM inavolisib. Dots in the graphics represent the mean ± SEM of two replicates. Šídák's multiple comparisons test. (D) Assessment of the response to inavolisib in the CSF of DIPG xenografts obtained during treatment. Graphics show the droplets for the alleles *H3F3A* K27M (blue) and *H3F3A* WT (green) from four representative samples. The box plot represents all data obtained by ddPCR.

Chapter 7. Discussion

This thesis contains two main parts. The aim of the first part was to improve the assessment of preclinical treatment efficacy in pHGG. To do so, I refined preclinical models and methods, such as a ddPCR technique to detect human DNA in pHGG xenografts established in mice. I took advantage of primary pHGG models, most of them DIPG, already established at the HSJD laboratory from biopsies and autopsies of patients, and I processed new patient samples to establish new models. We applied successfully the new preclinical tools to measure the efficacy of several pharmacological treatments in DIPG, and we detected the potential therapeutic activity of some of them *in vivo*. In the second part, I focused on the hypothesis that the PI3K/Akt pathway is actionable in pHGG with newly developed small molecules that we obtained through collaborative agreements with the company Roche. We performed a whole research program to characterize this pathway in pHGG and to test the drugs, identifying one PI3K inhibitor as a potential candidate for clinical use.

The ultimate goal of my PhD thesis was to provide consistent evidence to decide on whether the new preclinical findings are translatable into clinical applications for the treatment of patients with DMG (**Figure 39**).

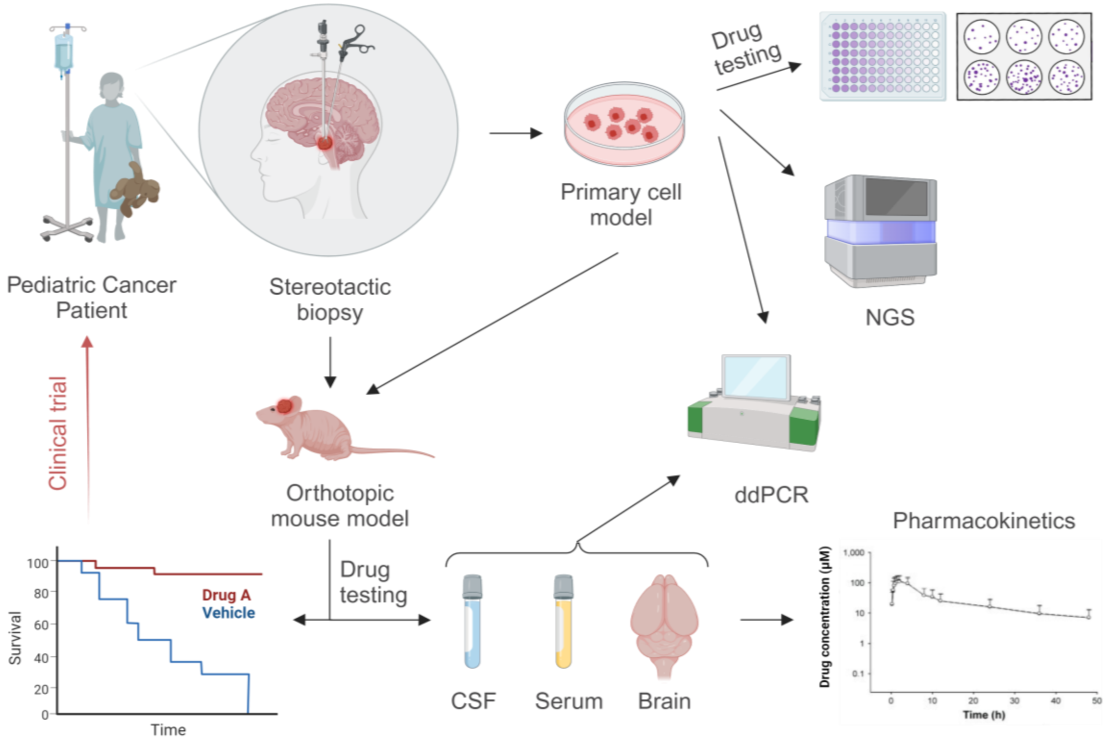

Figure 39. Graphical abstract. Workflow established during this PhD project.

1. DIPG disease symptoms positively correlated with human histone-3 in pHGG xenografts.

In the first part of the thesis, I developed preclinical methods to characterize and quantify tumor burden in xenografts of the pHGG subclasses DMG H3 K27-altered (DIPG-007 and DMG-005), diffuse hemispheric glioma H3 G34-mutant (GBM-002) and diffuse pediatric-type high-grade glioma H3-wildtype and IDH-wildtype (GBM-001). These xenografts are 100% lethal to immunodeficient mice, but methods to follow up disease progression and measure treatment efficacy need refinement. In my study, I established and compared two methods to quantify objectively the tumor burden in the xenografts, namely the body weight loss method and the preamplified - droplet digital PCR method that quantifies human ctDNA in paraffin brain tumor samples and in fresh CSF.

In our work with xenografts, we wanted to avoid the manipulation of the cancer cell genome through the insertion of tracer reporter genes encoding for fluorescent proteins and/or luciferase. This technique allows the continuous follow-up of the intracraneal tumor burden through imaging[191], but it may introduce a range of stressors and disruptions that negatively impact the viability of primary cultures[192,193]. Also, significant issues may arise due to the variability in the plasmid copy number introduced to the cells, resulting in a heterogeneous cell population with different levels of luciferase expression[194]. Bioluminiscence imaging (BLI) techniques are used for monitoring tumor growth and treatment efficacy in preclinical studies[43,84,195-198]. There exists an excellent correlation between the amount of BLI signal detected and the tumor volume, especially during the early stages of the disease. However, at extremes, when the BLI signal is very low or the tumor is very large, the correlation is slighter[199]. In intracranial studies, it has been observed that if the mouse has hydrocephalus or intracranial hemorrhage, BLI signal values increase exponentially, while MRI evaluation indicates the absence of visible tumors[199]. Also, necrotic and hypoxic regions within tumors may distort BLI signals by displaying little to no bioluminescence due to the absence of viable[200], luciferase-expressing cells, thus underestimating tumor size[201]. Other imaging modalities, such us positron emission tomography (PET) and magnetic resonance imaging (MRI) are not sufficiently sensitive for the comprehensive longitudinal monitoring of infiltrative pHGG xenografts. These techniques are primarily effective only at the terminal stage of the disease, coinciding with the disruption of the blood-brain barrier (BBB)[84,95,202]. Furthermore, mice need to be under anesthesia for extended periods, and these techniques generally assess indirect indicators of tumor pathology, like focal edema, which may not depict the tumor size and boundaries[195].

In previous studies, we followed up pHGG engraftment through the evaluation of animal weight loss, which was accompanied by slight motor symptoms such as mild ataxia, slightly altered balance, and head nodding, due to the infiltration of the brainstem and cerebellum[88,167,203,204]. In the DIPG-007 xenograft, motor symptoms and weight loss appear late (around 60 days) after tumor inoculation and are sufficient to evaluate the effect of treatments on mouse survival[205]. Our experience using this method is consistent with a previous report by Hart *et al*., which standardized the DIPG xenograft mouse model using DIPG-007 cells for preclinical research[206]. However, these methods fall short to detect changes in tumor burden during the period in which animals receive treatment, usually comprising day 30 to day 50[89,94,167]. In addition, some treatments induce moderate weight loss due to toxicity, which can lead to erroneous interpretation of the disease stage[89,207-211]. To address this, in previous studies we quantified tumor burden and pharmacodynamic parameters in FFPE tissues obtained from a limited number of mice that were sacrificed after the completion of their treatments[89,94]. This method, however, had the limitations of being terminal (i.e., mice need to be euthanized) and tumor burden analysis was only two-dimensional in tissue slides, which led us to propose the current work on the CSF liquid biopsy followed by ddPCR of the mutant H3 DNA. CSF is a well-established liquid biopsy source for DIPG diagnosis[77,212-215]. In adult and pediatric patients with diffuse gliomas, ddPCR quantification of ctDNA copies in the CSF is feasible without preamplification for the mutant versions of genes *IDH1*, *IDH2*, *TERT*, *TP53*, *PIK3CA*, *H3F3A, ACVR1* and *ATRX*[74,75,216].

In our study, ddPCR detection of *H3F3A* copies in the mouse CSF was not possible without a DNA preamplification step, likely due to the small volume that could be collected, around 5 µL of sample. The preamplification approach was applied to enhance the detection of mutations in the blood ctDNA from patients with esophageal adenocarcinomas[166]. The technique detected as low as 0.05%

of mutant fraction for three targets genes of esophageal adenocarcinoma, such as *SMAD4*, *TP53*, and *KRAS*, compared with non-preamplified samples, where mutations were not detectable[217]. The fact that, in our hands, *H3F3A* copies were below the limit of detection in the mouse blood could be explained by the effect of the BBB at the tumor site, which might be a primary obstacle for ctDNA detection in plasma[67,75,218,219]. The presence of DNases in blood could also contribute to an insufficient detection[220-222].

Our preclinical results in mice using ddPCR detection of *H3F3A* copies in the CSF intended to replicate the clinical experience. For instance, Panditharatna *et al*. used the DNA preamplification technique to detect low VAF somatic mutations of H3 (K27M, G34R), *ACVR1* (G328V, R206H), and *PPM1D* (E525X), among other genes, in the CSF and plasma of patients with DMG[77]. H3K27M ctDNA was identified in 87% (20 out of 23 subjects) of CSF samples and 90% (18 out of 20 subjects) of plasma samples from patients, but at lower levels[77]. Also, Li *et al*. optimized the ctDNA preamplification for their ddPCR-based technique for H3 K27M, using matched DMG tissue and liquid biopsy specimens[165]. They observed more mutant droplets and greater VAF values with preamplified specimens compare to not-preamplified ones, with no change in test specificity[165]. This observation aligns with our study, in which an increase in the number of droplets detected in CSF samples was noted following preamplification, compared to samples without preamplification. In plasma samples, despite the use of preamplification PCR, we were unable to detect droplets, contrary to the findings of Panditharatna *et al*. This discrepancy is likely due to the smaller volume of plasma obtained from mice compared to the larger volumes collected from patients. On the other hand, the results of the ctDNA quantification in our *in vitro* assay are in agreement with the study performed by Stallard *et al*., in which the increase of bioluminescent DIPG-007 cells correlated with the gain of K27M copies in the cell supernatant due to cell proliferation. In the Stallard study, a cytotoxic treatment (8 Gy irradiation) increased abruptly the amount of mutant ctDNA in the media[76]. Similar findings have been reported in subcutaneous lung cancer xenograft models, where ctDNA levels were monitored during radiotherapy and found to increase following 6 Gy treatment[223].

Currently, there is limited research related to the study of ctDNA in preclinical models. The few studies available have primarily focused on extracranial tumors, using serial samples of plasma as the main source of ctDNA[224,225], and no similar studies have been reported for intracranial xenografts previously, neither collecting serial samples of CSF for the analysis of ctDNA, as I did in my PhD work. It is interesting to note that some of these studies have correlated ctDNA concentration with tumor size in mice[225,226]. Wei *et al*. detected through ddPCR that the counts of *EGFR* T790M and *KRAS* Q61H mutations in plasma-derived ctDNA increased proportionally with the tumor weight of H1975 and H460 subcutaneous xenografts of lung cancer.[225] They found that when the tumor weight was below 400 mg, the detection of these mutations in plasma was relatively low (mostly negative), whereas when the tumor exceeded 1500 mg, they could detect up to 8280 mutated copies/mL[225]. These data suggest that tumor volume is crucial for this analysis. These findings align with ours, as the technique shows high sensitivity even for preclinical assays. As a limitation of our method, the detection of human *H3F3A* derived from ctDNA in the CSF cannot be detected until the tumor is more advanced, although this value can be correlated with mouse weight loss, which is equivalent to tumor weight for extracranial tumors.

In summary, due to limitations occurring during the last stages of tumor growth in the mouse brain, most studies still use the parameter of animal body weight loss as an endpoint for evaluating animal welfare deterioration and determining the point at which the animal should be sacrificed[88,89,198,205,211,227,228]. Our current study has validated that the body weight loss parameter correlated well with the real tumor burden in the management of DIPG preclinical studies, therefore validating *in vivo* experiments performed in this thesis. In this regard, studies with DIPG xenografts included in the Chapter 4 of this thesis, in which we evaluated *ACVR1* inhibitors, trametinib, ONC201 or taselisib, led to important strategic decisions to continue or cease the clinical development of drugs and to either recommend or not investigational treatments for application at our institution.

2. The PI3K/Akt pathway is dysregulated in pHGG/DIPG.

The phosphoinositide 3-kinase (PI3K)/ protein kinase B (Akt) pathway is crucial in various cancers, regulating cell survival, metastasis, metabolism, angiogenesis, and inflammatory factor recruitment in the tumor environment. This signalling cascade operates immediately downstream of various upregulated and mutant growth factor receptors in the cellular membrane that transmit oncogenic signals[229] and can become abnormally activated through various mechanisms, including genomic alterations such as mutations in *PIK3CA*, *PTEN*, *Akt*, *TSC1*, and *mTOR*[230]. One of the primary objectives of my PhD work was to characterize the PI3K/Akt/mTOR signalling activation in our pHGG/DIPG models.

Our interest to test inhibitors for the PI3K/Akt pathway is substantiated by several studies. In the context of DIPG, Duchatel *et al*. utilized a CRISPR/Cas9 loss-of-function screen to identify a significant genetic dependency on the *PIK3CA* and *MTOR* genes for maintaining cell growth and proliferation *in vitro*, emphasizing in the therapeutic potential of the *PIK3CA* inhibitor, paxalisib[211]. Recently, Fortin *et al*. utilized transgenic mouse models to elucidate the role of *PIK3CA* gain-of-function mutations in tumorigenesis. Their study demonstrated that concurrent mutations in *Hist1h3b*, *ACVR1*, and *PIK3CA* were necessary to induce high-grade diffuse gliomas in mice, underscoring the cooperative nature of these genetic alterations in glioma development[40]. These findings confirmed the potential of targeting proteins within this pathway for therapeutic interventions.

In pHGG, aside from histone mutations, the most prevalent molecular alterations involve the overexpression of receptor tyrosine kinase (RTK) family members. In this regard, our results showing most RTK are altered in our samples, consistent with previous findings. *PDGFRA* has been identified as the most commonly altered RTK in DIPG[10], significantly impacting patient prognosis, as its amplification is associated with reduced overall survival compared to patients lacking this alteration[178]. Mackay *et al*. also reported *EGFR* amplifications in 4% and *MET* amplifications in 2% of 834 pHGG cases[10]. *IGF1R* mutations were observed in a very small proportion of cases, alongside focal amplifications of the *IGF1R* gene[10,26]. These RTK aberrations are associated with increased expression and lead to dysregulation of these signalling receptors, triggering downstream signalling cascades through activation of the PI3K/Akt or MEK/Erk pathways[231].

Using gene expression analyses, we found differences in the expression of catalytic (p110) versus regulatory subunit (p85), encoding by *PIK3R1* and *PIK3R2*, being the regulatory subunit the most significantly altered across our models, compared to healthy brain control, in contrast to the catalytic subunit, which shows more stable and less variable expression, independent on the harboring alterations. Actually, regulation of the PI3K activity depends on the p85-to-p110 ratio. According with our results, in many cells it has been found that p85 levels exceed p110 levels[232]. This excess may lead to competition between free p85 monomers and the p85-p110 complex for binding to insulin receptor substrates (IRS) protein, which acts as an adaptor for PI3K to the RTK, reducing PI3K activity. Various p85 binding partners, such as bromodomain 7 (BRD7), play a role in regulating PI3K activity. BRD7 binds to p85 and sequesters it in the nucleus, reducing the interaction of free p85 with IRS and thus improving PI3K signalling by the p85-p110 complex union, as described in liver cells, although it produces contrary effect in HeLa cells[232]. We did not address these events in this PhD work. Regarding the brain development, it is regulated in part by trophic factors, such as insulin-like growth factor-1, making neuronal cell survival dependent on PI3K/Akt signalling. This pathway is thus essential for a proper brain size and function during embryogenesis, emphasizing the reliance of early neuronal stem cells on PI3K signalling for brainstem formation. This dependence also underlines the role of a dysregulated PI3K pathway in promoting the malignant growth seen in DIPG[211]. In DIPG, bromodomain proteins have been extensively studied. Research has shown that the loss of genomic H3K27me3 is associated with an increase in H3K27ac, a modification recognized by BRD proteins[233]. This recognition promotes the recruitment of RNA polymerase II and enhances transcriptional activity. Both of these mechanisms may play a role in tumorigenesis in DIPG.

PTEN, a negative regulator of the PI3K/Akt pathway, prevents the phosphorylation of PIP2 to PIP3, thereby inhibiting the recruitment and activation of PI3K at the cell membrane. PTEN functions as a tumor suppressor in tumor cells and exhibits higher activity compared to normal tissue, where cellular metabolism is lower[234]. The inactivation of PTEN via chromosomal deletion at 10q or oxidative inactivation at the active cysteine site Cys124, through the formation of a disulfide bond with the adjacent cysteine residue Cys71, has been identified as an early event in DIPG[28,235]. Our results revealed *PTEN* overexpression in five of our models (DIPG-008, DIPG-012, DIPG-013, DIPG-021, and DMG-005), that might imply an active and functional role in inhibiting PI3K activation and preventing the overexpression of downstream genes, despite the gene harboring no aberrations. Other cell lines, GBM-002, displayed a nonsense mutation in *PTEN*, which generates a premature stop codon, displaying a truncated protein[236]. As described for the *TP53* gene, it is possible that mRNA overexpression occurs when a gene harbors a nonsense mutation, as part of a compensatory response. Although nonsense mutations generally trigger the Nonsense-Mediated Decay (NMD) mechanism to degrade the defective mRNA, in some cases, the cell may evade this mechanism and increase transcription of the mutated gene to compensate the loss of the functional protein[237]. In other models, such as DIPG-007, DIPG-011, or DIPG-014, *PTEN* expression is either loss or significantly reduced compared to healthy brain tissue. Both of these phenomena may result in the hyperactivation of the PI3K/Akt pathway[188]. Extensive *in vitro* and *in vivo* data suggest that targeting PTEN activity could offer therapeutic benefits[238]. However, at the translational level, no clinical trials are currently focused on drugs specifically targeting the loss of the PTEN tumor suppressor. Nevertheless, many trials are investigating the efficacy of PI3K and mTOR inhibitors using PTEN deficiency or loss of expression as a predictive biomarker, suggesting these treatments could be more effective in cases with such genomic alterations (NCT06360588, NCT04439188, and NCT02449538). Considering this, some patients with PTEN-deficient DIPG may potentially benefit from these drugs, which are currently being studied for other tumor types, including pediatric osteosarcoma (NCT04690725).

The Ras/MEK/ERK and PI3K/Akt/mTOR pathways were initially viewed as distinct linear signalling cascades triggered by separate stimuli. However, early studies suggested potential interactions between these pathways, with evidence of mutual regulation and coordination of downstream functions[154]. The MEK/Erk pathway, along with PI3K/Akt, drive cell proliferation by promoting the cell cycle and gene expression required for growth[239]. Compensatory signalling interactions between the PI3K/Akt and MEK/Erk pathways are well-documented in adult cancers[154,240], including glioblastomas[241,242], and have also been under investigation in DIPG tumors for several years[162,163], wherein inhibition of one pathway leads to the activation of the other, thereby maintaining cell survival and proliferation[162,243]. This compensatory mechanism is crucial for understanding the resistance to targeted therapies and the complexity of signalling networks in DIPG[163,244]. Wu *et al.* demonstrated that dual inhibition of PI3K/Akt and MEK/Erk pathways with perifosine and trametinib resulted in more significant suppression of tumor growth in DIPG cells, compared to targeting either pathway alone[162]. Additionally, Chang *et al*. investigated the combination of a PI3K inhibitor with trametinib and found that this treatment suppressed the malignant growth of DIPG cells both *in vitro* and *in vivo*, leading to prolonged survival[163]. However, they observed considerable systemic toxicity, including weight loss and food avoidance, when the drugs were administered systemically. This aligns with clinical findings, which indicate that dose-limiting toxicities are common for these agents and may be exacerbated when used in combination[163]. We observed that in the DMG-005 cell model, the MEK/Erk pathway appeared to be overactivated while *PTEN* suppressed PI3K activation. This effect was not observed in other models showing *PTEN* overexpression, possibly due to the limited analysis of MEK/Erk pathway genes or the greater relevance of other pathways, such as AMPK, Wnt/β-catenin, NF-κB, or JAK/STAT, for the survival and proliferation of these models[245].

To evaluate the activation status of the PI3K/Akt pathway in our DIPG cell models, we used the phosphorylation of Akt, a direct readout of PI3K activity, as a reliable indicator of pathway activation[246]. Consistent with our expectations, DIPG cell models that exhibited upregulation of PI3K-related genes also demonstrated increased Akt activation. Interestingly, DIPG-008 showed an overexpression of *PTEN*, while pAkt, pPRAS40, pS6 and also pErk remained lower than in other models. This finding is in agreement with the described function of *PTEN* to inhibit pathway signalling[247]. A similar effect was observed in DIPG-021, in which PI3K-related downstream pathway proteins were less active, while phosphorylated Erk was increased. This suggests that the MEK/Erk signalling pathway plays a crucial role in the survival and proliferation in DIPG-021, despite the activity of the PI3K/Akt pathway. Additionally, DIPG-013 exhibited hyperactivation of Akt related genes and also Erk, despite downregulation of PIK3 and MEK-related genes and *PTEN* overexpression (as a compensatory mechanism to counteract the excessive activation of Akt) at the RNA level and no alterations harbored at DNA level. This observation may be attributed to the feedback loops generated between these two pathways, which are investigated in DIPG, wherein MEK has the potential to activate both Erk and Akt, along with downstream effectors[241].

In tissue samples from patients with DIPG, we observed overexpression of *EGFR*, *PDGFRA*, and *FGFR1*, suggesting that targeting RTKs could be a suitable therapeutic approach for pHGG tumors. Several clinical trials are active or recruiting patients to test tyrosine kinase inhibitors, typically by co-targeting multiple RTKs to prevent drug resistance mechanisms. A phase 1/2 clinical trial is now recruiting patients with pediatric solid tumors, including CNS tumors harboring *PDGFRA* and/or *KIT* mutations (non-synonymous point mutations, insertions, and deletions) or amplifications, to test avapritinib (NCT04773782). Additionally, a phase 1 study is active to test EGFR806-specific CAR T cells as locoregional immunotherapy for EGFR-positive recurrent or refractory pediatric CNS tumors (NCT03638167). These developments highlight the potential of RTKs as a target for pHGG tumor therapy. The clinical trials for patients with pHGG are currently active, focusing on targeting PI3K/mTOR pathway activation, typically in combination with other drugs such as ribociclib, a CDK4/6 cell cycle inhibitor (NCT05843253). Additionally, paxalisib (GDC-0084), a selective PI3K inhibitor, has been tested in clinical trials for pediatric patients with newly diagnosed DIPG or DMG (NCT03696355). These data suggest the importance of targeting the PI3K/Akt/mTOR pathway in patients diagnosed with pHGG where this signalling pathway is overactivated.

To summarize, our findings confirm that the PI3K/Akt/mTOR pathway plays a key role in pHGG tumorigenesis, providing a potentially actionable target, and also in resistance mechanisms, in which the RAF/MEK/Erk signalling pathway could be involved.

3. Inavolisib demonstrates potent preclinical efficacy and robust CNS distribution in DIPG xenografts with intact BBB.

The safety and efficacy of the PI3K/Akt pathway inhibitors ipatasertib and inavolisib has been proven in preclinical cancer models and clinical trials with encouraging results[138,151,248-250]. For my PhD studies, we used a preclinical platform of DIPG cell models and an animal model for biodistribution and survival studies. We demonstrated that both ipatasertib and inavolisib mono-therapies selectively inhibited cell growth in a dose and model-dependent manner *in vitro*. Treatment with ipatasertib did not increase the overall survival of the mice *in vivo*, while inavolisib significantly inhibited tumor burden and prolonged survival in a DIPG orthotopic model.

Numerous studies suggested that cancer cell lines with *PTEN* loss and amplified or mutant *PIK3CA* are more likely to respond to ipatasertib[137,138]. Similar investigations have been reported for inavolisib, which selectively inhibits proliferation of *PIK3CA*-mutant breast cancer cell lines to a greater extent, compared to *PIK3CA* wild-type cells[151]. DIPG-007 harbors a mutation in *PIK3CA* gene, encoding p-His1047Arg (also known as H1047R) which induces a substitution of the amino acid histidine at position 1047 with the amino acid arginine in the C-terminal portion of the kinase domain of the *PIK3CA* p110α protein[251-253]. This hotspot mutation induces an oncogenic transformation through increasing the lipid kinase activity of p110α and a gain of function of PI3K[254]. As described for other tumors, the presence of the mutation in DIPG-007 conferred cell sensitivity to ipatasertib and inavolisib. Our findings in DIPG-007 are consistent with a high degree of inhibition of molecular downstream targets of PI3K as demonstrated in western blots, in a dose and model-dependent manner.

Several drugs targeting the PI3K/Akt signaling are being developed and tested in clinical trials due to the constitutive activation of the pathway signaling in many pediatric brain tumors[255]. Unfortunately, identifying the right targets is not enough to predict drug activity in brain diseases, especially in the case of several CNS neoplasms in which the BBB remains intact[256]. To have activity, it is mandatory that a proper concentration of drug reaches the tumor cells and resides the adequate time in its site of action. Currently, thePI3K signaling pathway inhibitor ipatasertib is in phase-II/III clinical trials for adult breast cancer (NCT04177108) and inavolisib has been recently approved by the FDA for the treatment of metastatic *PIK3CA*-mutated breast cancer, but neither of them has been tested in clinical trials in children with pediatric tumors, and their biodistribution through the CNS remains unknown. In our orthotopic intracranial xenograft model, inavolisib reached the brain at concentrations sufficient to decrease the tumor burden in treated animals, while ipatasertib was clearly unable to cross the BBB sufficiently to produce tumor inhibition. We performed the *in vivo* studies using a daily oral dosage, rather than considering a local administration route such as direct intracranial drug injection via convection-enhanced delivery (CED), because drugs administered by CED must be water-soluble at physiological pH for effective brain delivery[257]. We also consider that local administration routes are not clinically feasible for drugs needing daily administration.

In the last decade, liquid biopsy raised as a useful and up-to-date method to monitor cancer malignancies, especially for brain tumors, due to the stereotactic or open biopsies carry an uncertain risk-benefit for the feasible surgical complications. Furthermore, neurosurgical biopsies provide limited amounts of tumor tissue, which cannot represent its own heterogeneity for an accurate pathologic and molecular diagnoses[213]. Isolated ctDNA present in the CSF is used as a potential tool to detect genomic alterations, providing information about tumor heterogeneity and treatment responses by tumor burden quantification. There are several technologies to detect the ctDNA molecules, and among them ddPCR is emerging as an effective instrument to quantify somatic mutations present in CNS tumors[258]. Previous *in vitro* studies have demonstrated that *H3F3A* K27M mutation present in DIPG cells may be detected in the ctDNA released into the cells supernatant due to cell proliferation, simulating ctDNA release into the CSF, by ddPCR[76]. Also, ctDNA abruptly increases on the media when cells are treated with radiotherapy (standard of care in DIPG) due to cell death[76]. Using the ddPCR method developed in the first part of the thesis, we detected an increase of ctDNA release into the CSF in animals treated with inavolisib during 14 days, suggesting that ctDNA levels in the CSF could rise following successful treatments in patients with brain tumors. The ctDNA could thus be used as biomarker for drug response in DIPG preclinical and clinical studies. This finding should be addressed in prospective clinical trials.

In this third part of the thesis, I emphasize that our positive preclinical data for inavolisib could have therapeutic implications in patients with pHGG carrying *PIK3CA* mutations, which should be addressed in prospective trials. Of note, the fact that DIPG shows substantial intratumoral clonal heterogeneity[175] highlights the importance of developing combination therapies to improve patient outcomes. Moving forward, it will be crucial to investigate potential resistance mechanisms that may arise in tumor cells treated with inavolisib, or others. Thus, new therapeutic approaches should foresee that monotherapy will likely not be sufficient to control disease, and treatment combination strategies should be considered early in future clinical trials.

Chapter 8. Conclusions

In this thesis, I contributed to expand and improve the preclinical models and methods to assess the efficacy of new therapies for DIPG, and I described the potential of the PI3K/Akt pathway as a therapeutic approach for DIPG harboring mutations in *PIK3CA* gene. The main conclusions are:

1. My work, added to previous work at HSJD, established and characterized 15 preclinical pHGG models covering three of the subclasses of the disease. The genetic profiles of these models match with the expected recurrent genomic alterations in genes such as *H3F3A*, *TP53*, *PPM1D*, *ACVR1*, *ATRX*, or *PIK3CA*. Four of such pHGG models are robust xenografts of the subclasses DMG H3 K27-altered (DIPG-007 and DMG-005), diffuse hemispheric glioma H3 G34-mutant (GBM-002) and diffuse pediatric-type high-grade glioma H3-wildtype and IDH-wildtype (GBM-001). These xenografts are 100% lethal to immunodeficient mice.
2. I developed sensitive and specific ddPCR methods to quantify allele frequencies of human genes *H3F3A* K27M, *H3F3A* G34R and *ACVR1* R206H in the ctDNA present in samples (FFPE slides and CSF) obtained from mice with pHGG.
3. The preamplification PCR is a feasible and necessary technique to allow for the detection of human *H3F3A* by ddPCR in small samples of 5 µL of CSF of mice with DIPG, increasing the sensitivity of the technique by 200 times, without losing specificity.
4. Collecting serial samples of CSF via the cisterna magna of mice with DIPG is a feasible technique. However, this liquid biopsy detects progressive disease only after animals start symptoms (weight loss), i.e., around day 60 after tumor inoculation in DIPG-007-bearing mice.
5. In mouse brain FFPE samples, both the ddPCR technique applied to the analysis of tumor gDNA and the count of human nuclei-positive cells are accurate methods to measure the degree of the disease progression, independently of the disease symptoms.
6. In DIPG-007 xenografts, the body weight loss parameter correlates very well with the real amount of tumor (tumor burden) in the mouse brain, calculated by IHC (human nuclei) or ddPCR. Thus, the body weight loss

method is an accurate method to follow up terminal disease and assess treatment efficacy in the xenograft DIPG-007.

7. Using the body weight loss method, we successfully evaluated the preclinical activity of potential therapeutic candidates, including *ACVR1* inhibitors, ONC201, trametinib and taselisib in DIPG-007 xenografts.
8. Using whole exome sequencing data, we found abnormalities in genes associated with the RTK-PI3K-MAPK axis among all the preclinical pHGG lines. Data from a limited number of patient samples (5 autopsies and 7 biopsies) confirmed the activation of the PI3K/Akt/mTOR pathway in at least 60% of the tumors.
9. Inavolisib, a PI3K inhibitor, and ipatasertib, an Akt inhibitor, demonstrated antiproliferative activity, in the low micromolar range, against DIPG models, being the *PIK3CA*-mutant model, DIPG-007, the most sensitive to both drugs.
10. Inavolisib inhibited vessel formation in the human brain endothelial cell line hCMEC/D3.
11. Inavolisib (50 mg/kg, oral, in mice) crosses the BBB and persists in the brain for more than 20 h at concentrations higher than 0.01 µM, the IC_{50} of DIPG-007 cells. In contrast, ipatasertib (100 mg/kg, oral, in mice), does not reach the necessary active concentration of at least 1 µM in the mouse brain.
12. Inavolisib increased significantly the survival of DIPG-007 bearing mice, likely due to its favorable CNS distribution profile. Ipatasertib did not increase the lifespan of these mice.
13. DIPG-007 bearing mice receiving inavolisib had significantly higher levels of human ctDNA in the CSF than control mice, suggesting that the ddPCR method in the mouse CSF could help detect the anticancer activity of candidate drugs.

Bibliography

1. Leary JB, Anderson-Mellies A, Green AL. Population-based analysis of radiation-induced gliomas after cranial radiotherapy for childhood cancers. *Neurooncol Adv.* 2022; 4(1):vdac159.

2. Gianno F, Giovannoni I, Cafferata B, et al. Paediatric-type diffuse high-grade gliomas in the 5th CNS WHO Classification. *Pathologica.* 2022; 114(6):422-435.

3. Hoogendijk R, van der Lugt J, Baugh J, et al. Sex-related incidence and survival differences in pediatric high-grade glioma subtypes: A population-based cohort study. *iScience.* 2023; 26(10):107957.

4. Vanan MI, Eisenstat DD. DIPG in Children - What Can We Learn from the Past? *Front Oncol.* 2015; 5:237.

5. Castel D, Philippe C, Calmon R, et al. Histone H3F3A and HIST1H3B K27M mutations define two subgroups of diffuse intrinsic pontine gliomas with different prognosis and phenotypes. *Acta Neuropathol.* 2015; 130(6):815-827.

6. Louis DN, Perry A, Reifenberger G, et al. The 2016 World Health Organization Classification of Tumors of the Central Nervous System: a summary. *Acta Neuropathol.* 2016; 131(6):803-820.

7. Loveson KF, Fillmore HL. Intersection of Brain Development and Paediatric Diffuse Midline Gliomas: Potential Role of Microenvironment in Tumour Growth. *Brain Sci.* 2018; 8(11).

8. Schwartzentruber J, Korshunov A, Liu XY, et al. Driver mutations in histone H3.3 and chromatin remodelling genes in paediatric glioblastoma. *Nature.* 2012; 482(7384):226-231.

9. El-Khouly FE, Veldhuijzen van Zanten SEM, Santa-Maria Lopez V, et al. Diagnostics and treatment of diffuse intrinsic pontine glioma: where do we stand? *J Neurooncol.* 2019; 145(1):177-184.

10. Mackay A, Burford A, Carvalho D, et al. Integrated Molecular Meta-Analysis of 1,000 Pediatric High-Grade and Diffuse Intrinsic Pontine Glioma. *Cancer Cell.* 2017; 32(4):520-537 e525.

11. Jones C, Baker SJ. Unique genetic and epigenetic mechanisms driving paediatric diffuse high-grade glioma. *Nat Rev Cancer.* 2014; 14(10).

12. Zhang X, Zhang Z. Oncohistone Mutations in Diffuse Intrinsic Pontine Glioma. *Trends in cancer.* 2019; 5(12):799-808.

13. Puget S, Beccaria K, Blauwblomme T, et al. Biopsy in a series of 130 pediatric diffuse intrinsic Pontine gliomas. *Childs Nerv Syst.* 2015; 31(10):1773-1780.

14. Hamisch C, Kickingereder P, Fischer M, Simon T, Ruge MI. Update on the diagnostic value and safety of stereotactic biopsy for pediatric brainstem tumors:

a systematic review and meta-analysis of 735 cases. *J Neurosurg Pediatr.* 2017; 20(3):261-268.

15. Walker DA, Liu J, Kieran M, et al. A multi-disciplinary consensus statement concerning surgical approaches to low-grade, high-grade astrocytomas and diffuse intrinsic pontine gliomas in childhood (CPN Paris 2011) using the Delphi method. *Neuro Oncol.* 2013; 15(4):462-468.

16. Wummer B, Woodworth D, Flores C. Brain stem gliomas and current landscape. *J Neurooncol.* 2021; 151(1):21-28.

17. Pollack IF, Agnihotri S, Broniscer A. Childhood brain tumors: current management, biological insights, and future directions. *J Neurosurg Pediatr.* 2019; 23(3):261-273.

18. Wilkinson KA, Henley JM. Mechanisms, regulation and consequences of protein SUMOylation. *The Biochemical journal.* 2010; 428(2):133-145.

19. Shanmugam MK, Arfuso F, Arumugam S, et al. Role of novel histone modifications in cancer. *Oncotarget.* 2018; 9(13):11414-11426.

20. Damodharan S, Lara-Velazquez M, Williamsen BC, Helgager J, Dey M. Diffuse Intrinsic Pontine Glioma: Molecular Landscape, Evolving Treatment Strategies and Emerging Clinical Trials. *Journal of personalized medicine.* 2022; 12(5).

21. Buccoliero AM, Giunti L, Moscardi S, et al. Pediatric High Grade Glioma Classification Criteria and Molecular Features of a Case Series. *Genes (Basel).* 2022; 13(4).

22. Chen CCL, Deshmukh S, Jessa S, et al. Histone H3.3G34-Mutant Interneuron Progenitors Co-opt PDGFRA for Gliomagenesis. *Cell.* 2020; 183(6):1617-1633.e1622.

23. Fontebasso AM, Liu XY, Sturm D, Jabado N. Chromatin remodeling defects in pediatric and young adult glioblastoma: a tale of a variant histone 3 tail. *Brain pathology (Zurich, Switzerland).* 2013; 23(2):210-216.

24. Ocasio JK, Budd KM, Roach JT, Andrews JM, Baker SJ. Oncohistones and disrupted development in pediatric-type diffuse high-grade glioma. *Cancer Metastasis Rev.* 2023.

25. Jones C, Karajannis MA, Jones DTW, et al. Pediatric high-grade glioma: biologically and clinically in need of new thinking. *Neuro Oncol.* 2017; 19(2):153-161.

26. Paugh BS, Broniscer A, Qu C, et al. Genome-wide analyses identify recurrent amplifications of receptor tyrosine kinases and cell-cycle regulatory genes in diffuse intrinsic pontine glioma. *J Clin Oncol.* 2011; 29(30):3999-4006.

27. Georgescu MM, Islam MZ, Li Y, et al. Global activation of oncogenic pathways underlies therapy resistance in diffuse midline glioma. *Acta Neuropathol Commun.* 2020; 8(1):111.

28. Koschmann C, Farooqui Z, Kasaian K, et al. Multi-focal sequencing of a diffuse intrinsic pontine glioma establishes PTEN loss as an early event. *NPJ Precis Oncol.* 2017; 1(1):32.

29. Rallis KS, George AM, Wozniak AM, et al. Molecular Genetics and Targeted Therapies for Paediatric High-grade Glioma. *Cancer Genomics Proteomics.* 2022; 19(4):390-414.

30. Nguyen AV, Soto JM, Gonzalez S-M, et al. H3G34-Mutant Gliomas—A Review of Molecular Pathogenesis and Therapeutic Options. *Biomedicines.* 2023; 11(7):2002.

31. Crowell C, Mata-Mbemba D, Bennett J, et al. Systematic review of diffuse hemispheric glioma, H3 G34-mutant: Outcomes and associated clinical factors. *Neuro-Oncology Advances.* 2022; 4(1).

32. Korshunov A, Ryzhova M, Hovestadt V, et al. Integrated analysis of pediatric glioblastoma reveals a subset of biologically favorable tumors with associated molecular prognostic markers. *Acta Neuropathologica.* 2015; 129(5):669-678.

33. Vuong HG, Le HT, Dunn IF. The prognostic significance of further genotyping H3G34 diffuse hemispheric gliomas. *Cancer.* 2022; 128(10):1907-1912.

34. Cohen KJ, Pollack IF, Zhou T, et al. Temozolomide in the treatment of high-grade gliomas in children: a report from the Children's Oncology Group. *Neuro-Oncology.* 2011; 13(3):317-323.

35. Korshunov A, Ryzhova M, Hovestadt V, et al. Integrated analysis of pediatric glioblastoma reveals a subset of biologically favorable tumors with associated molecular prognostic markers. *Acta Neuropathol.* 2015; 129(5):669-678.

36. Srikanthan D, Taccone MS, Van Ommeren R, Ishida J, Krumholtz SL, Rutka JT. Diffuse intrinsic pontine glioma: current insights and future directions. *Chin Neurosurg J.* 2021; 7(1):6.

37. Pathania M, De Jay N, Maestro N, et al. H3.3(K27M) Cooperates with Trp53 Loss and PDGFRA Gain in Mouse Embryonic Neural Progenitor Cells to Induce Invasive High-Grade Gliomas. *Cancer Cell.* 2017; 32(5):684-700.e689.

38. Hoeman CM, Cordero FJ, Hu G, et al. ACVR1 R206H cooperates with H3.1K27M in promoting diffuse intrinsic pontine glioma pathogenesis. *Nat Commun.* 2019; 10(1):1023.

39. Argersinger DP, Rivas SR, Shah AH, Jackson S, Heiss JD. New Developments in the Pathogenesis, Therapeutic Targeting, and Treatment of H3K27M-Mutant Diffuse Midline Glioma. *Cancers (Basel).* 2021; 13(21).

40. Fortin J, Tian R, Zarrabi I, et al. Mutant ACVR1 Arrests Glial Cell Differentiation to Drive Tumorigenesis in Pediatric Gliomas. *Cancer Cell.* 2020; 37(3):308-323.e312.

41. Deligne C, Hachani J, Duban-Deweer S, et al. Development of a human in vitro blood-brain tumor barrier model of diffuse intrinsic pontine glioma to better understand the chemoresistance. *Fluids Barriers CNS.* 2020; 17(1):37.

42. Warren KE. Beyond the Blood:Brain Barrier: The Importance of Central Nervous System (CNS) Pharmacokinetics for the Treatment of CNS Tumors, Including Diffuse Intrinsic Pontine Glioma. *Front Oncol.* 2018; 8:239.

43. Plessier A, Le Dret L, Varlet P, et al. New in vivo avatars of diffuse intrinsic pontine gliomas (DIPG) from stereotactic biopsies performed at diagnosis. *Oncotarget.* 2017; 8(32):52543-52559.

44. Wijaya J, Fukuda Y, Schuetz JD. Obstacles to Brain Tumor Therapy: Key ABC Transporters. *Int J Mol Sci.* 2017; 18(12).

45. Chaves C, Declèves X, Taghi M, et al. Characterization of the Blood-Brain Barrier Integrity and the Brain Transport of SN-38 in an Orthotopic Xenograft Rat Model of Diffuse Intrinsic Pontine Glioma. *Pharmaceutics.* 2020; 12(5).

46. Hauser P. Classification and Treatment of Pediatric Gliomas in the Molecular Era. *Children (Basel).* 2021; 8(9).

47. Sasaki T, Watanabe J, He X, et al. Intranasal delivery of nanoliposomal SN-38 for treatment of diffuse midline glioma. *J Neurosurg.* 2022:1-10.

48. Dalla C, Pavlidi P, Sakelliadou DG, Grammatikopoulou T, Kokras N. Sex Differences in Blood-Brain Barrier Transport of Psychotropic Drugs. *Frontiers in behavioral neuroscience.* 2022; 16:844916.

49. Warren KE. Diffuse intrinsic pontine glioma: poised for progress. *Front Oncol.* 2012; 2:205.

50. Vitanza NA, Monje M. Diffuse Intrinsic Pontine Glioma: From Diagnosis to Next-Generation Clinical Trials. *Current treatment options in neurology.* 2019; 21(8):37.

51. Brant-Zawadzki M, Atkinson D, Detrick M, Bradley WG, Scidmore G. Fluid-attenuated inversion recovery (FLAIR) for assessment of cerebral infarction. Initial clinical experience in 50 patients. *Stroke.* 1996; 27(7):1187-1191.

52. Giagnacovo M, Antonelli M, Biassoni V, et al. Retrospective analysis on the consistency of MRI features with histological and molecular markers in diffuse intrinsic pontine glioma (DIPG). *Childs Nerv Syst.* 2020; 36(4):697-704.

53. Poussaint TY. Magnetic Resonance Imaging of Pediatric Brain Tumors: State of the Art. *Topics in Magnetic Resonance Imaging.* 2001; 12(6):411-433.

54. Leach JL, Roebker J, Schafer A, et al. MR imaging features of diffuse intrinsic pontine glioma and relationship to overall survival: report from the International DIPG Registry. *Neuro Oncol.* 2020; 22(11):1647-1657.

55. Chauhan RS, Kulanthaivelu K, Kathrani N, et al. Prediction of H3K27M mutation status of diffuse midline gliomas using MRI features. *J Neuroimaging.* 2021; 31(6):1201-1210.

56. Mandell LR, Kadota R, Freeman C, et al. There is no role for hyperfractionated radiotherapy in the management of children with newly diagnosed diffuse intrinsic brainstem tumors: results of a Pediatric Oncology Group phase III trial comparing conventional vs. hyperfractionated radiotherapy. *International journal of radiation oncology, biology, physics.* 1999; 43(5):959-964.

57. Negretti L, Bouchireb K, Levy-Piedbois C, et al. Hypofractionated radiotherapy in the treatment of diffuse intrinsic pontine glioma in children: a single institution's experience. *J Neurooncol.* 2011; 104(3):773-777.

58. Zaghloul MS, Eldebawy E, Ahmed S, et al. Hypofractionated conformal radiotherapy for pediatric diffuse intrinsic pontine glioma (DIPG): a randomized controlled trial. *Radiotherapy and oncology : journal of the European Society for Therapeutic Radiology and Oncology.* 2014; 111(1):35-40.

59. Viani GA, Gouveia AG, Arcidiacono F, et al. Efficacy and safety of hypofractionated radiotherapy versus conventional fractionated radiotherapy in diffuse intrinsic pontine glioma: A systematic review and meta-analysis. *Reports of practical oncology and radiotherapy : journal of Greatpoland Cancer Center in Poznan and Polish Society of Radiation Oncology.* 2024; 29(3):309-317.

60. Zamora PL, Miller SR, Kovoor JJ. Single institution experience in re-irradiation of biopsy-proven diffuse intrinsic pontine gliomas. *Childs Nerv Syst.* 2021; 37(8):2539-2543.

61. Roujeau T, Machado G, Garnett MR, et al. Stereotactic biopsy of diffuse pontine lesions in children. *J Neurosurg.* 2007; 107(1 Suppl):1-4.

62. Leach PA, Estlin EJ, Coope DJ, Thorne JA, Kamaly-Asl ID. Diffuse brainstem gliomas in children: should we or shouldn't we biopsy? *British journal of neurosurgery.* 2008; 22(5):619-624.

63. Waters JD, Gonda DD, Reddy H, Kasper EM, Warnke PC, Chen CC. Diagnostic yield of stereotactic needle-biopsies of sub-cubic centimeter intracranial lesions. *Surgical neurology international.* 2013; 4(Suppl 3):S176-181.

64. Cordone I, Masi S, Carosi M, et al. Brain stereotactic biopsy flow cytometry for central nervous system lymphoma characterization: advantages and pitfalls. *J Exp Clin Cancer Res.* 2016; 35(1):128.

65. Yoshimura J, Onda K, Tanaka R, Takahashi H. Clinicopathological study of diffuse type brainstem gliomas: analysis of 40 autopsy cases. *Neurologia medico-chirurgica.* 2003; 43(8):375-382; discussion 382.

66. Toll SA, Tran HN, Cotter J, et al. Sustained response of three pediatric BRAF(V600E) mutated high-grade gliomas to combined BRAF and MEK inhibitor therapy. *Oncotarget.* 2019; 10(4):551-557.

67. De Mattos-Arruda L, Mayor R, Ng CKY, et al. Cerebrospinal fluid-derived circulating tumour DNA better represents the genomic alterations of brain tumours than plasma. *Nat Commun.* 2015; 6:8839.

68. Nikanjam M, Kato S, Kurzrock R. Liquid biopsy: current technology and clinical applications. *Journal of hematology & oncology.* 2022; 15(1):131.

69. Abramson DH. Cell Free DNA (cfDNA) in the Blood of Retinoblastoma Patients The Robert M. Ellsworth Lecture. *Ophthalmic genetics.* 2022; 43(6):731-735.

70. Valpione S, Campana L. Detection of circulating tumor DNA (ctDNA) by digital droplet polymerase chain reaction (dd-PCR) in liquid biopsies. *Methods in enzymology.* 2019; 629:1-15.

71. Postel M, Roosen A, Laurent-Puig P, Taly V, Wang-Renault SF. Droplet-based digital PCR and next generation sequencing for monitoring circulating tumor DNA: a cancer diagnostic perspective. *Expert review of molecular diagnostics.* 2018; 18(1):7-17.

72. Bettegowda C, Sausen M, Leary RJ, et al. Detection of Circulating Tumor DNA in Early- and Late-Stage Human Malignancies. *Science translational medicine.* 2014; 6(224):224ra224-224ra224.

73. Pan Y, Long W, Liu Q. Current Advances and Future Perspectives of Cerebrospinal Fluid Biopsy in Midline Brain Malignancies. *Current Treatment Options in Oncology.* 2019; 20(12):88.

74. Izquierdo E, Proszek P, Pericoli G, et al. Droplet digital PCR-based detection of circulating tumor DNA from pediatric high grade and diffuse midline glioma patients. *Neurooncol Adv.* 2021; 3(1):vdab013.

75. Pan C, Diplas BH, Chen X, et al. Molecular profiling of tumors of the brainstem by sequencing of CSF-derived circulating tumor DNA. *Acta Neuropathol.* 2019; 137(2):297-306.

76. Stallard S, Savelieff MG, Wierzbicki K, et al. CSF *H3F3A* K27M circulating tumor DNA copy number quantifies tumor growth and in vitro treatment response. *Acta Neuropathol Commun.* 2018; 6(1):80.

77. Panditharatna E, Kilburn LB, Aboian MS, et al. Clinically Relevant and Minimally Invasive Tumor Surveillance of Pediatric Diffuse Midline Gliomas Using Patient-Derived Liquid Biopsy. *Clin Cancer Res.* 2018; 24(23):5850-5859.

78. Cantor E, Wierzbicki K, Tarapore RS, et al. Serial H3K27M cell-free tumor DNA (cf-tDNA) tracking predicts ONC201 treatment response and progression in diffuse midline glioma. *Neuro Oncol.* 2022; 24(8):1366-1374.

79. Monje M, Mitra SS, Freret ME, et al. Hedgehog-responsive candidate cell of origin for diffuse intrinsic pontine glioma. *Proc Natl Acad Sci U S A.* 2011; 108(11):4453-4458.

80. Truffaux N, Philippe C, Paulsson J, et al. Preclinical evaluation of dasatinib alone and in combination with cabozantinib for the treatment of diffuse intrinsic pontine glioma. *Neuro Oncol.* 2015; 17(7):953-964.

81. Hashizume R, Smirnov I, Liu S, et al. Characterization of a diffuse intrinsic pontine glioma cell line: implications for future investigations and treatment. *J Neurooncol.* 2012; 110(3):305-313.

82. Misuraca KL, Cordero FJ, Becher OJ. Pre-Clinical Models of Diffuse Intrinsic Pontine Glioma. *Front Oncol.* 2015; 5:172.

83. Hashizume R, Ozawa T, Dinca EB, et al. A human brainstem glioma xenograft model enabled for bioluminescence imaging. *J Neurooncol.* 2010; 96(2):151-159.

84. Caretti V, Zondervan I, Meijer DH, et al. Monitoring of tumor growth and post-irradiation recurrence in a diffuse intrinsic pontine glioma mouse model. *Brain Pathol.* 2011; 21(4):441-451.

85. Xi G, Rajaram V, Mania-Farnell B, et al. Efficacy of vincristine administered via convection-enhanced delivery in a rodent brainstem tumor model documented by bioluminescence imaging. *Childs Nerv Syst.* 2012; 28(4):565-574.

86. Grasso CS, Tang Y, Truffaux N, et al. Functionally defined therapeutic targets in diffuse intrinsic pontine glioma. *Nature medicine.* 2015; 21(6):555-559.

87. Taylor KR, Mackay A, Truffaux N, et al. Recurrent activating ACVR1 mutations in diffuse intrinsic pontine glioma. *Nat Genet.* 2014; 46(5):457-461.

88. Balakrishnan I, Danis E, Pierce A, et al. Senescence Induced by BMI1 Inhibition Is a Therapeutic Vulnerability in H3K27M-Mutant DIPG. *Cell Rep.* 2020; 33(3):108286.

89. Carvalho D, Taylor KR, Olaciregui NG, et al. ALK2 inhibitors display beneficial effects in preclinical models of ACVR1 mutant diffuse intrinsic pontine glioma. *Commun Biol.* 2019; 2:156.

90. Chheda ZS, Kohanbash G, Okada K, et al. Novel and shared neoantigen derived from histone 3 variant H3.3K27M mutation for glioma T cell therapy. *J Exp Med.* 2018; 215(1):141-157.

91. Cockle JV, Bruning-Richardson A, Scott KJ, et al. Oncolytic Herpes Simplex Virus Inhibits Pediatric Brain Tumor Migration and Invasion. *Mol Ther Oncolytics.* 2017; 5:75-86.

92. Cockle JV, Picton S, Levesley J, et al. Cell migration in paediatric glioma; characterisation and potential therapeutic targeting. *Br J Cancer.* 2015; 112(4):693-703.

93. Fons NR, Sundaram RK, Breuer GA, et al. PPM1D mutations silence NAPRT gene expression and confer NAMPT inhibitor sensitivity in glioma. *Nat Commun.* 2019; 10(1):3790.

94. Hennika T, Hu G, Olaciregui NG, et al. Pre-Clinical Study of Panobinostat in Xenograft and Genetically Engineered Murine Diffuse Intrinsic Pontine Glioma Models. *PLoS One.* 2017; 12(1):e0169485.

95. Jansen MH, Lagerweij T, Sewing AC, et al. Bevacizumab Targeting Diffuse Intrinsic Pontine Glioma: Results of 89Zr-Bevacizumab PET Imaging in Brain Tumor Models. *Mol Cancer Ther.* 2016; 15(9):2166-2174.

96. Katagi H, Louis N, Unruh D, et al. Radiosensitization by Histone H3 Demethylase Inhibition in Diffuse Intrinsic Pontine Glioma. *Clinical cancer research : an official journal of the American Association for Cancer Research.* 2019; 25(18):5572-5583.

97. Koncar RF, Dey BR, Stanton AJ, et al. Identification of Novel RAS Signaling Therapeutic Vulnerabilities in Diffuse Intrinsic Pontine Gliomas. *Cancer research.* 2019; 79(16):4026-4041.

98. Meel MH, de Gooijer MC, Guillen Navarro M, et al. MELK Inhibition in Diffuse Intrinsic Pontine Glioma. *Clinical cancer research : an official journal of the American Association for Cancer Research.* 2018; 24(22):5645-5657.

99. Mohammad F, Weissmann S, Leblanc B, et al. EZH2 is a potential therapeutic target for H3K27M-mutant pediatric gliomas. *Nat Med.* 2017; 23(4):483-492.

100. Sewing ACP, Lagerweij T, van Vuurden DG, et al. Preclinical evaluation of convection-enhanced delivery of liposomal doxorubicin to treat pediatric diffuse intrinsic pontine glioma and thalamic high-grade glioma. *J Neurosurg Pediatr.* 2017; 19(5):518-530.

101. Thomas L, Smith N, Saunders D, et al. OKlahoma Nitrone-007: novel treatment for diffuse intrinsic pontine glioma. *Journal of translational medicine.* 2020; 18(1):424.

102. Vinci M, Burford A, Molinari V, et al. Functional diversity and cooperativity between subclonal populations of pediatric glioblastoma and diffuse intrinsic pontine glioma cells. *Nature medicine.* 2018; 24(8):1204-1215.

103. Wiese M, Hamdan FH, Kubiak K, et al. Combined treatment with CBP and BET inhibitors reverses inadvertent activation of detrimental super enhancer programs in DIPG cells. *Cell Death Dis.* 2020; 11(8):673.

104. Przystal JM, Waramit S, Pranjol MZI, et al. Efficacy of systemic temozolomide-activated phage-targeted gene therapy in human glioblastoma. *EMBO Mol Med.* 2019; 11(4).

105. Chauhan PS, Kumarasamy M, Carcaboso AM, Sosnik A, Danino D. Multifunctional silica-coated mixed polymeric micelles for integrin-targeted therapy of pediatric patient-derived glioblastoma. *Mater Sci Eng C Mater Biol Appl.* 2021; 128:112261.

106. Tsoli M, Shen H, Mayoh C, et al. International experience in the development of patient-derived xenograft models of diffuse intrinsic pontine glioma. *J Neurooncol.* 2019; 141(2):253-263.

107. Nunez FM, Gauss JC, Mendez FM, Haase S, Lowenstein PR, Castro MG. Genetically Engineered Mouse Model of Brainstem High-Grade Glioma. *STAR Protoc.* 2020; 1(3):100165.

108. Weidenhammer LB, Liu HQ, Luo L, et al. Inducing primary brainstem gliomas in genetically engineered mice using RCAS/TVA retroviruses and Cre/loxP recombination. *STAR Protoc.* 2023; 4(1):102094.

109. Misuraca KL, Hu G, Barton KL, Chung A, Becher OJ. A Novel Mouse Model of Diffuse Intrinsic Pontine Glioma Initiated in Pax3-Expressing Cells. *Neoplasia (New York, N.Y.).* 2016; 18(1):60-70.

110. Patel SK, Hartley RM, Wei X, et al. Generation of diffuse intrinsic pontine glioma mouse models by brainstem-targeted in utero electroporation. *Neuro Oncol.* 2020; 22(3):381-392.

111. Funato K, Major T, Lewis PW, Allis CD, Tabar V. Use of human embryonic stem cells to model pediatric gliomas with H3.3K27M histone mutation. *Science (New York, N.Y.).* 2014; 346(6216):1529-1533.

112. Grabovska Y, Mackay A, O'Hare P, et al. Pediatric pan-central nervous system tumor analysis of immune-cell infiltration identifies correlates of antitumor immunity. *Nat Commun.* 2020; 11(1):4324.

113. Lieberman NAP, DeGolier K, Kovar HM, et al. Characterization of the immune microenvironment of diffuse intrinsic pontine glioma: implications for development of immunotherapy. *Neuro Oncol.* 2019; 21(1):83-94.

114. Lenzen A, Lauing KL, Zhai L, et al. IMMU-01. NOVEL RNA-TARGETING STRATEGY FOR TREATING T CELL-DRIVEN IMMUNOSUPPRESSION IN HUMAN DIFFUSE INTRINSIC PONTINE GLIOMA. *Neuro-Oncology.* 2019; 21(Supplement_2):ii92-ii93.

115. Chen Z, Peng P, Zhang X, Mania-Farnell B, Xi G, Wan F. Advanced Pediatric Diffuse Pontine Glioma Murine Models Pave the Way towards Precision Medicine. *Cancers (Basel).* 2021; 13(5).

116. Prabhu VV, Morrow S, Rahman Kawakibi A, et al. ONC201 and imipridones: Anti-cancer compounds with clinical efficacy. *Neoplasia (New York, N.Y.).* 2020; 22(12):725-744.

117. Perrone MG, Ruggiero A, Centonze A, Carrieri A, Ferorelli S, Scilimati A. Diffuse Intrinsic Pontine Glioma (DIPG): Breakthrough and Clinical Perspective. *Curr Med Chem.* 2021; 28(17):3287-3317.

118. Allen JE, Kline CL, Prabhu VV, et al. Discovery and clinical introduction of first-in-class imipridone ONC201. *Oncotarget.* 2016; 7(45):74380-74392.

119. Allen JE, Krigsfeld G, Mayes PA, et al. Dual inactivation of Akt and ERK by TIC10 signals Foxo3a nuclear translocation, TRAIL gene induction, and potent antitumor effects. *Science translational medicine.* 2013; 5(171):171ra117.

120. Ishida CT, Zhang Y, Bianchetti E, et al. Metabolic Reprogramming by Dual AKT/ERK Inhibition through Imipridones Elicits Unique Vulnerabilities in Glioblastoma. *Clin Cancer Res.* 2018; 24(21):5392-5406.

121. Przystal JM, Cianciolo Cosentino C, Yadavilli S, et al. Imipridones affect tumor bioenergetics and promote cell lineage differentiation in diffuse midline gliomas. *Neuro Oncol.* 2022; 24(9):1438-1451.

122. Borsuk R, Zhou L, Chang WI, et al. Potent preclinical sensitivity to imipridone-based combination therapies in oncohistone H3K27M-mutant diffuse intrinsic pontine glioma is associated with induction of the integrated stress response, TRAIL death receptor DR5, reduced ClpX and apoptosis. *American journal of cancer research.* 2021; 11(9):4607-4623.

123. Duchatel RJ, Mannan A, Woldu AS, et al. Preclinical and clinical evaluation of German-sourced ONC201 for the treatment of H3K27M-mutant diffuse intrinsic pontine glioma. *Neurooncol Adv.* 2021; 3(1):vdab169.

124. Hall MD, Odia Y, Allen JE, et al. First clinical experience with DRD2/3 antagonist ONC201 in H3 K27M-mutant pediatric diffuse intrinsic pontine glioma: a case report. *J Neurosurg Pediatr.* 2019; 23(6):719-725.

125. Jackson ER, Duchatel RJ, Staudt DE, et al. ONC201 in combination with paxalisib for the treatment of H3K27-altered diffuse midline glioma. *Cancer research.* 2023.

126. Venneti S, Kawakibi AR, Ji S, et al. Clinical Efficacy of ONC201 in H3K27M-Mutant Diffuse Midline Gliomas Is Driven by Disruption of Integrated Metabolic and Epigenetic Pathways. *Cancer Discov.* 2023; 13(11):2370-2393.

127. Chung C, Sweha SR, Pratt D, et al. Integrated Metabolic and Epigenomic Reprograming by H3K27M Mutations in Diffuse Intrinsic Pontine Gliomas. *Cancer Cell.* 2020; 38(3):334-349.e339.

128. He Y, Sun MM, Zhang GG, et al. Targeting PI3K/Akt signal transduction for cancer therapy. *Signal Transduct Target Ther.* 2021; 6(1):425.

129. Arafeh R, Samuels Y. PIK3CA in cancer: The past 30 years. *Semin Cancer Biol.* 2019; 59:36-49.

130. Mayer IA, Arteaga CL. The PI3K/AKT Pathway as a Target for Cancer Treatment. *Annual review of medicine.* 2016; 67:11-28.

131. Haglund K, Rusten TE, Stenmark H. Aberrant receptor signaling and trafficking as mechanisms in oncogenesis. *Critical reviews in oncogenesis.* 2007; 13(1):39-74.

132. Vivanco I, Sawyers CL. The phosphatidylinositol 3-Kinase AKT pathway in human cancer. *Nat Rev Cancer.* 2002; 2(7):489-501.

133. Ikenoue T, Inoki K, Yang Q, Zhou X, Guan KL. Essential function of TORC2 in PKC and Akt turn motif phosphorylation, maturation and signalling. *The EMBO journal.* 2008; 27(14):1919-1931.

134. Manning BD, Toker A. AKT/PKB Signaling: Navigating the Network. *Cell.* 2017; 169(3):381-405.

135. Duchatel RJ, Jackson ER, Alvaro F, Nixon B, Hondermarck H, Dun MD. Signal Transduction in Diffuse Intrinsic Pontine Glioma. *Proteomics.* 2019; 19(21-22):e1800479.

136. Blake JF, Xu R, Bencsik JR, et al. Discovery and preclinical pharmacology of a selective ATP-competitive Akt inhibitor (GDC-0068) for the treatment of human tumors. *Journal of medicinal chemistry.* 2012; 55(18):8110-8127.

137. Lin J, Sampath D, Nannini MA, et al. Targeting activated Akt with GDC-0068, a novel selective Akt inhibitor that is efficacious in multiple tumor models. *Clin Cancer Res.* 2013; 19(7):1760-1772.

138. Saura C, Roda D, Roselló S, et al. A First-in-Human Phase I Study of the ATP-Competitive AKT Inhibitor Ipatasertib Demonstrates Robust and Safe Targeting of AKT in Patients with Solid Tumors. *Cancer Discov.* 2017; 7(1):102-113.

139. Ippen FM, Grosch JK, Subramanian M, et al. Targeting the PI3K/Akt/mTOR pathway with the pan-Akt inhibitor GDC-0068 in PIK3CA-mutant breast cancer brain metastases. *Neuro Oncol.* 2019; 21(11):1401-1411.

140. Kim SB, Dent R, Im SA, et al. Ipatasertib plus paclitaxel versus placebo plus paclitaxel as first-line therapy for metastatic triple-negative breast cancer (LOTUS): a multicentre, randomised, double-blind, placebo-controlled, phase 2 trial. *The Lancet. Oncology.* 2017; 18(10):1360-1372.

141. Slotkin EK, Diolaiti D, Shukla NN, et al. Patient-Driven Discovery, Therapeutic Targeting, and Post-Clinical Validation of a Novel AKT1 Fusion-Driven Cancer. *Cancer Discov.* 2019; 9(5):605-616.

142. Li H, Prever L, Hirsch E, Gulluni F. Targeting PI3K/AKT/mTOR Signaling Pathway in Breast Cancer. *Cancers (Basel).* 2021; 13(14).

143. Mukohara T. PI3K mutations in breast cancer: prognostic and therapeutic implications. *Breast cancer (Dove Medical Press).* 2015; 7:111-123.

144. Akinleye A, Avvaru P, Furqan M, Song Y, Liu D. Phosphatidylinositol 3-kinase (PI3K) inhibitors as cancer therapeutics. *Journal of hematology & oncology.* 2013; 6(1):88.

145. Massacesi C, Di Tomaso E, Urban P, et al. PI3K inhibitors as new cancer therapeutics: implications for clinical trial design. *OncoTargets and therapy.* 2016; 9:203-210.

146. Eckerdt FD, Bell JB, Gonzalez C, et al. Combined PI3Kα-mTOR Targeting of Glioma Stem Cells. *Sci Rep.* 2020; 10(1):21873.

147. Salphati L, Shahidi-Latham S, Quiason C, et al. Distribution of the phosphatidylinositol 3-kinase inhibitors Pictilisib (GDC-0941) and GNE-317 in U87 and GS2 intracranial glioblastoma models-assessment by matrix-assisted laser desorption ionization imaging. *Drug metabolism and disposition: the biological fate of chemicals.* 2014; 42(7):1110-1116.

148. Wen PY, Cloughesy TF, Olivero AG, et al. First-in-Human Phase I Study to Evaluate the Brain-Penetrant PI3K/mTOR Inhibitor GDC-0084 in Patients with Progressive or Recurrent High-Grade Glioma. *Clin Cancer Res.* 2020; 26(8):1820-1828.

149. Hanan EJ, Braun MG, Heald RA, et al. Discovery of GDC-0077 (Inavolisib), a Highly Selective Inhibitor and Degrader of Mutant PI3Kα. *Journal of medicinal chemistry.* 2022; 65(24):16589-16621.

150. Hong R, Edgar K, Song K, et al. Abstract PD4-14: GDC-0077 is a selective PI3Kalpha inhibitor that demonstrates robust efficacy in PIK3CA mutant breast cancer models as a single agent and in combination with standard of care therapies. *Cancer research.* 2018; 78(4_Supplement):PD4-14-PD14-14.

151. Song KW, Edgar KA, Hanan EJ, et al. RTK-Dependent Inducible Degradation of Mutant PI3Kalpha Drives GDC-0077 (Inavolisib) Efficacy. *Cancer Discov.* 2022; 12(1):204-219.

152. Jones LH. Small-Molecule Kinase Downregulators. *Cell chemical biology.* 2018; 25(1):30-35.

153. Glaviano A, Foo ASC, Lam HY, et al. PI3K/AKT/mTOR signaling transduction pathway and targeted therapies in cancer. *Molecular cancer.* 2023; 22(1):138.

154. Mendoza MC, Er EE, Blenis J. The Ras-ERK and PI3K-mTOR pathways: cross-talk and compensation. *Trends in biochemical sciences.* 2011; 36(6):320-328.

155. Cuesta C, Arévalo-Alameda C, Castellano E. The Importance of Being PI3K in the RAS Signaling Network. *Genes (Basel).* 2021; 12(7).

156. Tóthová Z, Šemeláková M, Solárová Z, Tomc J, Debeljak N, Solár P. The Role of PI3K/AKT and MAPK Signaling Pathways in Erythropoietin Signalization. *Int J Mol Sci.* 2021; 22(14).

157. Huang WC, Hung MC. Induction of Akt activity by chemotherapy confers acquired resistance. *Journal of the Formosan Medical Association = Taiwan yi zhi.* 2009; 108(3):180-194.

158. Cuesta C, Arévalo-Alameda C, Castellano E. The Importance of Being PI3K in the RAS Signaling Network. *Genes.* 2021; 12(7):1094.

159. Li Y, Dong Q, Cui Y. Synergistic inhibition of MEK and reciprocal feedback networks for targeted intervention in malignancy. *Cancer biology & medicine.* 2019; 16(3):415-434.

160. Perreault S, Larouche V, Tabori U, et al. A phase 2 study of trametinib for patients with pediatric glioma or plexiform neurofibroma with refractory tumor and activation of the MAPK/ERK pathway: TRAM-01. *BMC Cancer.* 2019; 19(1):1250.

161. He C, Xu K, Zhu X, et al. Patient-derived models recapitulate heterogeneity of molecular signatures and drug response in pediatric high-grade glioma. *Nature Communications.* 2021; 12(1):4089.

162. Wu YL, Maachani UB, Schweitzer M, et al. Dual Inhibition of PI3K/AKT and MEK/ERK Pathways Induces Synergistic Antitumor Effects in Diffuse Intrinsic Pontine Glioma Cells. *Translational oncology.* 2017; 10(2):221-228.

163. Chang R, Tosi U, Voronina J, et al. Combined targeting of PI3K and MEK effector pathways via CED for DIPG therapy. *Neurooncol Adv.* 2019; 1(1):vdz004.

164. Vicente-Garcés C, Esperanza-Cebollada E, Montesdeoca S, et al. Technical Validation and Clinical Utility of an NGS Targeted Panel to Improve Molecular Characterization of Pediatric Acute Leukemia. *Frontiers in molecular biosciences.* 2022; 9:854098.

165. Li D, Bonner ER, Wierzbicki K, et al. Standardization of the liquid biopsy for pediatric diffuse midline glioma using ddPCR. *Sci Rep.* 2021; 11(1):5098.

166. Jackson JB, Choi DS, Luketich JD, Pennathur A, Stahlberg A, Godfrey TE. Multiplex Preamplification of Serum DNA to Facilitate Reliable Detection of Extremely Rare Cancer Mutations in Circulating DNA by Digital PCR. *J Mol Diagn.* 2016; 18(2):235-243.

167. Carvalho DM, Richardson PJ, Olaciregui N, et al. Repurposing Vandetanib plus Everolimus for the Treatment of ACVR1-Mutant Diffuse Intrinsic Pontine Glioma. *Cancer Discov.* 2022; 12(2):416-431.

168. Zhang L, Nesvick CL, Day CA, et al. STAT3 is a biologically relevant therapeutic target in H3K27M-mutant diffuse midline glioma. *Neuro Oncol.* 2022; 24(10):1700-1711.

169. Liu L, Duff K. A technique for serial collection of cerebrospinal fluid from the cisterna magna in mouse. *J Vis Exp.* 2008(21).

170. Smil D, Wong JF, Williams EP, et al. Leveraging an Open Science Drug Discovery Model to Develop CNS-Penetrant ALK2 Inhibitors for the Treatment of Diffuse Intrinsic Pontine Glioma. *Journal of medicinal chemistry.* 2020; 63(17):10061-10085.

171. Ensan D, Smil D, Zepeda-Velázquez CA, et al. Targeting ALK2: An Open Science Approach to Developing Therapeutics for the Treatment of Diffuse Intrinsic Pontine Glioma. *Journal of medicinal chemistry.* 2020; 63(9):4978-4996.

172. Taylor KR, Mackay A, Truffaux N, et al. Recurrent activating ACVR1 mutations in diffuse intrinsic pontine glioma. *Nat Genet.* 2014; 46(5):457-461.

173. Werbrouck C, Evangelista CCS, Lobón-Iglesias MJ, et al. TP53 Pathway Alterations Drive Radioresistance in Diffuse Intrinsic Pontine Gliomas (DIPG). *Clin Cancer Res.* 2019; 25(22):6788-6800.

174. Wu G, Diaz AK, Paugh BS, et al. The genomic landscape of diffuse intrinsic pontine glioma and pediatric non-brainstem high-grade glioma. *Nat Genet.* 2014; 46(5):444-450.

175. Nikbakht H, Panditharatna E, Mikael LG, et al. Spatial and temporal homogeneity of driver mutations in diffuse intrinsic pontine glioma. *Nat Commun.* 2016; 7:11185.

176. Schwartzentruber J, Korshunov A, Liu X-Y, et al. Driver mutations in histone H3.3 and chromatin remodelling genes in paediatric glioblastoma. *Nature.* 2012; 482(7384):226-231.

177. Gatfield D, Unterholzner L, Ciccarelli FD, Bork P, Izaurralde E. Nonsense-mediated mRNA decay in Drosophila: at the intersection of the yeast and mammalian pathways. *The EMBO journal.* 2003; 22(15):3960-3970.

178. Koschmann C, Zamler D, MacKay A, et al. Characterizing and targeting PDGFRA alterations in pediatric high-grade glioma. *Oncotarget.* 2016; 7(40):65696-65706.

179. Bielski CM, Donoghue MTA, Gadiya M, et al. Widespread Selection for Oncogenic Mutant Allele Imbalance in Cancer. *Cancer Cell.* 2018; 34(5):852-862.e854.

180. Yu CC, Qiu W, Juang CS, Mansukhani MM, Halmos B, Su GH. Mutant allele specific imbalance in oncogenes with copy number alterations: Occurrence, mechanisms, and potential clinical implications. *Cancer letters.* 2017; 384:86-93.

181. Stieglitz E, Troup CB, Gelston LC, et al. Subclonal mutations in SETBP1 confer a poor prognosis in juvenile myelomonocytic leukemia. *Blood.* 2015; 125(3):516-524.

182. Odia Y, Koschmann C, Vitanza NA, et al. Safety and pharmacokinetics of ONC201 (dordaviprone) administered two consecutive days per week in pediatric patients with H3 K27M-mutant glioma. *Neuro Oncol.* 2024; 26(Supplement_2):S155-s164.

183. Brandão M, Caparica R, Eiger D, de Azambuja E. Biomarkers of response and resistance to PI3K inhibitors in estrogen receptor-positive breast cancer patients and combination therapies involving PI3K inhibitors. *Annals of oncology : official journal of the European Society for Medical Oncology.* 2019; 30(Suppl_10):x27-x42.

184. Abramson VG, Oliveira M, Cervantes A, et al. A phase Ib, open-label, dose-escalation study of the safety and pharmacology of taselisib (GDC-0032) in combination with either docetaxel or paclitaxel in patients with HER2-negative, locally advanced, or metastatic breast cancer. *Breast cancer research and treatment.* 2019; 178(1):121-133.

185. Stulpinas A, Sereika M, Vitkeviciene A, Imbrasaite A, Krestnikova N, Kalvelyte AV. Crosstalk between protein kinases AKT and ERK1/2 in human lung tumor-derived cell models. *Front Oncol.* 2022; 12:1045521.

186. Li Q, Li Z, Luo T, Shi H. Targeting the PI3K/AKT/mTOR and RAF/MEK/ERK pathways for cancer therapy. *Molecular Biomedicine.* 2022; 3(1):47.

187. Koncar RF, Dey BR, Stanton A-CJ, et al. Identification of Novel RAS Signaling Therapeutic Vulnerabilities in Diffuse Intrinsic Pontine Gliomas. *Cancer research.* 2019; 79(16):4026-4041.

188. Hyun T, Yam A, Pece S, et al. Loss of PTEN expression leading to high Akt activation in human multiple myelomas. *Blood.* 2000; 96(10):3560-3568.

189. Poduri A, Evrony GD, Cai X, et al. Somatic activation of AKT3 causes hemispheric developmental brain malformations. *Neuron.* 2012; 74(1):41-48.

190. Panwar V, Singh A, Bhatt M, et al. Multifaceted role of mTOR (mammalian target of rapamycin) signaling pathway in human health and disease. *Signal Transduction and Targeted Therapy.* 2023; 8(1):375.

191. Carcaboso AM, Elmeliegy MA, Shen J, et al. Tyrosine kinase inhibitor gefitinib enhances topotecan penetration of gliomas. *Cancer research.* 2010; 70(11):4499-4508.

192. Hamm A, Krott N, Breibach I, Blindt R, Bosserhoff AK. Efficient transfection method for primary cells. *Tissue engineering.* 2002; 8(2):235-245.

193. Gresch O, Altrogge L. Transfection of Difficult-to-Transfect Primary Mammalian Cells. In: Hartley JL, ed. *Protein Expression in Mammalian Cells: Methods and Protocols*. Totowa, NJ: Humana Press; 2012:65-74.

194. Feys L, Descamps B, Vanhove C, et al. Quantitative and Functional Requirements for Bioluminescent Cancer Models. *In vivo (Athens, Greece).* 2016; 30(1):1-11.

195. Koessinger AL, Koessinger D, Stevenson K, et al. Quantitative in vivo bioluminescence imaging of orthotopic patient-derived glioblastoma xenografts. *Sci Rep.* 2020; 10(1):15361.

196. Cobb DA, de Rossi J, Liu L, An E, Lee DW. Targeting of the alpha(v) beta(3) integrin complex by CAR-T cells leads to rapid regression of diffuse intrinsic pontine glioma and glioblastoma. *J Immunother Cancer.* 2022; 10(2).

197. de Billy E, Pellegrino M, Orlando D, et al. Dual IGF1R/IR inhibitors in combination with GD2-CAR T-cells display a potent anti-tumor activity in diffuse midline glioma H3K27M-mutant. *Neuro Oncol.* 2022; 24(7):1150-1163.

198. Zuo P, Li Y, He C, et al. Anti-tumor efficacy of anti-GD2 CAR NK-92 cells in diffuse intrinsic pontine gliomas. *Front Immunol.* 2023; 14:1145706.

199. Jost SC, Collins L, Travers S, Piwnica-Worms D, Garbow JR. Measuring brain tumor growth: combined bioluminescence imaging-magnetic resonance imaging strategy. *Molecular imaging.* 2009; 8(5):245-253.

200. Shan L, Wang S, Korotcov A, Sridhar R, Wang PC. Bioluminescent animal models of human breast cancer for tumor biomass evaluation and metastasis detection. *Ethnicity & disease.* 2008; 18(2 Suppl 2):S2-65-69.

201. Jang SJ, Kang JH, Kim KI, et al. Application of bioluminescence imaging to therapeutic intervention of herpes simplex virus type I – Thymidine kinase/ganciclovir in glioma. *Cancer letters.* 2010; 297(1):84-90.

202. Chevaleyre C, Kereselidze D, Caillé F, et al. TSPO PET Imaging as a Potent Non-Invasive Biomarker for Diffuse Intrinsic Pontine Glioma in a Patient-Derived Orthotopic Rat Model. *Int J Mol Sci.* 2022; 23(20).

203. van Hooren L, Vaccaro A, Ramachandran M, et al. Agonistic CD40 therapy induces tertiary lymphoid structures but impairs responses to checkpoint blockade in glioma. *Nat Commun.* 2021; 12(1):4127.

204. Madhavan K, Balakrishnan I, Lakshmanachetty S, et al. Venetoclax Cooperates with Ionizing Radiation to Attenuate Diffuse Midline Glioma Tumor Growth. *Clin Cancer Res.* 2022; 28(11):2409-2424.

205. Brown EJ, Balaguer-Lluna L, Cribbs AP, et al. PRMT5 inhibition shows in vitro efficacy against H3K27M-altered diffuse midline glioma, but does not extend survival in vivo. *Sci Rep.* 2024; 14(1):328.

206. t Hart E, Bianco J, Besse HC, et al. Towards Standardisation of a Diffuse Midline Glioma Patient-Derived Xenograft Mouse Model Based on Suspension Matrices for Preclinical Research. *Biomedicines.* 2023; 11(2).

207. Balakrishnan I, Danis E, Pierce A, et al. Senescence Induced by BMI1 Inhibition Is a Therapeutic Vulnerability in H3K27M-Mutant DIPG. *Cell Reports.* 2020; 33(3):108286.

208. Kim JY, Jo Y, Oh HK, Kim EH. Sorafenib increases tumor treating fields-induced cell death in glioblastoma by inhibiting STAT3. *American journal of cancer research.* 2020; 10(10):3475-3486.

209. Yin L, Li H, Liu W, et al. A highly potent CDK4/6 inhibitor was rationally designed to overcome blood brain barrier in gliobastoma therapy. *European Journal of Medicinal Chemistry.* 2018; 144:1-28.

210. de la Nava D, Ausejo-Mauleon I, Laspidea V, et al. The oncolytic adenovirus Delta-24-RGD in combination with ONC201 induces a potent antitumor response in pediatric high-grade and diffuse midline glioma models. *Neuro Oncol.* 2024.

211. Duchatel RJ, Jackson ER, Parackal SG, et al. PI3K/mTOR is a therapeutically targetable genetic dependency in diffuse intrinsic pontine glioma. *The Journal of clinical investigation.* 2024; 134(6).

212. Huang TY, Piunti A, Lulla RR, et al. Detection of Histone H3 mutations in cerebrospinal fluid-derived tumor DNA from children with diffuse midline glioma. *Acta Neuropathol Commun.* 2017; 5(1):28.

213. Bonner ER, Bornhorst M, Packer RJ, Nazarian J. Liquid biopsy for pediatric central nervous system tumors. *NPJ Precis Oncol.* 2018; 2:29.

214. Cohen NR, Phipps K, Harding B, Jacques TS. Is CSF cytology a useful diagnostic procedure in staging paediatric CNS tumours? *Cytopathology.* 2009; 20(4):256-260.

215. Martínez-Ricarte F, Mayor R, Martínez-Sáez E, et al. Molecular Diagnosis of Diffuse Gliomas through Sequencing of Cell-Free Circulating Tumor DNA from Cerebrospinal Fluid. *Clinical Cancer Research.* 2018; 24(12):2812-2819.

216. Juratli TA, Stasik S, Zolal A, et al. TERT Promoter Mutation Detection in Cell-Free Tumor-Derived DNA in Patients with IDH Wild-Type Glioblastomas: A Pilot Prospective Study. *Clinical Cancer Research.* 2018; 24(21):5282-5291.

217. Jackson JB, Choi DS, Luketich JD, Pennathur A, Ståhlberg A, Godfrey TE. Multiplex Preamplification of Serum DNA to Facilitate Reliable Detection of Extremely Rare Cancer Mutations in Circulating DNA by Digital PCR. *J Mol Diagn.* 2016; 18(2):235-243.

218. Bettegowda C, Sausen M, Leary RJ, et al. Detection of circulating tumor DNA in early- and late-stage human malignancies. *Science translational medicine.* 2014; 6(224):224ra224.

219. Buzova D, Frohlich J, Zapletalova D, et al. Detection of cell-free histones in the cerebrospinal fluid of pediatric central nervous system malignancies by imaging flow cytometry. *Frontiers in molecular biosciences.* 2023; 10:1254699.

220. Dang DK, Park BH. Circulating tumor DNA: current challenges for clinical utility. *The Journal of clinical investigation.* 2022; 132(12).

221. Stejskal P, Goodarzi H, Srovnal J, Hajdúch M, van 't Veer LJ, Magbanua MJM. Circulating tumor nucleic acids: biology, release mechanisms, and clinical relevance. *Molecular cancer.* 2023; 22(1):15.

222. Martin-Alonso C, Tabrizi S, Xiong K, et al. Priming agents transiently reduce the clearance of cell-free DNA to improve liquid biopsies. *Science (New York, N.Y.).* 2024; 383(6680):eadf2341.

223. Noh JM, Kim YJ, Lee HY, et al. Targeted Liquid Biopsy Using Irradiation to Facilitate the Release of Cell-Free DNA from a Spatially Aimed Tumor Tissue. *Cancer Res Treat.* 2022; 54(1):40-53.

224. Rago C, Huso DL, Diehl F, et al. Serial assessment of human tumor burdens in mice by the analysis of circulating DNA. *Cancer research.* 2007; 67(19):9364-9370.

225. Wei L, Xie L, Wang X, et al. Circulating tumor DNA measurement provides reliable mutation detection in mice with human lung cancer xenografts. *Laboratory investigation; a journal of technical methods and pathology.* 2018; 98(7):935-946.

226. Hayashi M, Chu D, Meyer CF, et al. Highly personalized detection of minimal Ewing sarcoma disease burden from plasma tumor DNA. *Cancer.* 2016; 122(19):3015-3023.

227. Mount CW, Majzner RG, Sundaresh S, et al. Potent antitumor efficacy of anti-GD2 CAR T cells in H3-K27M(+) diffuse midline gliomas. *Nature medicine.* 2018; 24(5):572-579.

228. Irtenkauf SM, Sobiechowski S, Hasselbach LA, et al. Optimization of Glioblastoma Mouse Orthotopic Xenograft Models for Translational Research. *Comparative medicine.* 2017; 67(4):300-314.

229. Yang J, Nie J, Ma X, Wei Y, Peng Y, Wei X. Targeting PI3K in cancer: mechanisms and advances in clinical trials. *Molecular cancer.* 2019; 18(1):26.

230. He Y, Sun MM, Zhang GG, et al. Targeting PI3K/Akt signal transduction for cancer therapy. *Signal Transduction and Targeted Therapy.* 2021; 6(1):425.

231. Lemmon MA, Schlessinger J. Cell signaling by receptor tyrosine kinases. *Cell.* 2010; 141(7):1117-1134.

232. Kim CW, Lee JM, Park SW. Divergent roles of the regulatory subunits of class IA PI3K. *Front Endocrinol (Lausanne).* 2023; 14:1152579.

233. Wang J, Huang TY, Hou Y, et al. Epigenomic landscape and 3D genome structure in pediatric high-grade glioma. *Sci Adv.* 2021; 7(23).

234. Chen CY, Chen J, He L, Stiles BL. PTEN: Tumor Suppressor and Metabolic Regulator. *Front Endocrinol (Lausanne).* 2018; 9:338.

235. Leslie NR, Bennett D, Lindsay YE, Stewart H, Gray A, Downes CP. Redox regulation of PI 3-kinase signalling via inactivation of PTEN. *The EMBO journal.* 2003; 22(20):5501-5510.

236. Morais P, Adachi H, Yu YT. Suppression of Nonsense Mutations by New Emerging Technologies. *Int J Mol Sci.* 2020; 21(12).

237. Cohen S, Kramarski L, Levi S, Deshe N, Ben David O, Arbely E. Nonsense mutation-dependent reinitiation of translation in mammalian cells. *Nucleic Acids Research.* 2019; 47(12):6330-6338.

238. Spinelli L, Lindsay YE, Leslie NR. PTEN inhibitors: An evaluation of current compounds. *Advances in Biological Regulation.* 2015; 57:102-111.

239. Zehorai E, Yao Z, Plotnikov A, Seger R. The subcellular localization of MEK and ERK--a novel nuclear translocation signal (NTS) paves a way to the nucleus. *Mol Cell Endocrinol.* 2010; 314(2):213-220.

240. Jokinen E, Koivunen JP. MEK and PI3K inhibition in solid tumors: rationale and evidence to date. *Therapeutic advances in medical oncology.* 2015; 7(3):170-180.

241. Rajasekhar VK, Viale A, Socci ND, Wiedmann M, Hu X, Holland EC. Oncogenic Ras and Akt signaling contribute to glioblastoma formation by differential recruitment of existing mRNAs to polysomes. *Molecular cell.* 2003; 12(4):889-901.

242. Van Dort ME, Hong H, Wang H, et al. Discovery of Bifunctional Oncogenic Target Inhibitors against Allosteric Mitogen-Activated Protein Kinase (MEK1) and Phosphatidylinositol 3-Kinase (PI3K). *Journal of medicinal chemistry.* 2016; 59(6):2512-2522.

243. Carracedo A, Ma L, Teruya-Feldstein J, et al. Inhibition of mTORC1 leads to MAPK pathway activation through a PI3K-dependent feedback loop in human cancer. *The Journal of clinical investigation.* 2008; 118(9):3065-3074.

244. Izquierdo E, Carvalho DM, Mackay A, et al. DIPG Harbors Alterations Targetable by MEK Inhibitors, with Acquired Resistance Mechanisms Overcome by Combinatorial Inhibition. *Cancer Discov.* 2022; 12(3):712-729.

245. Sudhesh Dev S, Zainal Abidin SA, Farghadani R, Othman I, Naidu R. Receptor Tyrosine Kinases and Their Signaling Pathways as Therapeutic Targets of Curcumin in Cancer. *Frontiers in pharmacology.* 2021; 12:772510.

246. Martin NE, Gerke T, Sinnott JA, et al. Measuring PI3K Activation: Clinicopathologic, Immunohistochemical, and RNA Expression Analysis in Prostate Cancer. *Mol Cancer Res.* 2015; 13(10):1431-1440.

247. Georgescu MM. PTEN Tumor Suppressor Network in PI3K-Akt Pathway Control. *Genes & cancer.* 2010; 1(12):1170-1177.

248. Turner N, Jhaveri K, Kalinsky K, et al. Abstract OT-36-01: Phase III study of GDC-0077 or placebo (pbo) with palbociclib (P) + fulvestrant (F) in patients with PIK3CA-mutant/hormone receptor-positive/HER2-negative locally advanced or metastatic breast cancer (HR+/HER2- LA/MBC). *Cancer Research.* 2021; 81(4_Supplement):OT-36-01-OT-36-01.

249. Kim S-B, Dent R, Im S-A, et al. Ipatasertib plus paclitaxel versus placebo plus paclitaxel as first-line therapy for metastatic triple-negative breast cancer (LOTUS): a multicentre, randomised, double-blind, placebo-controlled, phase 2 trial. *The Lancet Oncology.* 2017; 18(10):1360-1372.

250. Sweeney C, Bracarda S, Sternberg CN, et al. Ipatasertib plus abiraterone and prednisolone in metastatic castration-resistant prostate cancer (IPATential150): a multicentre, randomised, double-blind, phase 3 trial. *The Lancet.* 2021; 398(10295):131-142.

251. Ng PK, Li J, Jeong KJ, et al. Systematic Functional Annotation of Somatic Mutations in Cancer. *Cancer Cell.* 2018; 33(3):450-462.e410.

252. Gymnopoulos M, Elsliger MA, Vogt PK. Rare cancer-specific mutations in PIK3CA show gain of function. *Proc Natl Acad Sci U S A.* 2007; 104(13):5569-5574.

253. Huang C-H, Mandelker D, Schmidt-Kittler O, et al. The Structure of a Human p110α/p85α Complex Elucidates the Effects of Oncogenic PI3Kα Mutations. *Science.* 2007; 318(5857):1744-1748.

254. Guo S, Loibl S, von Minckwitz G, Darb-Esfahani S, Lederer B, Denkert C. PIK3CA H1047R Mutation Associated with a Lower Pathological Complete Response Rate in Triple-Negative Breast Cancer Patients Treated with Anthracycline-Taxane-Based Neoadjuvant Chemotherapy. *Cancer Res Treat.* 2020; 52(3):689-696.

255. Rogers HA, Estranero J, Gudka K, Grundy RG. The therapeutic potential of targeting the PI3K pathway in pediatric brain tumors. *Oncotarget.* 2017; 8(2):2083-2095.

256. Aldape K, Brindle KM, Chesler L, et al. Challenges to curing primary brain tumours. *Nat Rev Clin Oncol.* 2019; 16(8):509-520.

257. Singleton WGB, Bienemann AS, Woolley M, et al. The distribution, clearance, and brainstem toxicity of panobinostat administered by convection-enhanced delivery. *J Neurosurg Pediatr.* 2018; 22(3):288-296.

258. Palacin-Aliana I, Garcia-Romero N, Asensi-Puig A, Carrion-Navarro J, Gonzalez-Rumayor V, Ayuso-Sacido A. Clinical Utility of Liquid Biopsy-Based Actionable Mutations Detected via ddPCR. *Biomedicines.* 2021; 9(8).